

INFORMATION TO USERS

This manuscript has been reproduced from the microfilm master. UMI films the text directly from the original or copy submitted. Thus, some thesis and dissertation copies are in typewriter face, while others may be from any type of computer printer.

The quality of this reproduction is dependent upon the quality of the copy submitted. Broken or indistinct print, colored or poor quality illustrations and photographs, print bleedthrough, substandard margins, and improper alignment can adversely affect reproduction.

In the unlikely event that the author did not send UMI a complete manuscript and there are missing pages, these will be noted. Also, if unauthorized copyright material had to be removed, a note will indicate the deletion.

Oversize materials (e.g., maps, drawings, charts) are reproduced by sectioning the original, beginning at the upper left-hand corner and continuing from left to right in equal sections with small overlaps. Each original is also photographed in one exposure and is included in reduced form at the back of the book.

Photographs included in the original manuscript have been reproduced xerographically in this copy. Higher quality 6" x 9" black and white photographic prints are available for any photographs or illustrations appearing in this copy for an additional charge. Contact UMI directly to order.

UMI

A Bell & Howell Information Company
300 North Zeeb Road, Ann Arbor MI 48106-1346 USA
313/761-4700 800/521-0600

The Composition of Near-Earth Objects

by

Mark Hammergren

A dissertation submitted in partial fulfillment
of the requirements for the degree of

Doctor of Philosophy

University of Washington

1998

Approved by



Chairperson of Supervisory Committee

Program Authorized

to Offer Degree

ASTRONOMY

Date

AUGUST 20, 1998

UMI Number: 9907907

**Copyright 1998 by
Hammergren, Mark**

All rights reserved.

**UMI Microform 9907907
Copyright 1998, by UMI Company. All rights reserved.**

**This microform edition is protected against unauthorized
copying under Title 17, United States Code.**

UMI
**300 North Zeeb Road
Ann Arbor, MI 48103**

© Copyright 1998
Mark Hammergren

In presenting this dissertation in partial fulfillment of the requirements for the Doctoral degree at the University of Washington, I agree that the Library shall make its copies freely available for inspection. I further agree that extensive copying of this dissertation is allowable for scholarly purposes, consistent with "fair use" as prescribed in the U. S. Copyright Law. Requests for copying or reproduction of this dissertation may be referred to University Microfilms, 1490 Eisenhower Place, P. O. Box 975, Ann Arbor, MI 48106, to whom the author has granted "the right to reproduce and sell (a) copies of the manuscript in microform and/or (b) printed copies of the manuscript made from microform."

Signature Mark Hammer

Date August 20, 1998

University of Washington

Abstract

The Composition of Near-Earth Objects

by Mark Hammergren

Chairperson of the Supervisory Committee

Professor Don Brownlee

Department of Astronomy

I present reflectance spectra of 34 near-Earth objects (NEOs), 6 main-belt asteroids, and four non-NEO cometary candidates, all obtained with the Apache Point Observatory 3.5m telescope + Double Imaging Spectrograph. The spectra cover the wavelength range 3800 – 10,000 Å, encompassing regions of mineralogically important absorption features. Nearly all of the NEOs observed display ultraviolet and near-infrared absorptions characteristic of rock-forming silicate minerals. Of the 27 NEOs belonging to the S or Q taxonomic classes observed in this study, 15 are spectrally indistinguishable from ordinary chondrite meteorites. I perform extensive Monte Carlo simulations of the NEO and main belt populations aimed at quantifying the severe biases affecting observed taxonomic distributions. The bias-corrected NEO population in the 1 – 10 km diameter range is composed of $67 \pm 13\%$ S- or Q-type objects, and $30 \pm 7\%$ C-types objects, with the remainder being primarily of the spectrally degenerate X-class. The NEO population resembles most closely that of the inner main belt near the 3:1 mean motion resonance, and is consistent with that region being the sole source for NEOs. If extinct comet nuclei resemble the primitive taxonomic classes C, P, or D, the cometary component of the NEOs is constrained at $\lesssim 30\%$. I investigate trends of S-type spectral characteristics with size. The strength of the 1 μm absorption increases with decreasing size. There is a possible trend towards shorter-wavelength band centers with decreasing size, possibly reflecting a decreasing olivine abundance in the optically active surface fraction. For sizes below about 6 km, the spectral continuum reddens with increasing size. Above

6 km, this trend reverses, and larger objects have on average bluer continua. For the smaller objects, these trends are all consistent with predictions of the "space weathering" hypothesis. The bluer continua of the larger objects remains unexplained. All of these trends appear to be systematically dependent on size; specifically, no distinct separation exists between the larger S-type objects and the smaller ordinary chondrite-like bodies.

Contents

| | |
|---|----------|
| List of Figures | iii |
| List of Tables | vi |
| 1 Introduction | 1 |
| 1.1 NEOs: Unanswered Questions | 1 |
| 1.1.1 Origins | 1 |
| 1.1.2 The Meteorite / Asteroid Connection | 2 |
| 1.1.3 Space Weathering and the Ordinary Chondrite Problem | 2 |
| 1.1.4 Planetary and Biological Evolution | 3 |
| 1.1.5 Future Hazards and Resources | 4 |
| 1.2 Reflectance Spectroscopy | 4 |
| 1.3 Asteroid Taxonomy | 5 |
| 2 Data Acquisition and Processing | 7 |
| 2.1 Object Selection | 7 |
| 2.2 Observations | 7 |
| 2.3 Data Reduction | 11 |
| 2.4 Solar Analog Stars | 12 |
| 2.5 Possible Sources of Systematic and Random Error | 13 |
| 2.5.1 Bias Subtraction | 14 |
| 2.5.2 Flat Fielding | 14 |
| 2.5.3 Poor Subtraction of Night Sky Lines | 15 |
| 2.5.4 Poor Choice of Solar Analog? | 17 |
| 2.5.5 Misregistration of Object and Solar Analog Spectra | 18 |

| | | |
|----------|---|------------|
| 2.5.6 | Improper Correction for Telluric Absorption | 20 |
| 2.6 | Other Factors Which May Affect Spectra | 20 |
| 2.6.1 | Differential Refraction | 20 |
| 2.6.2 | Phase Reddening | 21 |
| 3 | Summary of Results | 22 |
| 3.1 | Taxonomic Classification | 31 |
| 4 | Discussion of Results for Individual Objects | 35 |
| 4.1 | NEOs | 35 |
| 4.1.1 | Spectra similar to ordinary chondrite meteorites | 35 |
| 4.1.2 | Unusual spectra with UV- and 1- μ m absorptions | 36 |
| 4.1.3 | 3103 Eger | 36 |
| 4.2 | Mars Crosser – 2078 Nanking | 37 |
| 4.3 | Non-NEO Cometary Candidates | 37 |
| 5 | Spectral Trends Among S-type Objects | 38 |
| 5.1 | Space Weathering | 38 |
| 5.2 | Modified Gaussian Model Fits | 39 |
| 5.3 | Spectral Trends with Diameter | 41 |
| 6 | Debiasing Asteroid Taxonomic Distributions | 45 |
| 6.1 | Introduction | 45 |
| 6.2 | Debiasing Methodology | 47 |
| 6.3 | The Detection Simulation | 48 |
| 7 | Discussion of Debiasing Results | 64 |
| 8 | Conclusions | 104 |
| | References | 106 |

List of Figures

| | | |
|-----|---|----|
| 2.1 | Plot of DIS blue CCD bias “ripple” | 14 |
| 2.2 | DIS red CCD flat field image | 16 |
| 2.3 | Reflectance spectrum of 1627 Ivar displaying fringing “ripples” . . | 17 |
| 2.4 | Ratios of Solar Analog Stars | 18 |
| 2.5 | Spurious features introduced by misregistration of spectra | 19 |
| 3.1 | NEO reflectance spectra | 23 |
| 3.2 | NEO reflectance spectra | 24 |
| 3.3 | NEO reflectance spectra | 25 |
| 3.4 | NEO reflectance spectra | 26 |
| 3.5 | NEO reflectance spectra | 27 |
| 3.6 | NEO reflectance spectra | 28 |
| 3.7 | Main-belt asteroid reflectance spectra | 29 |
| 3.8 | Reflectance spectrum of Mars-crossing asteroid 2078 Nanking . . . | 30 |
| 3.9 | Non-NEO cometary candidate asteroid reflectance spectra | 31 |
| 5.1 | Modified Gaussian Fits to NEO Spectra | 40 |
| 5.2 | 1- μm Band Strength vs. Size | 42 |
| 5.3 | 1- μm Band Center vs. Size | 43 |
| 5.4 | Visual Slope vs. Size | 44 |
| 6.1 | Probability of potential observation | 49 |

| | | |
|------|---|----|
| 6.2 | Dependence of potential observation on orbital elements for Spacewatch-type detection criteria | 50 |
| 6.3 | Taxonomic completenesses for the Atens, Apollos, and Amors. . . | 56 |
| 6.4 | Taxonomic completenesses for the Hungaria Group, Mars Crossers, and Flora Family. | 57 |
| 6.5 | Taxonomic completenesses for the Phocaea Group, Nysa Family, and Main Belt I. | 58 |
| 6.6 | Taxonomic completenesses for the Pallas Zone, Main Belt IIa, and Main Belt IIb. | 59 |
| 6.7 | Taxonomic completenesses for the Koronis Zone, Eos Zone, and Main Belt IIIa. | 60 |
| 6.8 | Taxonomic completenesses for the Themis Zone, Griqua Group, and Main Belt IIIb. | 61 |
| 6.9 | Taxonomic completenesses for the Cybele Group, Hilda Group, and Trojan Group. | 62 |
| 6.10 | Taxonomic completenesses for the Vesta Family. | 63 |
| 7.1 | Cumulative Size-Frequency Diagram for the Atens | 65 |
| 7.2 | Cumulative Size-Frequency Diagram for the Apollos | 66 |
| 7.3 | Cumulative Size-Frequency Diagram for the Amors | 67 |
| 7.4 | Cumulative Size-Frequency Diagram for the Hungaria Group . . . | 68 |
| 7.5 | Cumulative Size-Frequency Diagram for the Mars Crossers | 69 |
| 7.6 | Cumulative Size-Frequency Diagram for the Flora Family | 70 |
| 7.7 | Cumulative Size-Frequency Diagram for the Phocaea Group . . . | 71 |
| 7.8 | Cumulative Size-Frequency Diagram for the Nysa Family | 72 |
| 7.9 | Cumulative Size-Frequency Diagram for the Vesta Family | 73 |
| 7.10 | Cumulative Size-Frequency Diagram for Main Belt Zone I | 74 |
| 7.11 | Cumulative Size-Frequency Diagram for the Pallas Zone | 75 |
| 7.12 | Cumulative Size-Frequency Diagram for Main Belt Zone IIa . . . | 76 |
| 7.13 | Cumulative Size-Frequency Diagram for Main Belt Zone IIb . . . | 77 |

| | | |
|------|--|-----|
| 7.14 | Cumulative Size-Frequency Diagram for the Koronis Zone | 78 |
| 7.15 | Cumulative Size-Frequency Diagram for the Eos Zone | 79 |
| 7.16 | Cumulative Size-Frequency Diagram for Main Belt Zone IIIa | 80 |
| 7.17 | Cumulative Size-Frequency Diagram for the Themis Zone | 81 |
| 7.18 | Cumulative Size-Frequency Diagram for the Griqua Group | 82 |
| 7.19 | Cumulative Size-Frequency Diagram for Main Belt Zone IIIb | 83 |
| 7.20 | Cumulative Size-Frequency Diagram for the Cybele Group | 84 |
| 7.21 | Cumulative Size-Frequency Diagram for the Hilda Group | 85 |
| 7.22 | Cumulative Size-Frequency Diagram for the Trojan Group | 86 |
| 7.23 | Cumulative Size-Frequency Diagram for the NEOs | 87 |
| 7.24 | Taxonomic Gradient Across the Main Belt | 89 |
| 7.25 | Wave-like Oscillation in the Size-Frequency Distribution of S-type NEOs | 103 |

List of Tables

| | | |
|-----|---|-----|
| 2.1 | Observational Circumstances for NEOs | 9 |
| 2.2 | Observational Circumstances for non-NEOs | 11 |
| 2.3 | Selected Properties of Solar Analog Stars | 13 |
| 3.1 | Physical parameters for the 34 NEOs observed | 32 |
| 3.2 | Physical parameters for the non-NEOs observed | 33 |
| 6.1 | Selected Average Parameters for 12 Taxonomic Classes | 51 |
| 6.2 | Orbital Element Zones | 54 |
| 7.1 | Bias-corrected Taxonomic Fractions | 90 |
| 7.2 | Bias-corrected Taxonomic Fractions for the NEOs (excluding X-types) | 101 |
| 7.3 | Bias-corrected Taxonomic Fractions for the NEOs (if all X-types are P-type) | 102 |

Acknowledgements

I would like to thank everyone, everywhere, who helped me get to this place in my life. Folks of particular note include the following: my mother and brother, for their support throughout my life; Bill Baum, the consummate gentleman scientist; Don Brownlee, for his advice and for those great conversations on science, rockhounding, explosions, and beer; and Paul Hodge, for the example of his comfortable competence. Thanks too to Chris Stubbs and Craig Hogan for helping me out. My fellow students over the years, friends all, deserve special thanks for making this an enjoyable experience. To mention any names here would run the risk of leaving others off – and I can not bear to insult any by omission. Hail and well-met to my compatriots from Amnesty International Group 94! And finally, I must thank that most special institution whose threshold I crossed every time with joyful, thirsty anticipation: the College Inn Pub. Long may it serve astronomy grads!

To all my friends. You know who you are.

Chapter 1

Introduction

It is a cursed evil to any man to become so absorbed in any subject as I am in mine.

— Charles Darwin

On August 13, 1898, Gustav Witt in Berlin discovered the first of a new class of solar system objects. Later named 433 Eros, this apparently asteroidal object was notable for its orbit, which, unlike the more numerous population of main-belt asteroids which remain between the orbits of Mars and Jupiter, occasionally brings the object very close to the Earth. In the succeeding century, more than 500 planet-crossing peers of 433 Eros have been discovered. Known collectively today as the Near-Earth Objects (or “NEOs”), they remain the subject of intense scientific and popular interest for a simple and dramatic reason: NEOs have in the past, and will again in the future, strike the terrestrial worlds.

1.1 NEOs: Unanswered Questions

Knowledge of the distribution and composition of NEOs is becoming of increasing importance for addressing questions in many areas, including the following:

1.1.1 Origins

Due to interactions and impacts with the terrestrial planets, NEOs have a dynamical lifetime of $\sim 10^7 - 10^8$ years (Wetherill 1974) – much shorter than the age of the solar system. Since the cratering rate – and by implication the number

of NEOs – has remained nearly constant or even increased over the past 3.2 billion years (Grieve & Shoemaker 1994), the numbers of NEOs must continuously be replenished from some longer-lived reservoir located elsewhere in the solar system.

Two of the most commonly suggested sources include main-belt asteroids propelled by collisions into orbital resonances with Jupiter, and then perturbed into planet-crossing orbits, or cometary nuclei which have exhausted their supplies of volatiles due to repeated passages through the inner solar system (“extinct” comets). Most main-belt asteroids and comets appear to be compositionally distinct (Luu & Jewitt 1990). Compositional information on individual NEOs, and the distribution of taxonomic types among the NEOs, should provide constraints on the fraction of NEOs that may be extinct comets, as well as allow comparisons to main belt asteroids (Xu et al. 1995, Luu & Jewitt 1990).

1.1.2 The Meteorite / Asteroid Connection

The investigation of the relationship between meteorites and asteroids, their probable parent bodies, is a strong reason for studying the composition of asteroids. Meteorites have great scientific value since they may be studied in detail in a laboratory, and except for samples of the Moon and interplanetary dust particles, they represent the only extraterrestrial material we have ever examined. Detailed chronologies of chemical and physical processes in the early solar system have been derived from meteorites. Knowledge of specific meteorite parent bodies would then provide us with spatial information, a “map” to the locations of these physical processes. Since NEOs are already in planet-crossing, Earth-approaching orbits, they are in a particularly favorable location for the delivery of meteorites to the Earth. Dynamical studies have further suggested that a few well-placed parent bodies may dominate the flux of meteorites on the Earth (Greenberg & Nolan 1989). NEOs may thus be a very important connection in the transport of meteorites to the Earth.

1.1.3 Space Weathering and the Ordinary Chondrite Problem

The extreme rarity of spectral analogs for the ordinary chondrite meteorites, which make up more than 75% of terrestrial falls, is one of the most significant

and puzzling problems in solar system astronomy. More perplexing still, only one main-belt asteroid out of an observed sample of nearly a thousand appears to match an ordinary chondrite, while even though far fewer have been characterized, at least eight NEOs of similar colors have previously been observed (Xu et al. 1995, Binzel et al. 1996, Hicks et al. 1998).

Space weathering has been invoked as one way of solving the ordinary chondrite dilemma. In this hypothesis, the parent bodies of ordinary chondrites have been disguised by some unknown surface processing to appear as the very common S-type asteroids (cf., Lipschutz et al. 1989). NEOs are typically smaller than main-belt asteroids; additionally, since NEOs pass much nearer to the Earth than main-belt asteroids, very much smaller objects are occasionally observable. Smaller objects will have lower surface gravities and are generally predicted to retain less regolith (impact-generated “soil”). If some regolith process is responsible for disguising asteroid spectra, it should be less effective on NEOs than main-belt asteroids. Studies of NEO surface composition should thus contribute to our understanding of space weathering on all asteroids.

1.1.4 Planetary and Biological Evolution

Craters resulting from NEOs and other planet-crossing objects are the dominant landforms on the Moon, Mercury, Mars, and many other solar system bodies (Melosh 1980), and more than 140 impact structures have been identified on the Earth (Grieve & Shoemaker 1994). It is thought that most of the volatiles present on the surface of the Earth (i.e., the atmosphere and oceans) were delivered after the formation of the planet by the accretion of asteroids and comets (Hunten 1993, Chyba 1990). It is possible that much of the Earth’s storehouse of organic material – the basis for life – arrived in the same manner (Marcus & Olsen 1991). These theories are highly dependent on our understanding of NEO composition.

There is increasing evidence that the Cretaceous-Tertiary mass extinction was caused by the impact of an asteroid or comet (Grieve & Shoemaker 1994). At least one composition-dependent extinction mechanism – poisoning of the biosphere by meteoritic heavy metals – has been explored (Davenport et al. 1990).

1.1.5 Future Hazards and Resources

The recent collision of Comet Shoemaker-Levy 9 with Jupiter underscored the fact that planetary impacts still occur. Studies have been undertaken to determine the threat that such impacts pose to the Earth (e.g., "the Spaceguard Survey," Morrison et al. 1992). The probability that an as-yet undiscovered NEO will hit the Earth is estimated at one chance in a thousand during the lifetime of an average American. Knowledge of a potential impactor's composition would allow us to better estimate its mass, and thus destructive potential, and its likelihood to penetrate the Earth's atmosphere (Shoemaker et al. 1995, Hills & Goda 1993).

NEOs are also important resources for the future exploration of space. Pieces of asteroids, obtained on the ground as meteorites, are seen to be composed of a wide variety of materials including iron-nickel alloy, small amounts of precious metals, organic chemicals, water of hydration, and chemically-bound oxygen. Furthermore, many NEOs are accessible with less energy than required by a Moon landing, making them the cheapest targets beyond the Moon for robotic exploration, and by far the easiest for human exploration (Shoemaker et al. 1995).

1.2 Reflectance Spectroscopy

Reflectance spectroscopy has emerged as a powerful tool for probing the surface compositions of small solar system objects. Pioneering work in the remote sensing of solar system body composition by McCord et al. (1970) was paralleled by fundamental developments in the crystal field theory of mineral absorption features (Burns 1970a) and in the laboratory determination of diagnostic mineral absorption features (Adams & Filice 1967; Adams 1974, 1975; Hunt & Salisbury 1970). Pieters & McFadden (1994) recount a detailed history of the use of reflectance spectroscopy for meteorite and asteroid studies. These related lines of research paved the way for the utility of reflectance spectroscopy in remote sensing.

The slope of the spectral continuum, and the presence or absence of certain solid-state absorption features can provide specific mineralogical information (Burns 1983). For example, the common rock-forming silicate minerals pyroxene

and olivine show strong absorption features near $1\ \mu\text{m}$. Pyroxene has another strong feature further in the infrared near $2\ \mu\text{m}$, while such a feature is weak or nonexistent in spectra of olivine. Furthermore, Adams (1974) showed that the wavelength positions of the silicate absorption band minima are dependent on Fe, Mg, and Ca composition. Gaffey et al. (1993) provide a review of progress in the field, and summarize several mineralogical properties accessible to reflectance spectroscopy.

While crystal field theory can provide some background for the interpretation of reflectance spectra, analyses are more often dependent on an empirical comparison to laboratory spectra of material analogs or to a study of the general variations in spectra across an object (eg., studies of the Moon by Charette et al. 1974) or within a population of objects (e.g., differences among the S-type asteroids by Gaffey et al. 1993). A common practice in asteroid studies is to compare asteroid reflectance spectra to those of meteorites obtained in the laboratory, though arguments based on such comparisons are extremely controversial (see, for example, Section 1.1.3 on the ordinary chondrite dilemma, and Gaffey et al. 1993 for more information).

Although compositional surveys of NEOs are of great scientific value, these fast-moving, faint objects pose considerable observational difficulties, and few concerted studies have been attempted (Howell 1994, Hicks et al. 1998). Spectroscopic surveys of main-belt asteroids occasionally pick up some NEOs as targets-of-opportunity, when individual NEOs have particularly favorable apparitions near the Earth (Xu et al. 1995, Binzel 1996). Other programs have returned data of low signal-to-noise (McFadden et al. 1984), low spectral resolution (Zellner et al. 1985), or limited spectral range (Luu & Jewitt 1989).

Since ground-based remote sensing will always be far less expensive than space missions, reflectance spectroscopy will remain the most common method of studying the compositions of a population of objects such as the NEOs.

1.3 Asteroid Taxonomy

Taxonomy is the process by which a population of objects or organisms are split into unique categories, on the basis of perceived or actual similarities and

differences between and among these objects. It is important to remember that *perceived* similarities or differences are not necessarily indicative of genetic or compositional relationships. (This is akin to the distinction in the biological sciences between phenotyping and genotyping.)

The asteroid taxonomic system in most widespread current use is the "Tholen system" (Tholen & Barucci 1989), in which a cluster and principal component analysis were applied to Eight Color Asteroid Survey (ECAS) data along with corresponding IRAS asteroid albedos. The 14 classes in the original "Tholen system" have been supplemented by other researchers with at least four other classes, some of which contain only a single member (Tholen & Barucci 1989; Gaffey et al 1993). Other classification schemes, including the "G-mode analysis" (Barucci et al. 1987), the "Three-Parameter system" (Tedesco et al. 1989), and a neural network analysis (Howell et al. 1994) have suffered from a disadvantage common with the Tholen system, namely, that in order to formally classify a single new object, one must re-run the analysis on the entire set. All of these taxonomies use the relative fluxes of asteroids at a small number of wavelength bands as inputs; none intelligently apply information on solid-state absorptions gained from reflectance spectroscopy theory, and none make full use of the higher resolutions offered by reflectance spectroscopy. It is obvious that asteroid taxonomy needs to be refined to make it relevant to current technologies and theory, but it is beyond the scope of this work to carry out this task.

* * *

In this work I present moderate resolution reflectance spectra of 34 NEOs. The data acquisition and reduction of these spectra are described in Chapter 2. The spectra are presented in Chapter 3. In Chapter 4, I discuss individual objects and the implications of the spectral observations. In Chapter 5, I compare this work's sample of 34 NEO reflectance spectra with previously published NEO and main-belt asteroid reflectance spectra, with a particular view towards describing spectral trends with object size. In Chapter 6, I describe a new model for bias-correcting observed taxonomic distributions among the various NEO and asteroid populations. The results of the application of this bias correction are presented in Chapter 7. Chapter 8 summarizes the conclusions of this work.

Chapter 2

Data Acquisition and Processing

It seems to me that those sciences which are not born of experience, the mother of all certainty, and which do not end in known experience – that is to say, those sciences whose origin or process or end does not pass through any of the five senses – are vain and full of errors.

— Leonardo da Vinci

2.1 Object Selection

The NEOs (and other objects) observed during the course of this survey were selected from a catalog of $\sim 30,000$ asteroids for which reasonably good orbits were known (Bowell 1998). The main criteria for inclusion in the NEO survey were brightness and visibility at the Apache Point Observatory (APO). The faint magnitude limit used in the selection process was typically $V \sim 18.5$. Brighter objects were usually given a higher priority, since these objects were often those making particularly close approaches to the Earth. Objects with solar elongations less than 60° and those at minimum airmasses greater than 2.0 were generally excluded, although exceptions to these guidelines were sometimes made for high priority targets. On any given night, about 10 – 20 objects passed all the above selection criteria. No further attempt was made to define a strictly absolute-magnitude-limited sample, since it was felt that this would result in an impractically small number of candidates.

2.2 Observations

Spectra of a total of 34 near-Earth objects, 6 main-belt asteroids, 1 Mars-crosser, 4 non-NEO cometary candidates, and three comets were obtained during the

course of this research. The comet spectra will be discussed in another work. All of the spectra were taken using the Double Imaging Spectrograph (DIS) on the 3.5 m telescope at APO. Table 2.1 presents the observational circumstances for these objects. Table 2.2 presents the same data for the non-NEOs.

The DIS uses a dichroic filter with a transition wavelength of 5350 Å to split incoming light into separate red and blue beams. For spectroscopy, these beams are fed to two different gratings which are optimized for the appropriate wavelength regime, whereas for imaging, mirrors are put in place of the gratings. The red light is then sent to a 800×800 pixel TI CCD, and the blue light to a thinned, UV-coated 512×512 pixel SITe CCD. In low-resolution mode, the blue side utilizes a 150 line mm^{-1} grating resulting in a dispersion of about 6.3 Å per pixel , and the red side a 300 line mm^{-1} grating with a dispersion of about 7.0 Å per pixel .

The DIS is described in more detail in Kundic et al. 1995 and on the APO DIS homepage at <http://www.apo.nmsu.edu/Instruments/DIS/>.

For the observations made prior to 08/19/96, a $6' \times 3''$ wide acetate slit was used. During these exposures, no type of guiding was possible, and individual exposures were limited to $\sim 5\text{--}15$ minutes to limit telescope drift. For later observations, a $6' \times 2''$ aluminized glass slit was used to allow the employment of a slit camera. Longer exposure times were then possible since the slit camera could be used to ensure the object did not drift out of the slit.

The predicted positions of these objects and the telescope pointing accuracy were generally not good enough for immediate identification on the basis of their apparent locations in images. Most objects were instead identified by their apparent motion between successive images. Both the amount and direction of apparent motion were used in ensuring that the moving object seen was indeed the intended target. The identification image exposures were short enough that no trailing was evident even for the fastest-moving NEOs observed.

During spectral exposures, the telescope was driven at the predicted apparent rates of the target objects. After the installation of a slit camera in DIS and the use of the $2''$ aluminized slit, occasional slit camera images were taken during spectroscopic exposures in an effort to compensate for telescope drift.

The spectrograph slit was either maintained at the parallactic angle during

Table 2.1: Observational Circumstances for the 34 NEOs observed

| Object | Date(s) | V | Δ | r | ϕ |
|-----------------|----------|-------|----------|------|--------|
| | Observed | (mag) | (AU) | (AU) | (deg) |
| 433 Eros | 95/09/21 | 11.6 | 0.60 | 1.57 | 16.6 |
| | 96/01/22 | 12.6 | 0.82 | 1.19 | 54.8 |
| 1627 Ivar | 95/04/26 | 14.5 | 0.81 | 1.70 | 22.9 |
| 1864 Daedalus | 97/01/31 | 18.2 | 1.41 | 2.30 | 13.7 |
| 2062 Aten | 95/01/01 | 13.8 | 0.15 | 1.12 | 18.3 |
| | 96/04/17 | 18.4 | 0.52 | 0.80 | 96.9 |
| | 96/04/18 | 18.4 | 0.52 | 0.80 | 96.7 |
| 2063 Bacchus | 96/04/17 | 14.1 | 0.13 | 1.12 | 24.8 |
| | 96/04/18 | 14.2 | 0.14 | 1.13 | 24.9 |
| 2102 Tantalus | 95/05/05 | 18.2 | 0.83 | 1.07 | 62.5 |
| | 95/06/27 | 15.5 | 0.34 | 1.32 | 22.5 |
| 2201 Oljato | 96/01/22 | 16.2 | 0.43 | 0.93 | 83.6 |
| | 96/01/23 | 16.2 | 0.43 | 0.92 | 85.2 |
| 2212 Hephaistos | 95/01/01 | 18.9 | 2.44 | 2.59 | 22.3 |
| | 97/01/31 | 19.0 | 2.39 | 2.86 | 19.2 |
| 2368 Beltrovata | 95/05/05 | 18.1 | 1.25 | 2.20 | 12.2 |
| 3103 Eger | 96/05/22 | 17.3 | 0.78 | 1.47 | 40.6 |
| 3122 Florence | 96/10/29 | 17.1 | 1.23 | 1.42 | 43.2 |
| 3199 Nefertiti | 96/09/18 | 16.8 | 0.83 | 1.13 | 59.4 |
| 3200 Phaethon | 96/09/18 | 16.1 | 0.66 | 1.24 | 54.0 |
| | 96/10/29 | 16.4 | 0.83 | 1.71 | 22.8 |
| 3691 1982 FT | 96/01/22 | 16.7 | 0.85 | 1.75 | 18.0 |
| 3752 Camillo | 95/07/22 | 17.8 | 0.93 | 1.76 | 26.3 |
| 4055 Magellan | 95/05/05 | 18.0 | 1.29 | 2.00 | 25.8 |
| 4197 1982 TA | 96/09/18 | 15.4 | 0.57 | 1.49 | 25.4 |

Table 2.1 – *Continued*

| Object | Date(s) | V | Δ | r | ϕ |
|---------------|----------|-------|----------|------|--------|
| | Observed | (mag) | (AU) | (AU) | (deg) |
| 5131 1990 BG | 95/01/01 | 17.8 | 1.55 | 2.32 | 18.8 |
| 5143 Heracles | 96/10/29 | 15.9 | 0.95 | 1.92 | 9.7 |
| 6053 1993 BW3 | 96/01/23 | 15.7 | 0.62 | 1.59 | 10.2 |
| 6491 1991 OA | 95/07/22 | 17.8 | 0.26 | 1.17 | 48.9 |
| 6569 1993 MO | 95/04/26 | 17.9 | 0.65 | 1.44 | 37.8 |
| 7088 Ishtar | 95/04/25 | 18.8 | 0.99 | 1.96 | 10.1 |
| 7336 1989 RS1 | 96/09/18 | 16.2 | 0.19 | 1.20 | 9.8 |
| 7358 1995 YA3 | 96/01/23 | 16.9 | 1.19 | 2.16 | 6.2 |
| 7822 1991 CS | 96/08/19 | 15.2 | 0.12 | 1.05 | 66.9 |
| 7889 1994 LX | 95/06/27 | 18.0 | 1.10 | 1.41 | 45.9 |
| 7977 1977 QQ5 | 95/01/01 | 19.3 | 1.62 | 2.25 | 22.9 |
| 1990 VB | 95/01/01 | 17.9 | 0.97 | 1.93 | 7.2 |
| 1991 BB | 96/01/22 | 17.8 | 0.76 | 1.49 | 36.2 |
| 1992 QN | 96/09/18 | 17.4 | 0.58 | 1.58 | 8.5 |
| 1996 AE2 | 96/01/23 | 16.7 | 0.16 | 1.13 | 20.5 |
| 1996 FQ3 | 96/04/17 | 17.7 | 0.11 | 1.09 | 34.5 |
| | 96/04/18 | 17.8 | 0.11 | 1.09 | 35.6 |
| 1996 JG | 96/05/19 | 14.3 | 0.06 | 1.07 | 9.3 |

NOTE— Visual magnitude, geocentric and heliocentric distance, and phase angle are given as listed in ephemeris at time of observation.

the exposure or reset to the parallactic angle at the start of every exposure to minimize the effects of differential refraction.

Observations of solar analog stars (see Section 2.4) were made at least once and usually several times per night, at airmasses as near as possible to those at which the targets were observed. One or two spectroscopic standards were also

Table 2.2: Observational Circumstances for non-NEOs

| Object | Date(s) | V | Δ | r | ϕ |
|------------------|----------|-------|----------|------|--------|
| | Observed | (mag) | (AU) | (AU) | (deg) |
| 8 Flora | 95/03/22 | 10.6 | 1.95 | 2.07 | 28.5 |
| 225 Henrietta | 95/09/21 | 12.4 | 1.73 | 2.72 | 4.0 |
| 631 Philippina | 95/03/22 | 12.9 | 1.79 | 2.57 | 16.8 |
| 692 Hippodamia | 96/04/18 | 14.1 | 2.22 | 3.05 | 12.3 |
| 1279 Uganda | 97/01/31 | 17.7 | 2.44 | 2.82 | 19.9 |
| 1653 Yakhontovia | 97/01/31 | 15.4 | 1.94 | 1.78 | 30.4 |
| 2078 Nanking | 96/10/29 | 15.4 | 1.37 | 1.73 | 35.1 |
| 2906 Caltech | 96/04/18 | 15.5 | 2.65 | 3.47 | 11.0 |
| 2938 Hopi | 95/04/26 | 18.0 | 3.50 | 4.17 | 11.3 |
| 6144 1994 EQ3 | 95/05/05 | 17.3 | 2.90 | 3.41 | 15.9 |
| 1996 PW | 96/08/19 | 17.2 | 1.53 | 2.54 | 2.6 |

NOTE— Visual magnitude, geocentric and heliocentric distance, and phase angle are given as listed in ephemeris at time of observation.

usually observed.

2.3 Data Reduction

The spectra were extracted and calibrated using a combination of standard IRAF procedures and custom-written routines in IDL. The sequence of processing steps is described in this section; the potential for random or systematic errors introduced by these reduction steps is described in detail in Section 2.5.

About 10 bias frames were obtained at the beginning or end of the night of observation. Unfortunately, because of problems with the DIS blue CCD chip (described in Section 2.5.1 below) bias frame subtraction was usually not performed.

Spectroscopic flat fields were taken using “white-light” quartz lamps

illuminating the closed mirror cover. This results in a non-uniform and instrument-rotation dependent illumination pattern which does not match sky illumination very well. Typically, a stack of ~ 10 flat field images was combined into an outlier-resistant average flat field. This flat was then divided by a median-filtered copy to remove the spectral continuum and lower-order illumination variations across the field. This normalized flat was then divided into each object exposure to remove pixel-to-pixel variations in efficiency.

Spectra were extracted using a custom-written routine in IDL. Night sky lines were fit in regions surrounding the object aperture, and were subtracted out. Cosmic ray removal was performed manually on the extracted spectra.

Wavelength dispersion solutions were accomplished by taking reference He-Ne-Ar arcs at the beginning or end of the night. Formal fits using the arcs were generally good to a small fraction of an Ångström. However, the central wavelength settings of the gratings changed throughout the night (especially in the early runs of this survey), often from one exposure to the next, and sometimes by more than a hundred Ångströms. Wavelength zeropoints were determined for each individual spectrum by examination of night-sky line positions (in longer exposures, for fainter objects) or by locating strong solar or telluric atmospheric absorption features (in brighter objects). Wavelengths in calibrated spectra are believed to be accurate to within $\sim 2\text{--}3$ Å.

Atmospheric extinction was corrected by division with the Kitt Peak standard extinction table provided in IRAF. Object spectra were divided by spectra of solar analog stars to remove the solar spectrum and instrumental efficiency variations, and the red and blue portions of the spectrum were knitted together to produce the final reflectance spectrum.

2.4 Solar Analog Stars

A key step in the reduction of reflectance spectra is the ratioing of the object spectrum by the reflected solar spectrum in order to reveal the underlying solid-state absorption characteristics of the object being studied. The Sun is far too bright to directly observe with the same instrument as other solar system objects. Since there are no perfect artificial sources of the solar spectrum, and since there

Table 2.3: Solar Analog Star Properties

| Name | Type | V (mag) | $U - B$ (mag) | $B - V$ (mag) |
|------------|-------|--------------|------------------|------------------|
| Hyades 64 | G2V | 8.12 | 0.20 | 0.69 |
| 16 Cygni B | G1.5V | 5.96 | 0.19 | 0.64 |
| HD 120528 | G5V | 8.56 | 0.21 | 0.66 |
| HD 144873 | G5 | 8.5 | ... ^a | ... ^a |
| HD 191854 | G5 | 7.46 | 0.22 | 0.69 |

^a Colors not available for HD 144873.

are no perfectly colorless reflectors of sunlight available in the night sky, one must use sun-like stars as surrogate providers for the solar spectrum. It is also highly desirable that the surrogate solar spectrum pass through the same atmospheric and optical path, is observed with the same detectors, and is calibrated in the same manner as the solar system objects being studied, since this congruency greatly reduces the possibility that instrumental or data reduction artifacts are introduced into the final reflectance spectrum.

The Sun is a fundamental calibrator in many astronomical photometric and abundance studies, which makes true solar analogs scientifically valuable for the reasons listed above. Such stars have been sought for decades (cf. Hardorp 1978). A list of five solar analog stars was drawn from catalogs prepared by Hardorp. Some characteristics of these stars (drawn from SIMBAD) are presented in Table 2.3.

2.5 Possible Sources of Systematic and Random Error

Each of the data reduction steps described in Section 2.3 can introduce error. The magnitude of these potential errors and their characteristics are described below.

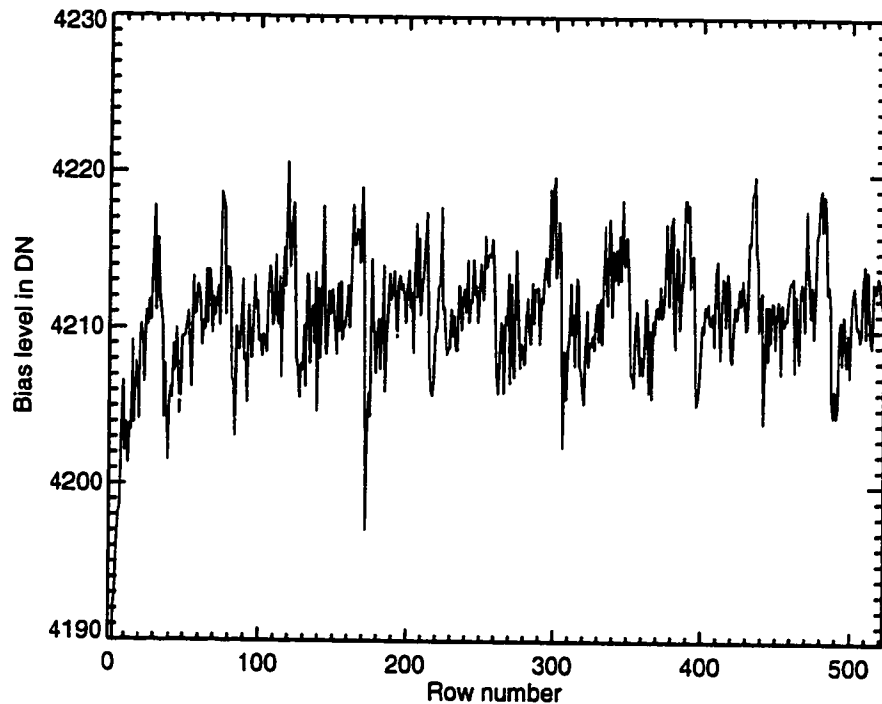


Figure 2.1: Average profile for central 10 columns in the DIS “blue” CCD chip bias frame. A non-stationary “ripple” presumably due to 60-Hz electrical interference is visible.

2.5.1 Bias Subtraction

During most of the course of the survey, the DIS blue CCD chip bias suffered from a non-stationary noise pattern apparently due to 60-Hz electrical interference (Figure 2.1). While much of this pattern could be removed by fitting and dividing out the “ripple,” the subtraction of a bias frame still usually increased the noise level in the final product. Therefore, most spectra were not bias-subtracted. Those that were subject to bias subtraction were examined carefully for any artifacts which may have been introduced; none were found.

2.5.2 Flat Fielding

The DIS red CCD chip is cosmetically unclean. Various spots and hairlike features are evident in flat fields and in images with high sky backgrounds (Figure 2.2). As described in Section 2.5, the illumination pattern in flat fields does not match

that of the night sky. This causes slight differences in the positions of the "hairs" and "spots" between flat fields and night sky images or spectra. When dividing by these imperfect flat fields, residuals appear at the locations of these defects. An examination of spectra for flat-field residuals indicates that such residuals appear most strongly near 7800 \AA , slightly redward of the strong telluric oxygen absorption, and less conspicuously near 6100 \AA , 6500 \AA , and 9200 \AA . When present, these artifacts appear as spikes or dips of ~ 20 DN amplitude over scales of around $50 - 100 \text{ \AA}$. Such artifacts are generally systematic in effect: a given flat-field defect will repeatedly produce either a positive spike or a negative dip. These regions must be treated with care in further analyses.

In addition to these defects, the DIS red CCD chip also suffers from fringing in the near-infrared, which is apparent in spectroscopic flat field images and in the spectra of some of the objects observed. (Fringes are visible in Figure 2.2 as alternating dark and bright horizontal bands in the upper half of the image). Since atmospheric night-sky emission lines (particularly the near-infrared OH^- lines) cause stronger fringing than the "white" light in which flats are obtained, flat-fielding when strong fringing is present can introduce additional noise (cf. Tyson 1989). This artifact can be seen in the reflectance spectrum of 1627 Ivar as another "ripple" of ~ 5 DN amplitude through the wavelength range $\sim 7600 - 9600 \text{ \AA}$ (Figure 2.3). Fringe artifacts can be thought of as a source of pseudo-random noise, as negative dips alternate with positive "bumps" around a common mean level. Since the scale of these fringes ($\sim 90 \text{ \AA}$) is much smaller than most solid-state absorption features (which are typically hundreds of Angstroms wide), they are an unsightly but relatively insignificant problem in this application.

2.5.3 Poor Subtraction of Night Sky Lines

In wavelength regimes or in exposures where the contrast between object and night sky spectra was very low, night sky line removal was problematic and apt to result in residual artifacts. This problem is particularly troublesome in the near-infrared redward of 9000 \AA , where night-sky OH^- emission is bright, the reflected solar flux is low, instrumental efficiencies drop rapidly, and many asteroids display absorption features (further reducing the available flux). Frustratingly, these effects often conspire to introduce a thicket of powerful noise spikes in the

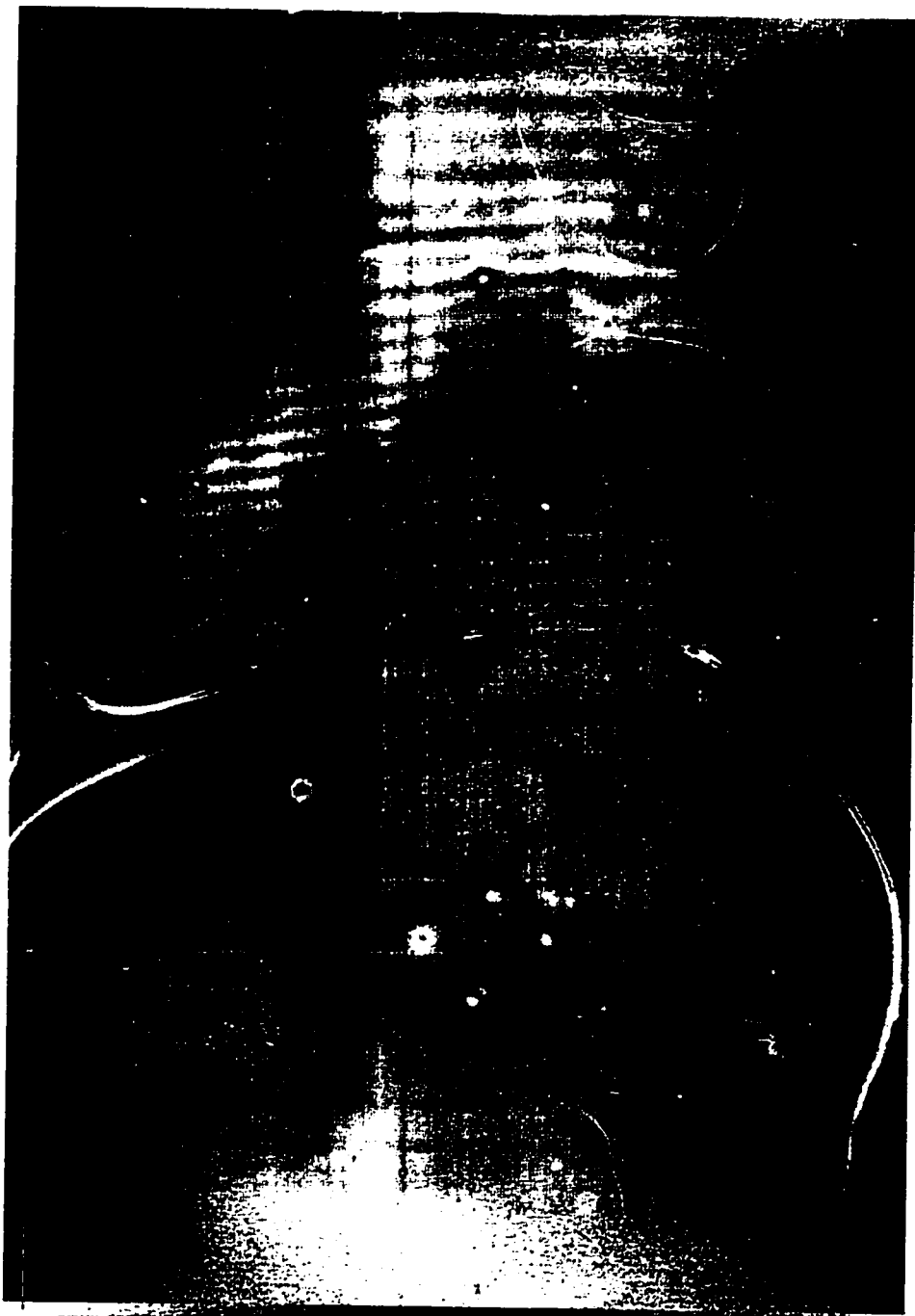


Figure 2.2: Flat-field image for the DIS “red” CCD chip. In addition to the “hairs” and “spots” visible in this image, fringing is apparent in the upper half, corresponding to the longer-wavelength end of the “red” spectra.

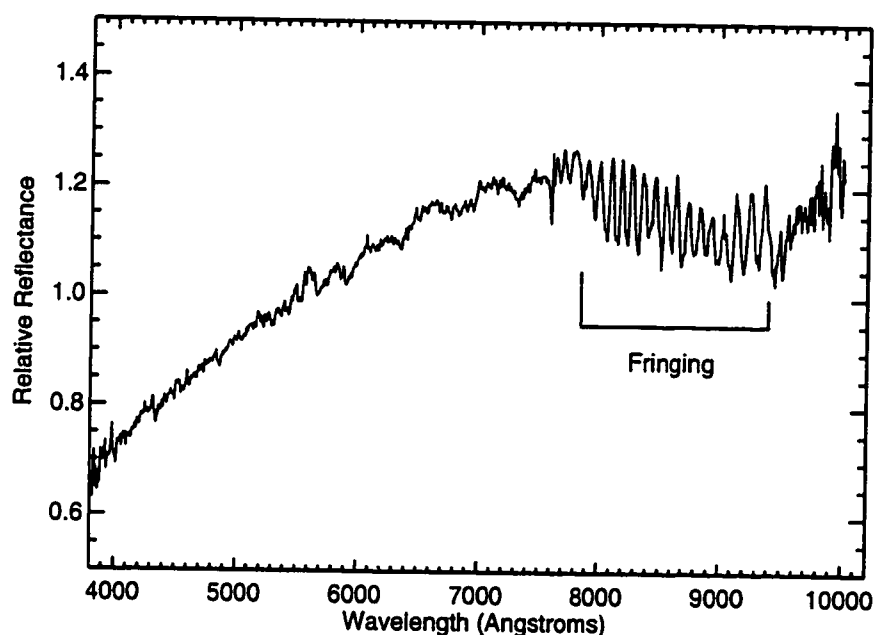


Figure 2.3: Fringing is apparent in extracted spectra as a $\sim 5\%$ amplitude “ripple” in the 7600 – 9400 Å region.

mineralogically important 9000 – 10,000 Å region. In general, over-subtraction of night sky lines is as likely as under-subtraction, leading to an increase in random noise levels in those spectral regions affected rather than a systematic shift in continuum level.

2.5.4 Poor Choice of Solar Analog?

The ultimate step in the production of a reflectance spectrum is the division by the solar (or as is usually the case for astronomical observations, the solar analog) spectrum. The choice of a solar analog star for use as a reference is thus critical for the quality and reliability of the product. Several solar analog stars from Table 2.3 were observed on the same night as a check on the similarity of their spectra. Figure 2.4 displays ratios of solar analog stars with one another. The spectra used in these ratios were all obtained on the same night, but at significantly different airmasses (in this respect, the figure may also be used to judge the accuracy of the atmospheric extinction correction). Apart from artifacts introduced by strong or changing telluric absorptions, the spectral ratios are flat

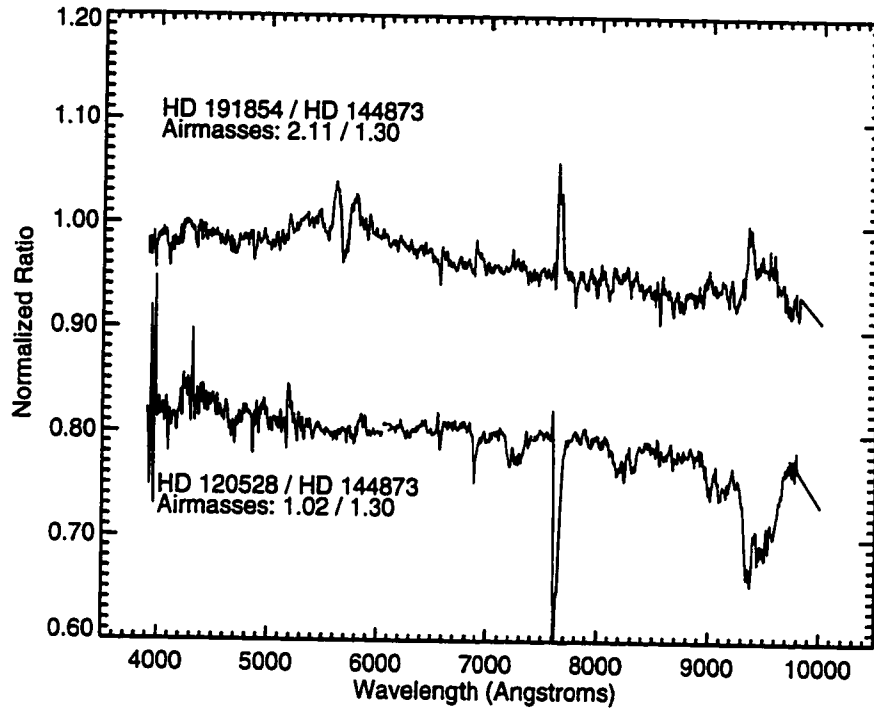


Figure 2.4: Ratios of solar analog stars observed on 05/22/96. The spectra have been offset vertically by 0.2 units for clarity.

to within 10% over the wavelength range 3800 Å to 10200 Å.

2.5.5 Misregistration of Object and Solar Analog Spectra

A misregistration between the solar analog star spectrum and the object spectrum may result in strong spurious features. There are several different manifestations of these artifacts: a misregistration of the relatively narrow solar or telluric atmospheric absorption features will cause correspondingly sharp dips and/or spikes to appear, while a misregistration of larger scale trends in instrumental efficiency can cause systematic bends in reflectance spectra. These latter artifacts will be especially apparent where the efficiency changes rapidly. These two effects are illustrated in Figure 2.5. A poor removal of absorption features may also be due to a change in the instrumental point spread function between the object spectrum and the solar analog star spectrum; at some level, this effect is inevitable.

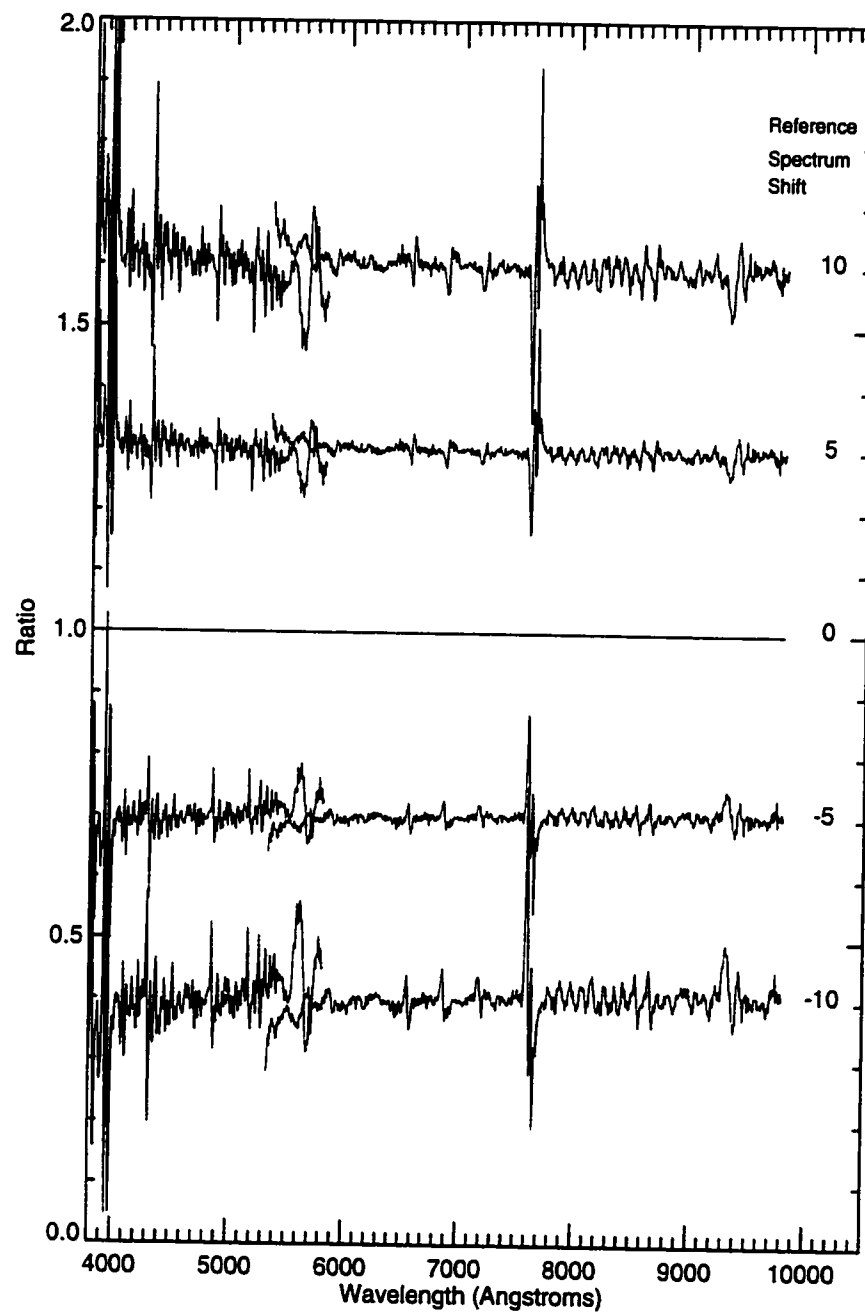


Figure 2.5: Ratios of artificially mis-registered solar analog spectra, illustrating the possible systematic shifts in continuum levels and the increase in apparently “random” noise due to poorly canceled stellar and telluric absorption lines. Ratios have been offset by 0.3 units for clarity.

If these spurious features can not be removed even through reprocessing the spectrum, then regions of the reflectance spectrum around the strong telluric oxygen absorption band and regions at both the far red and far blue ends of the spectrum are suspect and should be avoided in further analyses. Those spectra in which this effect was thought to have been important have had the appropriate ends truncated. Most other analyses are inherently resistant to possible errors near the telluric oxygen absorptions.

2.5.6 Improper Correction for Telluric Absorption

Since the solar analog star spectra were obtained at airmasses similar to the object spectra, differences in atmospheric extinction between the two were minimized, and the effects of any improper correction for extinction are likely to be small. However, certain telluric absorption features are particularly prominent and heavily dependent on airmass. For example, a change in the abundance of water vapor in the atmosphere may cause a faulty correction in the reflectance spectrum near 9600 Å, or a poor airmass match may cause strong residuals near the telluric oxygen absorption. Effects such as these are expected to be most important for observations at higher airmasses. Therefore, most observations were limited to airmasses less than 2.0, and almost all below 3.0.

2.6 Other Factors Which May Affect Spectra

2.6.1 Differential Refraction

Filippenko (1982) strongly cautioned astronomers about the phenomenon of atmospheric differential refraction. Unless observers plan for this effect, significant systematic errors in measured continuum intensities may arise, especially when observing at high airmasses. To avoid these errors in this work, the spectrograph slit was either maintained at the parallactic angle during the exposures, or reset to the parallactic angle at the beginning of each exposure. Also, observations were limited to relatively low airmasses (as detailed above).

2.6.2 Phase Reddening

Adams and Filice (1967) first showed that powdered rock samples can vary in color with phase angle and particle size. Since then it has been found that main-belt asteroids, the Moon, and powdered samples of meteorites also appear redder at higher phase angles (Gradie & Veverka 1986), over the phase angle ranges at which these objects are likely to be observed. Relatively little new work has been done on this subject. Luu & Jewitt (1990) estimate the effect for S-type asteroids as a linear increase in continuum slope by $\sim 0.16\% \pm 0.13\% / 10^3 \text{ \AA}$ per degree, and $\sim 0.15\% \pm 0.17\% / 10^3 \text{ \AA}$ per degree for C-type asteroids. Over the $\sim 6,000 \text{ \AA}$ range typically observed in this study, this effect could amount to a systematic reddening of about 1% per degree. Studies of the Moon and rocks powders indicate that phase reddening is not a monotonic function of phase angle, however, so that observations at very high phase angles would not necessarily be reddened as severely as a simplistic application of the Luu & Jewitt (1990) estimate would suggest (Adams & Filice 1967). Since NEOs are often observed at far greater phase angles than main-belt asteroids, the reader is cautioned that a simple comparison between NEO and main-belt object continuum slopes may be compromised to some degree by the effects of phase reddening.

Chapter 3

Summary of Results

Speak to the Earth, and it shall teach thee.

— Bible, Job 12:8

The reflectance spectra of the 34 NEOs which were observed during the course of this survey are presented in Figures 3.1 – 3.6. Reflectance spectra of the other objects, including the non-NEO cometary candidates, are presented in Figures 3.7 – 3.9. All spectra have been normalized to a reflectance of unity at 5500 Å by convention. The full-resolution, unsmoothed spectra are plotted as thin lines. The fainter objects show a considerable degree of scatter, especially at short or long wavelengths where the observed flux is very low. In some cases, the spectra have been truncated below ~ 4000 Å or above ~ 9500 Å to avoid these degraded data. To aid the eye, spectra were also binned in 250 Å intervals. The mean reflectances in these bins are overplotted as filled circles; the error bars correspond to plus and minus one standard deviation of the data in each bin. All of the automatic fits described in Section 5.2 were performed on the full-resolution, unsmoothed spectra. Some of the taxonomic classifications (Section 3.1) were performed by eye using the binned data.

Selected physical parameters for the NEOs are listed in Table 3.1, and non-NEOs in Table 3.2. Taxonomic classifications are described in Section 3.1. The Tisserand invariant T is a quasi-constant of motion for the restricted three-body problem of the Sun-Jupiter system (cf. Weissman et al. 1989), and is defined as

$$T = \frac{a_j}{a} + 2\sqrt{\left(\frac{a_j}{a}\right)(1 - e^2)} \cos i \quad (3.1)$$

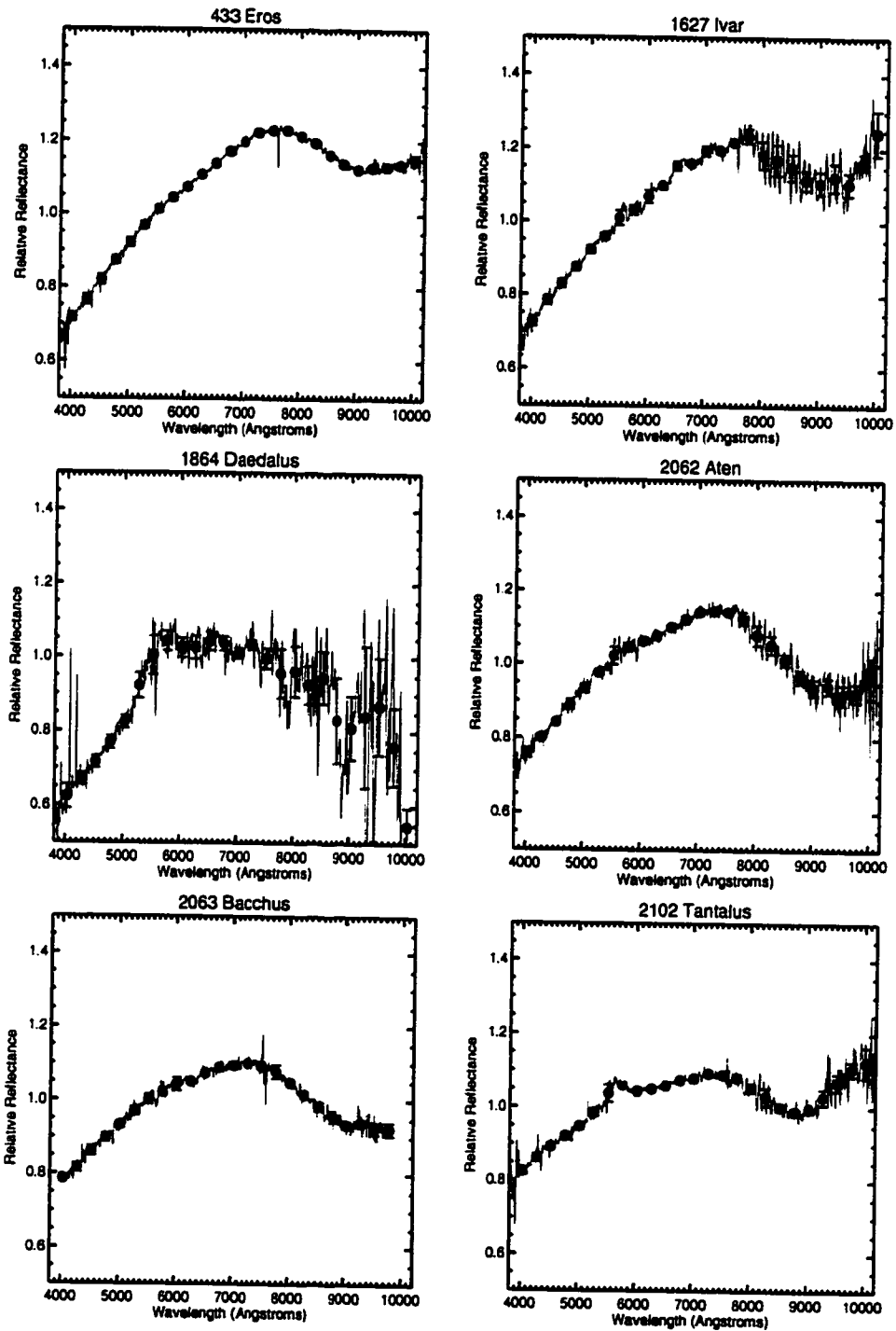


Figure 3.1: NEO reflectance spectra for 433 Eros, 1627 Ivar, 1864 Daedalus, 2062 Aten, 2063 Bacchus, and 2102 Tantalus.

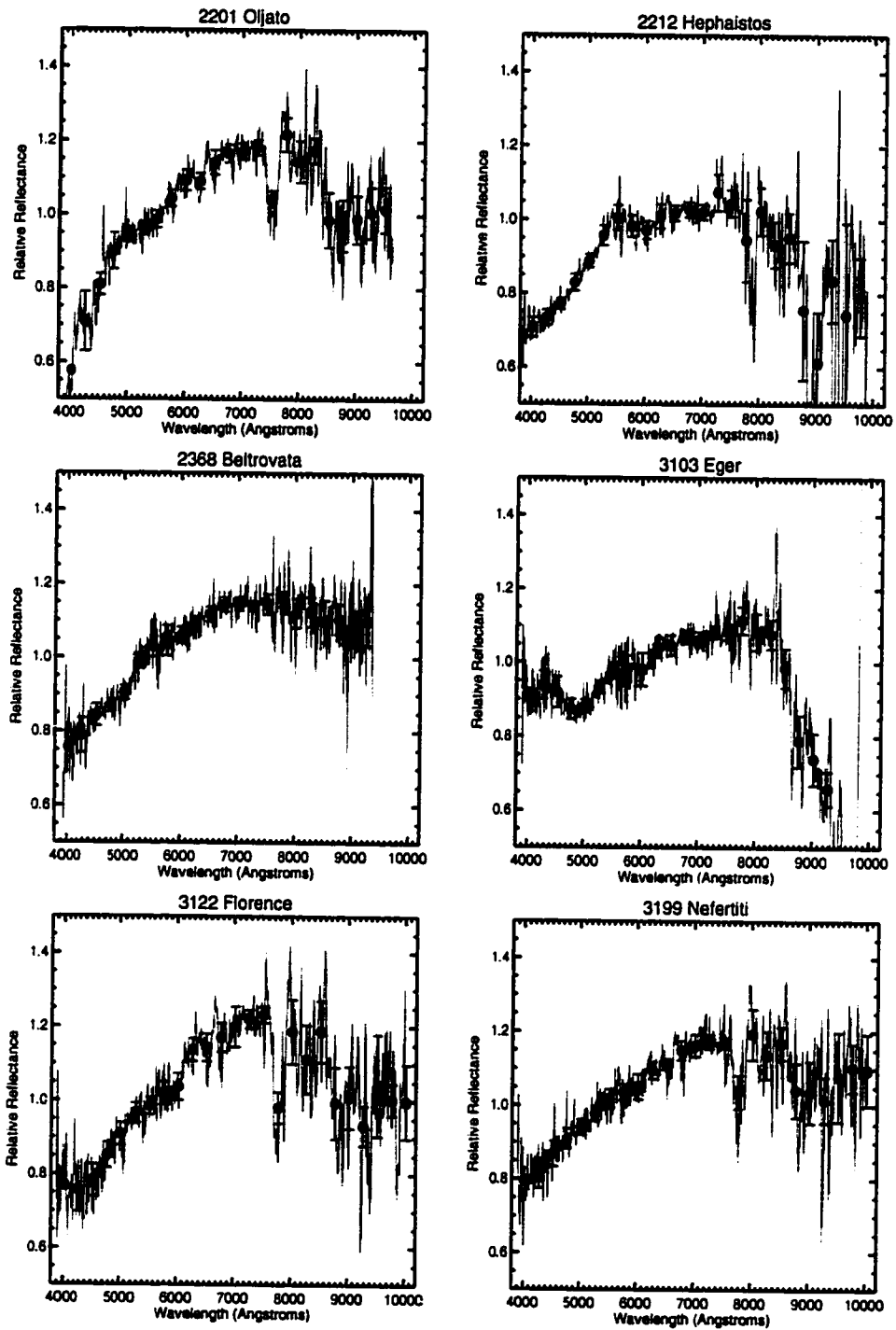


Figure 3.2: NEO reflectance spectra for 2201 Oljato, 2212 Hephaistos, 2368 Beltrovata, 3103 Eger, 3122 Florence, and 3199 Nefertiti.

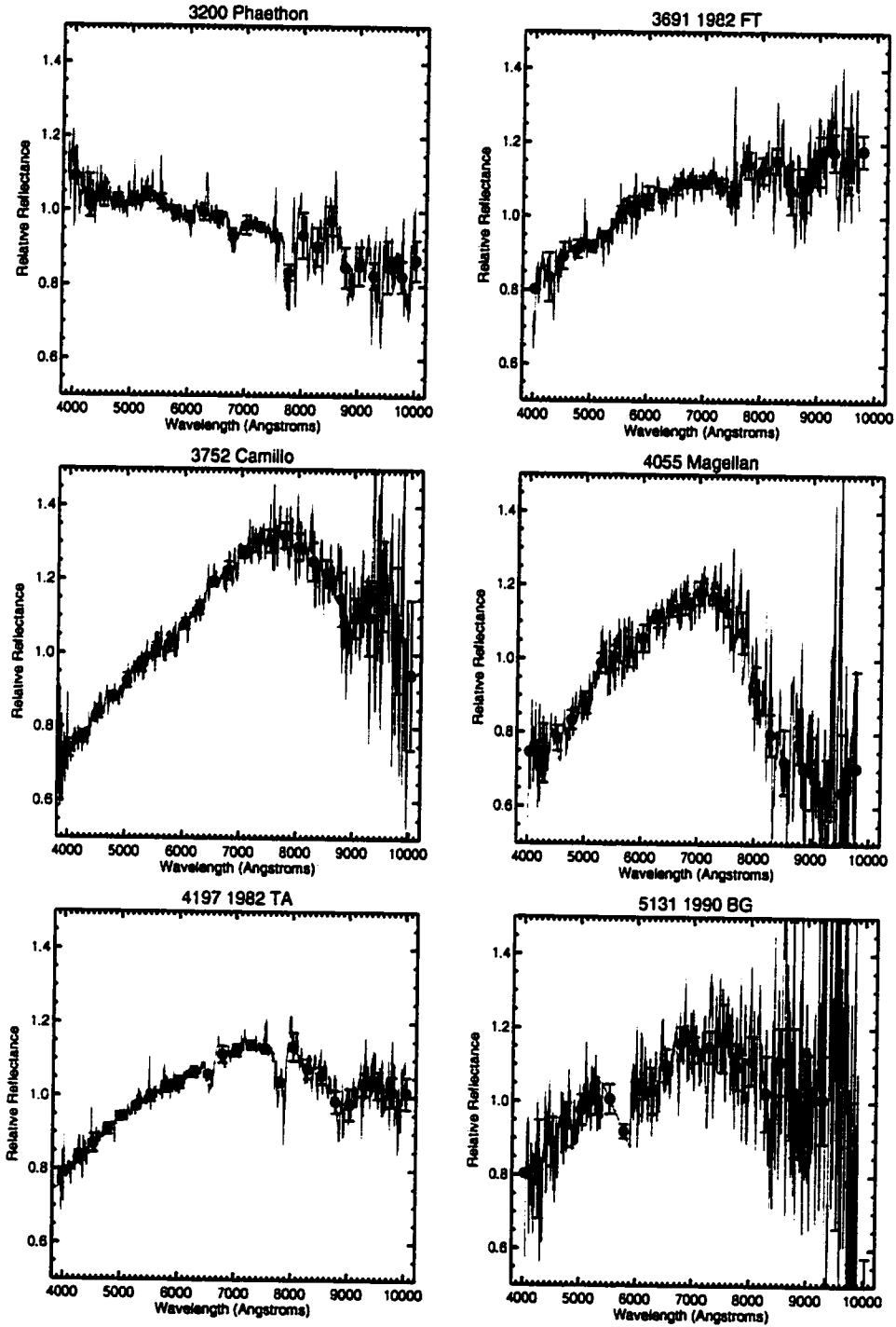


Figure 3.3: NEO reflectance spectra for 3200 Phaethon, 3691 1982 FT, 3752 Camillo, 4055 Magellan, 4197 1982 TA, and 5131 1990 BG.

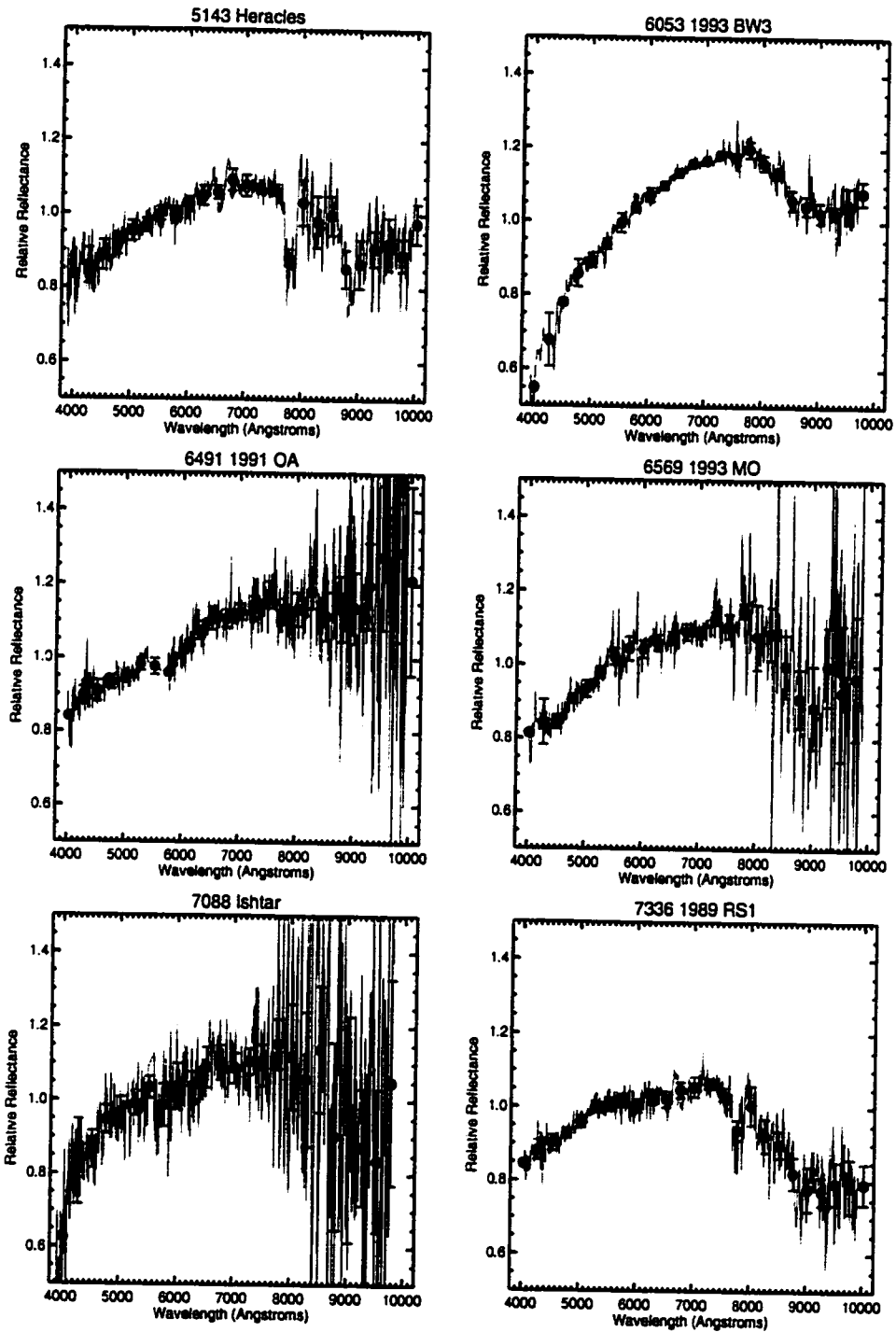


Figure 3.4: NEO reflectance spectra for 5143 Heracles, 6053 1993 BW3, 6491 1991 OA, 6569 1993 MO, 7088 Ishtar, and 7336 1989 RS1.

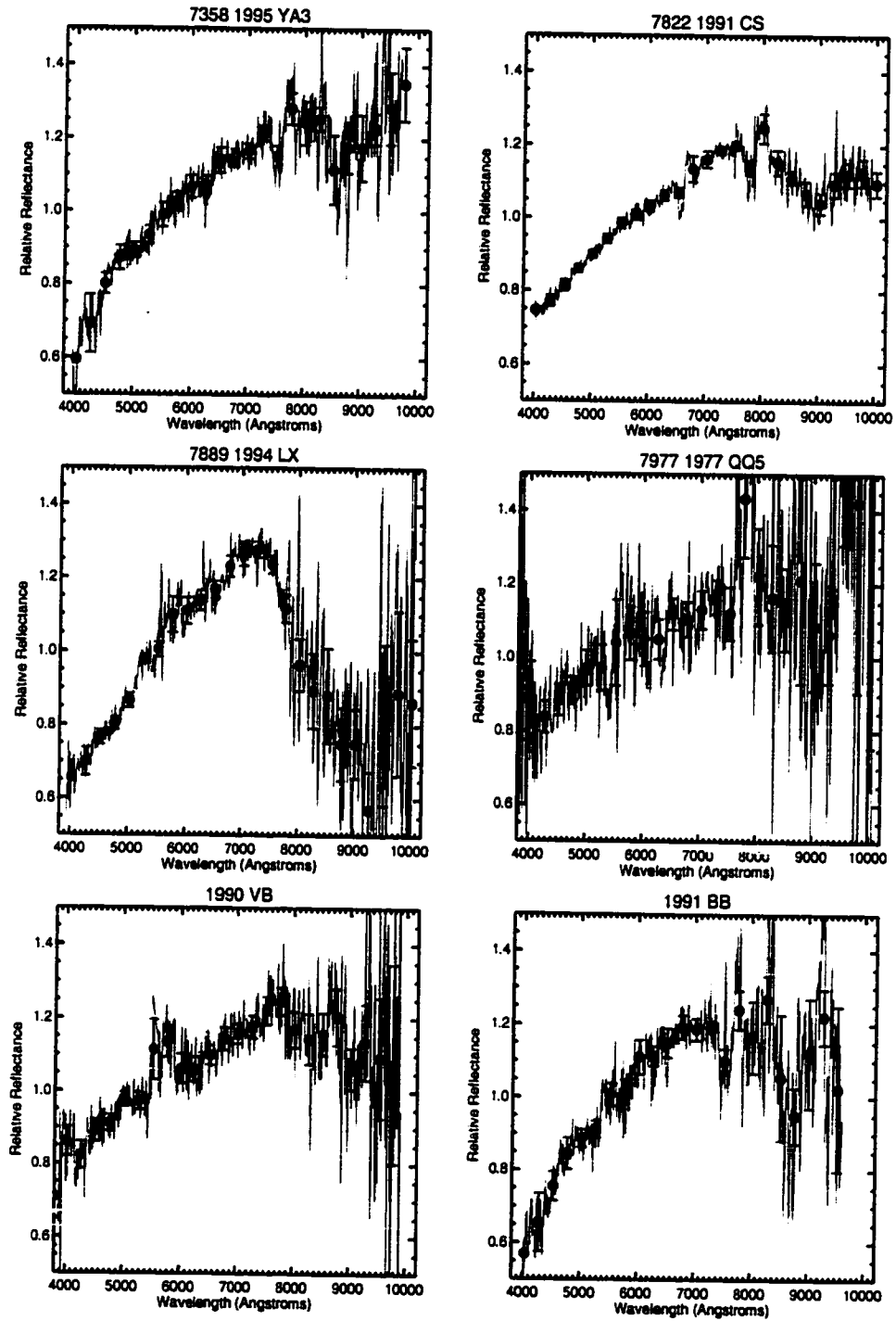


Figure 3.5: NEO reflectance spectra for 7358 1995 YA3, 7822 1991 CS, 7889 1994 LX, 7977 1977 QQ5, 1990 VB, and 1991 BB.

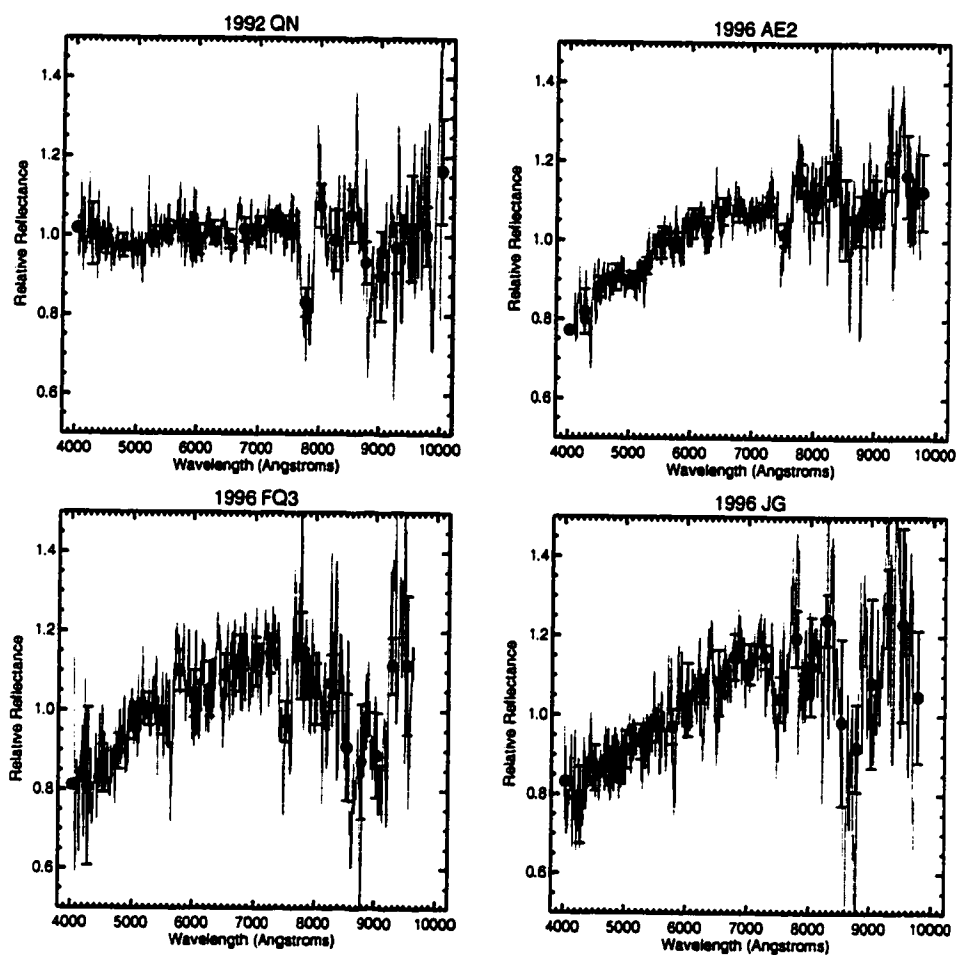


Figure 3.6: NEO reflectance spectra for 1992 QN, 1996 AE2, 1996 FQ3, and 1996 JG.

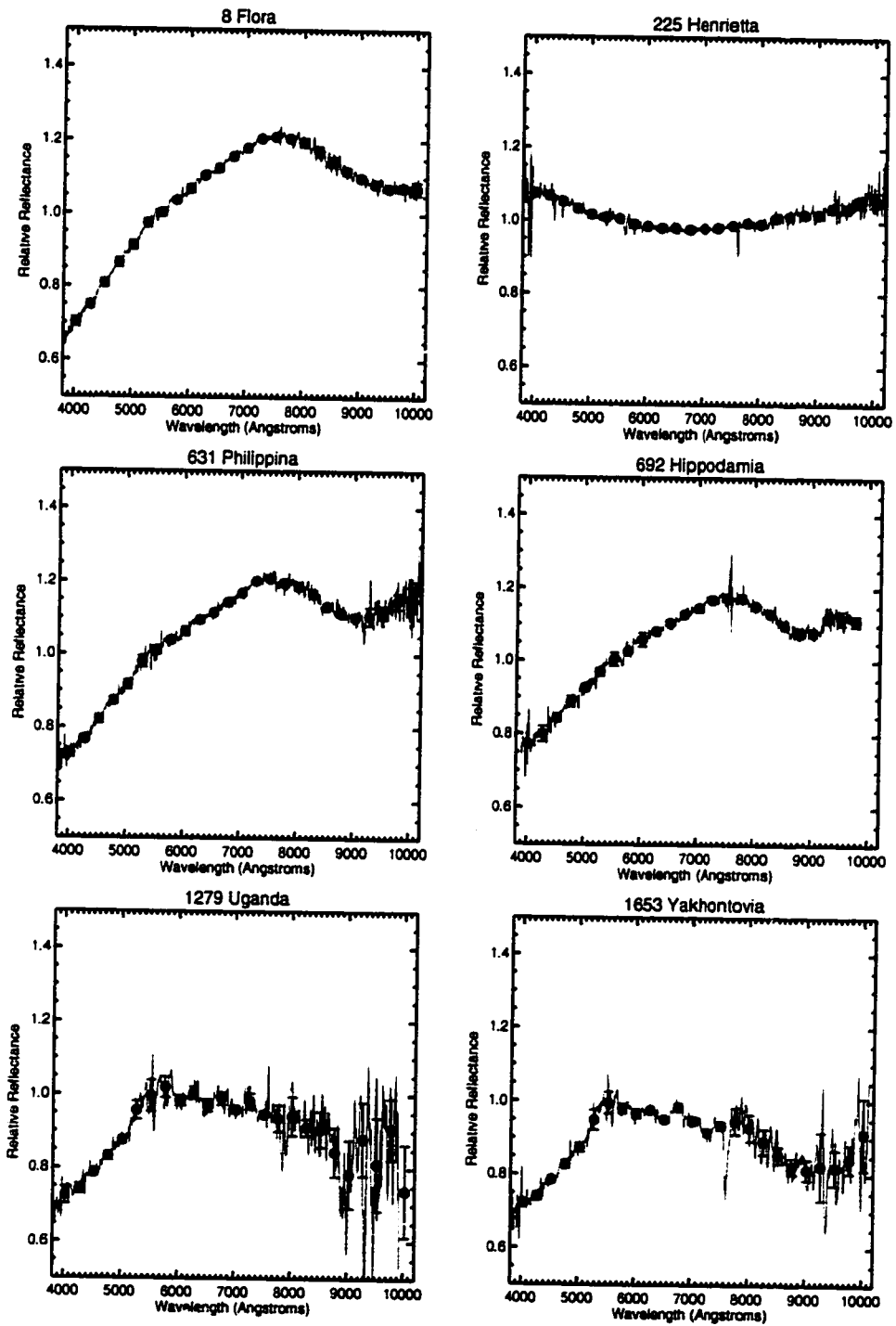


Figure 3.7: Main-belt asteroid reflectance spectra (for 8 Flora, 225 Henrietta, 631 Philippina, 692 Hippodamia, 1279 Uganda, and 1653 Yakhontovia).

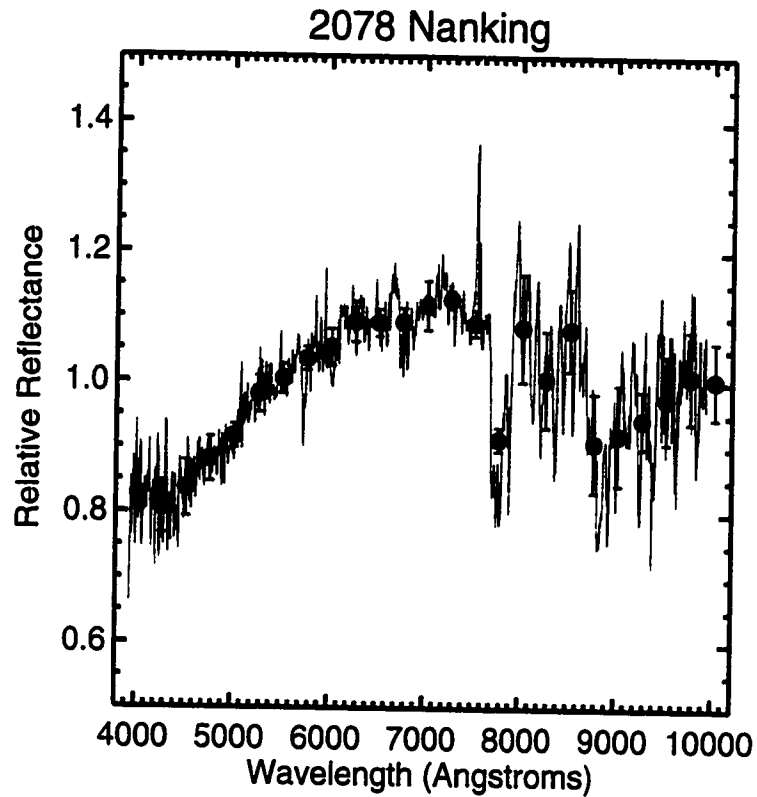


Figure 3.8: Reflectance spectrum of Mars-crossing asteroid 2078 Nanking

where a_j is the semimajor axis of Jupiter (≈ 5.2 AU), a is the semimajor axis of the object, e the object's orbital eccentricity, and i the inclination between the orbits of the object and Jupiter. The Tisserand invariant has the property that it remains nearly constant even if an object has close encounters with Jupiter. Close approaches to Jupiter can only occur if $T \leq 3$, and if stable resonances do not prevent them (as they do the Trojan asteroids). Almost all short-period comets have $T < 3$, and nearly all asteroids $T > 3$. Therefore, the dividing line $T = 3$ is often used to dynamically distinguish cometary-type orbits from asteroidal ones. For the purposes of this work, the ecliptic inclination of the object orbit was used instead of its relative inclination to Jupiter, as a simplifying assumption. This might cause an error of a few percent in T for the higher inclination objects.

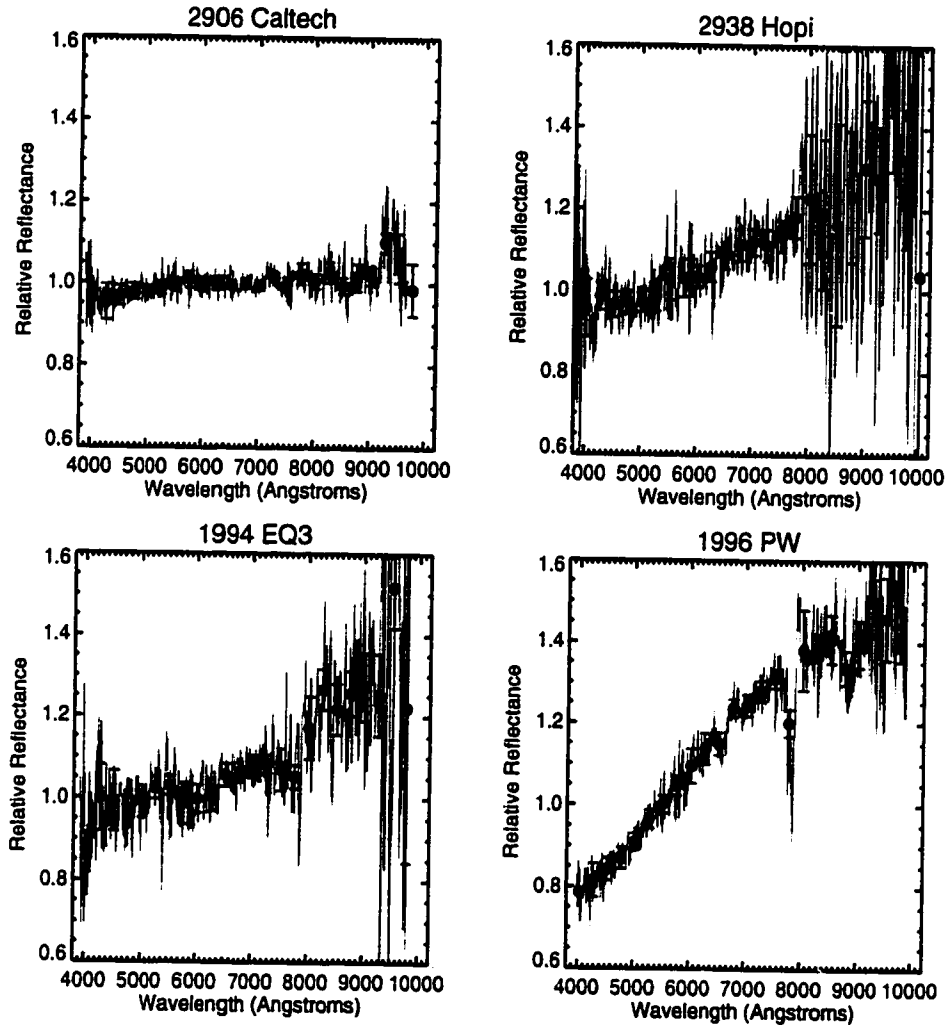


Figure 3.9: Non-NEO cometary candidate asteroid reflectance spectra (for 2906 Caltech, 2938 Hopi, 1994 EQ3, and 1996 PW).

3.1 Taxonomic Classification

A historical overview of the various asteroid taxonomic classification systems is given in Tholen & Barucci (1989). A brief summary of issues relating to these asteroid taxonomies is related in Section 1.3.

In order to taxonomically classify the objects observed during this survey according to the Tholen scheme, it would be necessary to calculate synthetic ECAS medium-band colors for them. Although early tests showed that this resulted in reasonable classifications (Hammergren 1996), and that different

Table 3.1: Physical parameters for the 34 NEOs observed

| Object | a (AU) | e | i (deg) | T^a | H (mag) | D (km) | Taxonomic Type |
|-----------------|-------------|-------|--------------|-------|--------------|-------------------|-------------------|
| 433 Eros | 1.458 | 0.223 | 10.83 | 4.58 | 11.16 | 19 | S |
| 1627 Ivar | 1.863 | 0.397 | 8.44 | 3.88 | 13.20 | 7.4 | S |
| 1864 Daedalus | 1.461 | 0.615 | 22.18 | 4.33 | 14.85 | 3.5 | SQ |
| 2062 Aten | 0.966 | 0.183 | 18.93 | 6.18 | 16.80 | 1.3 | Q |
| 2063 Bacchus | 1.078 | 0.349 | 9.43 | 5.67 | 17.10 | 1.1 | Q |
| 2102 Tantalus | 1.290 | 0.299 | 64.01 | 4.45 | 16.20 | 1.9 | SQ |
| 2201 Oljato | 2.173 | 0.713 | 2.52 | 3.30 | 15.25 | 1.90 ^b | Q? |
| 2212 Hephaistos | 2.168 | 0.833 | 11.77 | 3.10 | 13.87 | 4.9 | QR |
| 2368 Beltrovata | 2.104 | 0.414 | 5.25 | 3.63 | 15.21 | 2.9 | SQ |
| 3103 Eger | 1.406 | 0.355 | 20.94 | 4.61 | 15.38 | 1.7 | E? |
| 3122 Florence | 1.768 | 0.423 | 22.18 | 3.92 | 14.20 | 4.7 | S |
| 3199 Nefertiti | 1.575 | 0.284 | 32.98 | 4.19 | 14.84 | 3.5 | S |
| 3200 Phaethon | 1.271 | 0.890 | 22.10 | 4.51 | 14.60 | 5.20 ^b | F |
| 3691 1982 FT | 1.774 | 0.284 | 20.38 | 3.98 | 14.90 | ^c | XC |
| 3752 Camillo | 1.414 | 0.302 | 55.55 | 4.24 | 15.50 | 2.6 | SA |
| 4055 Magellan | 1.820 | 0.326 | 23.24 | 3.89 | 14.80 | 3.3 | V |
| 4197 1982 TA | 2.299 | 0.772 | 12.22 | 3.09 | 14.60 | 3.5 | QS |
| 5131 1990 BG | 1.486 | 0.570 | 36.38 | 4.21 | 14.10 | 4.9 | SQ |
| 5143 Heracles | 1.834 | 0.772 | 9.16 | 3.58 | 14.00 | 4.6 | Q |
| 6053 1993 BW3 | 2.146 | 0.529 | 21.60 | 3.44 | 15.10 | 2.8 | QS |
| 6491 1991 OA | 2.508 | 0.587 | 5.52 | 3.19 | 18.50 | 0.6 | SQ |
| 6569 1993 MO | 1.626 | 0.221 | 22.64 | 4.21 | 16.50 | 1.5 | VQS |
| 7088 Ishtar | 1.981 | 0.390 | 8.29 | 3.75 | 16.70 | 1.5 | SX? |
| 7336 1989 RS1 | 2.305 | 0.482 | 7.18 | 3.41 | 18.70 | 0.5 | RQ |
| 7358 1995 YA3 | 2.198 | 0.502 | 4.66 | 3.49 | 14.40 | 4.3 | S |
| 7822 1991 CS | 1.123 | 0.165 | 37.12 | 5.36 | 17.40 | 1.1 | S |
| 7889 1994 LX | 1.261 | 0.346 | 36.90 | 4.86 | 15.30 | 2.6 | V |
| 7977 1977 QQ5 | 2.226 | 0.466 | 25.19 | 3.38 | 15.40 | 2.7 | SX? |

Table 3.1 – *Continued*

| Object | <i>a</i> (AU) | <i>e</i> | <i>i</i> (deg) | <i>T</i> ^a | <i>H</i> (mag) | <i>D</i> (km) | Taxonomic Type |
|----------|------------------|----------|-------------------|-----------------------|-------------------|------------------|-------------------|
| 1990 VB | 2.442 | 0.528 | 14.57 | 3.26 | 15.90 | 2.1 | S |
| 1991 BB | 1.186 | 0.272 | 38.48 | 5.11 | 16.04 | 1.8 | QS |
| 1992 QN | 1.191 | 0.359 | 9.59 | 5.25 | 17.01 | 2.3 | C |
| 1996 AE2 | 1.368 | 0.257 | 37.35 | 4.59 | 19.49 | ^c | X |
| 1996 FQ3 | 2.031 | 0.471 | 1.07 | 3.66 | 21.09 | 0.2 | Q |
| 1996 JG | 1.803 | 0.661 | 5.28 | 3.77 | 19.73 | 0.3 | Q |

^a *T* = Tisserand Invariant.^b IRAS Diameter, listed in Bowell 1998.^c Diameters not computed for spectrally degenerate X-type objects.NOTE— Diameters computed from *H* and average albedo for taxonomic type, except where indicated.

Table 3.2: Physical parameters for the non-NEOs observed

| Object | <i>a</i> (AU) | <i>e</i> | <i>i</i> (deg) | <i>T</i> ^a | <i>H</i> (mag) | <i>D</i> (km) | Taxonomic Type |
|------------------|------------------|----------|-------------------|-----------------------|-------------------|-------------------|-------------------|
| 8 Flora | 2.201 | 0.156 | 5.89 | 3.64 | 6.49 | 141 ^b | S |
| 225 Henrietta | 3.382 | 0.270 | 20.90 | 2.99 | 8.72 | 124 ^b | F |
| 631 Philippina | 2.792 | 0.083 | 18.92 | 3.24 | 8.70 | 60.5 ^b | S |
| 692 Hippodamia | 3.373 | 0.176 | 26.12 | 2.97 | 9.18 | 47.7 ^b | S |
| 1279 Uganda | 2.371 | 0.208 | 5.73 | 3.51 | 12.51 | 19 | SX? |
| 1653 Yakhontovia | 2.611 | 0.323 | 4.07 | 3.33 | 11.40 | 31 | SX? |
| 2078 Nanking | 2.370 | 0.374 | 20.16 | 3.37 | 12.10 | 11 | Q |
| 2906 Caltech | 3.161 | 0.116 | 30.69 | 2.98 | 10.00 | 62.0 ^b | C |
| 2938 Hopi | 3.144 | 0.334 | 41.44 | 2.75 | 11.50 | 33 | T |
| 6144 1994 EQ3 | 4.691 | 0.367 | 5.73 | 2.87 | 11.50 | 33 | T |
| 1996 PW | 329.968 | 0.992 | 29.82 | 1.73 | 14.01 | 10 | D |

^a *T* = Tisserand Invariant.^b IRAS Diameter, listed in Bowell 1998.NOTE— Diameters computed from *H* and average albedo for taxonomic type, except where indicated.

classes of objects separated fairly well in principal component space, it was felt that the loss of information incurred by using synthetic multicolor photometry rather than spectra was undesirable. Unfortunately, there are no formal taxonomies which use reflectance spectra as inputs.

Objects were instead classified by eye using human judgment, using mean reflectance spectra for various asteroid classes (Xu et al. 1994) as guides. This is obviously a subjective process, and one for which it is difficult if not impossible to estimate uncertainties. Also, as Binzel et al. (1998) note, smaller objects seem to possess spectral properties which span the differences between taxonomic classes, which makes unique classification very difficult. Taxonomic classes for the objects observed during this survey are presented in Tables 3.1 and 3.2.

Chapter 4

Discussion of Results for Individual Objects

In all matters of opinion, our adversaries are insane.

— Mark Twain

4.1 NEOs

4.1.1 Spectra similar to ordinary chondrite meteorites

Several of the objects which are apparently roughly similar to S-type asteroids have spectra which display stronger 1- μ m absorption bands, and less reddened visual continua than typical S-type asteroids. These spectra are similar, and in some cases, for all intents identical to the spectra of ordinary chondrite meteorites. These objects include: 2062 Aten, 2063 Bacchus, 2102 Tantalus, 2201 Oljato, 2212 Hephaistos, 3199 Nefertiti, 4197 1982 TA, 5131 1990 BG, 5143 Heracles, 6053 1993 BW3, 6569 1993 MO, 7088 Ishtar, 7336 1989 RS1, 1996 FQ3, and 1996 JG. Hicks et al. (1998) also observed 2102 Tantalus, 2201 Oljato, and 6053 1993 BW3, all of which were in good agreement with observations in this work. Binzel et al. (1996) report an ordinary-chondrite-like spectrum for 2102 Tantalus, and a spectrum midway between an S-type asteroid and an ordinary chondrite for 2063 Bacchus. Lazzarin et al. (1997) also observed 2063 Bacchus, but their spectrum shows a featureless and slightly red-sloped continuum which they label as C-type. The reason for this inconsistency is unknown.

2212 Hephaistos and 2201 Oljato are traditionally known as strong cometary

candidates, owing mainly to their orbits (Weissman et al. 1989); 2212 Hephaistos has an orbit similar to that of Comet Encke and the δ Cancriids meteor stream, while that of 2201 Oljato is chaotic and possibly associated with several meteor streams (Weissman et al. 1989). Much of the excitement surrounding 2201 Oljato is due to an apparent excess of UV flux in photometry obtained by McFadden et al. (1984), and interpreted by McFadden et al. (1993) as a possible sign of fluorescent cometary emissions. Spectra from this work of 2212 Hephaistos and 2201 Oljato show fairly strong UV and $1\text{-}\mu\text{m}$ absorptions, reminiscent of absorptions seen in S- or Q-type asteroids. Since cometary nuclei are thought to be dark and neutral to red in color, with any absorption features muted by highly opaque surface materials (Luu 1993, 1994), these spectra argue strongly against a cometary origin for these objects.

4.1.2 Unusual spectra with UV- and $1\text{-}\mu\text{m}$ absorptions

Several of the objects observed in this survey display unusual spectra, with strong UV- and $1\text{-}\mu\text{m}$ absorption bands, but with relatively blue-sloped continua between 5500 \AA and 7500 \AA , where most asteroids and meteorites with silicate absorption features have significantly red-sloped continua. These objects are the NEOs 1864 Daedalus and 2212 Hephaistos, and the main-belt asteroids 1279 Uganda and 1653 Yakhontovia. The latter two were observed by Xu et al. (1995), whose spectra are similar to those of this study. 1864 Daedalus was observed by Lazzarin et al. (1997), who report an S-type spectrum for the object. I am unable to resolve this difference, although I note that their observations of 2063 Bacchus (see above) are also discrepant.

4.1.3 3103 Eger

The Apollo object 3103 Eger was reported by Wisniewski (1987) to have relatively neutral colors below about 7000 \AA . Veeder et al. (1989) determined the radiometric albedo of 3103 Eger to be in the range $0.53 - 0.63$. The high albedo and neutral colors were strongly suggestive of the E-type asteroids. Observations of this object by Gaffey et al. (1992) using continuously-variable filters (CVF) over the wavelength range $0.8 - 2.5\mu\text{m}$ seemed to confirm this classification. Gaffey et al. (1992) went on to conclude that 3103 Eger was the sole near-Earth parent

body for all enstatite achondrite (aubrite) meteorites. However, spectra obtained during the course of this survey display an unusually strong $1\text{-}\mu\text{m}$ absorption band, coupled with a relatively neutral continuum below about 8000 \AA , except for a small apparent absorption feature near 5000 \AA . The presence of such a strong feature near $1\text{-}\mu\text{m}$ – if real – is enough to invalidate the E-type classification, since the presence of ultramafic silicates is inconsistent with a putative enstatite composition. Ten separate spectra of 3103 Eger were obtained on 05/22/96. All of them show the identical shape. Three different solar analog stars were also observed on that night; ratios using these stars all show the same features and continuum slope. It is difficult to reconcile the spectra obtained in this work to those of Gaffey et al. (1992) unless one invokes an observational or data reduction error. This issue remains unresolved.

4.2 Mars Crosser – 2078 Nanking

The Mars crossing asteroid 2078 Nanking was observed by Xu et al. (1995), and found to have a spectrum similar to an H-chondrite. This work confirms those conclusions. It is noted that many NEOs also have spectra similar to the H- or L-chondrites, and that perhaps 2078 Nanking is evidence of a link from the main asteroid belt through a Mars crossing stage.

4.3 Non-NEO Cometary Candidates

Four non-NEO objects with unusual orbits were observed during the course of this survey. 2906 Caltech, 2938 Hopi, 1994 EQ3, and 1996 PW all have orbits which either cross or approach Jupiter's orbit, thus making them excellent candidates for extinct comets. All four of these objects have relatively featureless, red-sloped continua consistent with either the C, P or D spectral classes, and with known cometary nuclei (Luu 1993, 1994).

Chapter 5

Spectral Trends Among S-type Objects

Some circumstantial evidence is very strong, as when you find a trout in the milk.

— Henry David Thoreau

5.1 Space Weathering

Surface processes active on the Moon cause a lowering of albedo, a reddening of the spectral continuum, and a decrease in absorption band depth in regolith compared to lunar rocks (cf. Pieters et al. 1993). This process or collection of spectrally-altering processes is known as “space weathering,” and has been proposed as one reason for the differences between asteroid and meteorite spectra, particularly for the spectral differences between S-type asteroids and the ordinary chondrite meteorites.

Pieters et al. (1993) found that lunar space weathering appears to be correlated to surface alterations, and that it is in only the finest fraction of lunar regolith that the red-sloped continuum is produced. Space weathering, at least on the Moon, appears to be directly related to regolith maturation. Galileo spacecraft images of main-belt S-type asteroid 951 Gaspra show color trends and differences in albedo and absorption band depth consistent with the nature (but not necessarily the magnitude) of lunar space weathering, demonstrating unambiguously the existence on S-type asteroids of some form of surface spectral alteration.

Since larger bodies will generally retain ejecta more effectively than smaller bodies, a dependence of regolith maturity on size may be expected to exist. Additionally, if small NEOs are produced from relatively recent catastrophic disruption events, they may be even less affected by potential space weathering. Previous investigations of small main-belt asteroids and NEOs have shown some interesting relationships between spectral slope, absorption band depth, and size. McFadden et al. (1984) found that small S-type NEOs displayed stronger absorption band depths than larger main-belt asteroids. In a study of small main-belt asteroids, Xu et al. (1995) also found this relation to be the case, but they interpret this effect as being due mainly to an increase in the diversity of spectral band strengths among the small S-type asteroids. Binzel et al. (1998) reiterate this supposition. In an investigation of 39 S-type asteroids ranging in size from $\sim 30 - 300$ km in diameter, Gaffey et al. (1993) too observed an increase in absorption band depth for smaller asteroids. They found no correlation between albedo and size, and a slight negative correlation between spectral slope and size (such that the smaller asteroids had relatively redder continua). Since this trend is opposite what might be expected from space weathering due to regolith maturity, they conclude that it is unlikely that the more steeply-sloped asteroids could be plausible ordinary chondrite parent bodies.

5.2 Modified Gaussian Model Fits

To study the relationships between spectral characteristics and object size, I first fit NEO spectra with a 5-parameter, two-component Modified Gaussian model, following those presented in Sunshine et al. (1990). A Modified Gaussian model is one in which an absorption band is fit by a Gaussian in inverse-energy - log reflectance space. In this work, a single Modified Gaussian was superimposed on a continuum which was linear in energy - log reflectance space. Figure 5.1 displays some example fits which result from the application of this model. In most cases, this 5-parameter fit does a wonderful job at fitting both the visual continuum and 1- μ m band shape, returning reduced χ^2 values near 1.1-1.3. The fit does break down on objects with unusual spectra like 1864 Daedalus, or for obviously non-S-type objects. The model was also fit to spectra of S-type objects from Xu et al. (1995) for comparison. Those data include spectra of 5 NEOs;

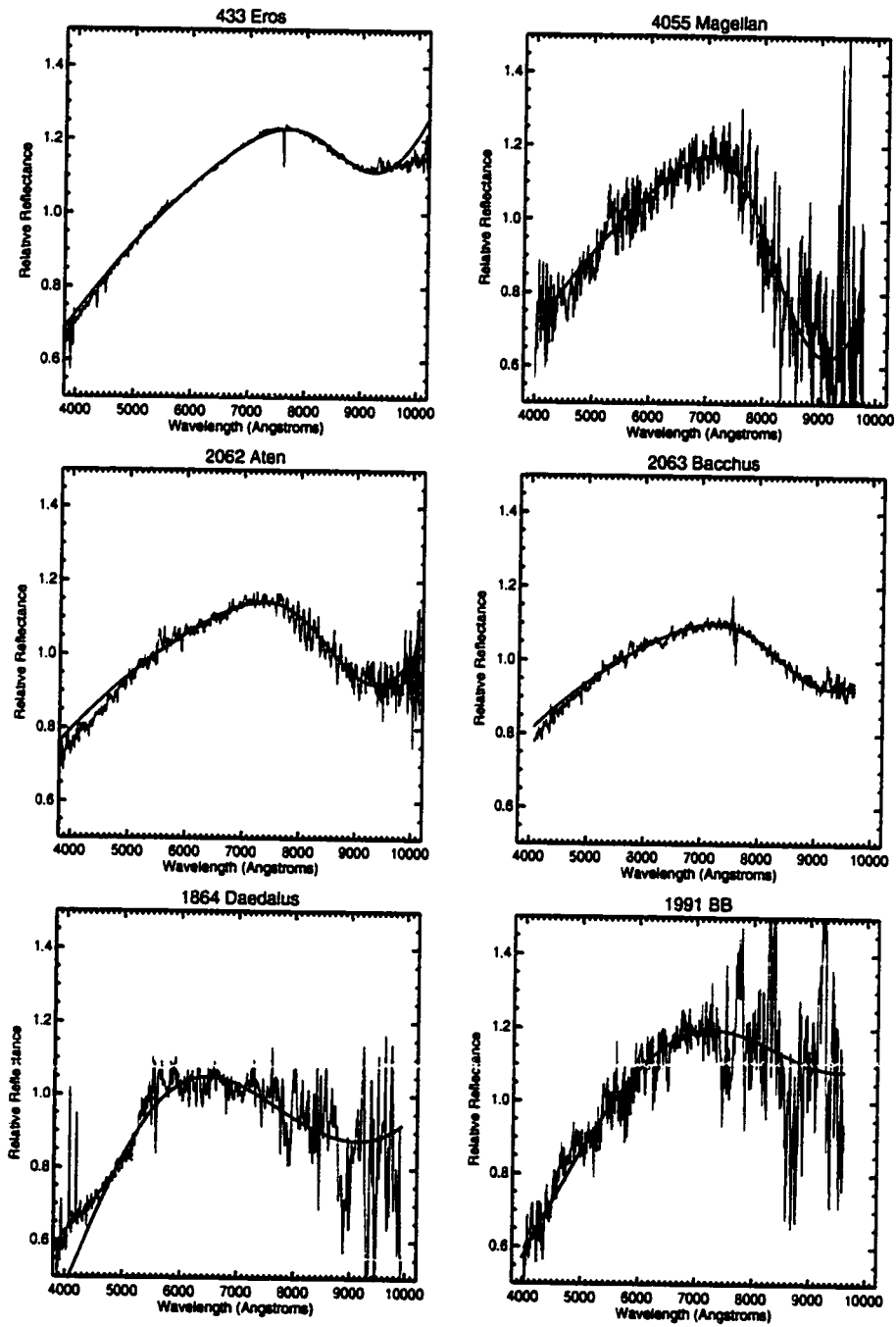


Figure 5.1: NEO spectra have been fit by a five-parameter, two-component Modified Gaussian model. S- and Q-type objects are well fit.

most others are of main-belt asteroids.

5.3 Spectral Trends with Diameter

The plot of 1- μm band strength versus size is shown in Figure 5.2. There is a slight trend towards deeper absorption bands for smaller objects. A formal fit to the equation

$$\text{BandStrength} = a_{str} + b_{str} \times \log_{10} D \quad (5.1)$$

yields $a_{str} = -0.230 \pm 0.001$ and $b_{str} = 0.0295 \pm 0.0007$, with a linear correlation coefficient r of 0.43. Most of the scatter around this fit is apparently intrinsic to the population of objects, and not due to observational errors.

A plot of 1- μm band center versus size is presented in Figure 5.3. While a slight trend towards bluer band centers with smaller diameters is apparent in a formal fit, the linear correlation coefficient r of 0.14 shows this trend to be relatively insignificant compared to the scatter in the data. The parameters of a formal log-linear fit to the equation

$$\text{BandCenter} = a_{ctr} + b_{ctr} \times \log_{10} D \quad (5.2)$$

are $a_{ctr} = 9243 \pm 4\text{\AA}$ and $b_{ctr} = 38 \pm 2$. If real, this trend would seem to imply that larger objects (or at least the spectrally important components of their surfaces) are relatively enriched in olivine or clinopyroxene. Hörz & Cintala (1997) have noted that such a trend towards olivine enrichment may be expected on asteroidal surfaces due to certain regolith processes, such as the selective crystallization of olivine relative to pyroxene in impact melts, and the production of much larger quantities of fine-grained olivine relative to pyroxene in comminution experiments.

Figure 5.4 presents a plot of “visual slope” versus size. The “visual slope” is a measure of the redness of a spectrum, and refers to the reflectivity gradient calculated in the 5000–7500 \AA region, as introduced by Luu & Jewitt (1990). For objects larger than ~ 6 km, the trend towards redder visual slopes at larger diameters noted by Gaffey et al. (1993) is also observed, but quite strikingly, the reverse relationship is seen for smaller objects. A formal log-linear fit to those objects smaller than 6 km in diameter yields the relation:

$$\text{VisualSlope}(D < 6\text{km})(\% \text{ per } 10^3 \text{\AA}) = (6.19 \pm 0.03) + (8.20 \pm 0.06) \times \log_{10} D(\text{km}) \quad (5.3)$$

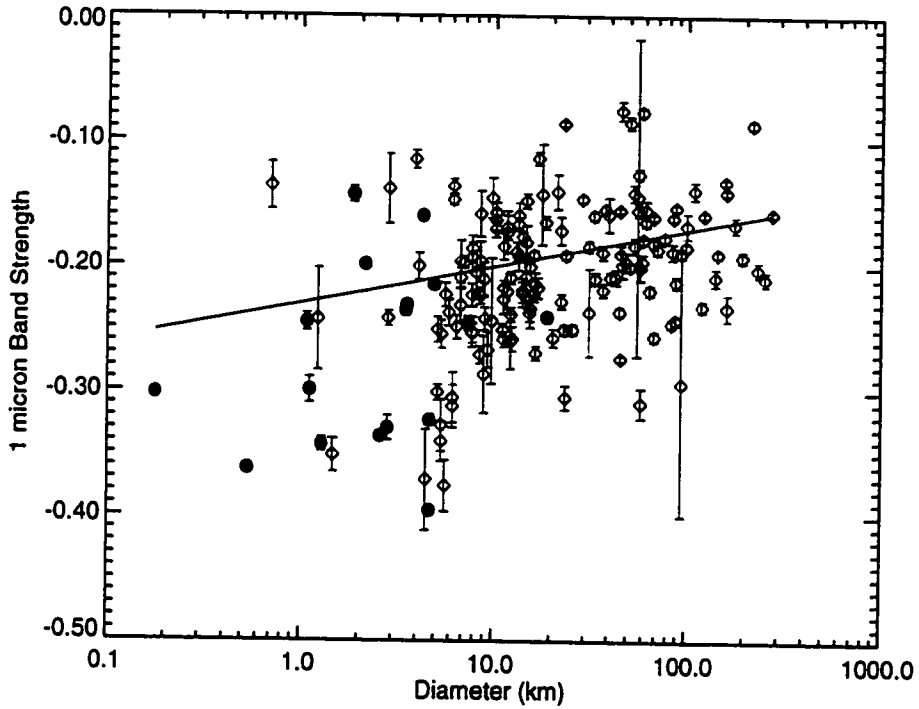


Figure 5.2: Plot of 1- μm band strength vs. size. NEOs observed in this survey are plotted as solid circles, and S-type asteroids from Xu et al. (1995) (mostly main-belt asteroids, but including five NEOs) are indicated by hollow diamonds. A log-linear fit to these data is shown.

For objects larger than 6 km, the fit is

$$\text{VisualSlope}(D \geq 6\text{km})(\% \text{ per } 10^3 \text{\AA}) = (12.16 \pm 0.02) + (-1.09 \pm 0.01) \times \log_{10} D(\text{km}) \quad (5.4)$$

This seems to indicate that the smaller S-type objects are systematically more spectrally similar to the ordinary chondrites than larger objects not only in terms of band depth but also visual continuum slope. It may be that there are two competing effects altering asteroid spectra, one which causes objects smaller than ~ 6 km to redden with increasing size, and another which produces the opposite size dependence for larger objects.

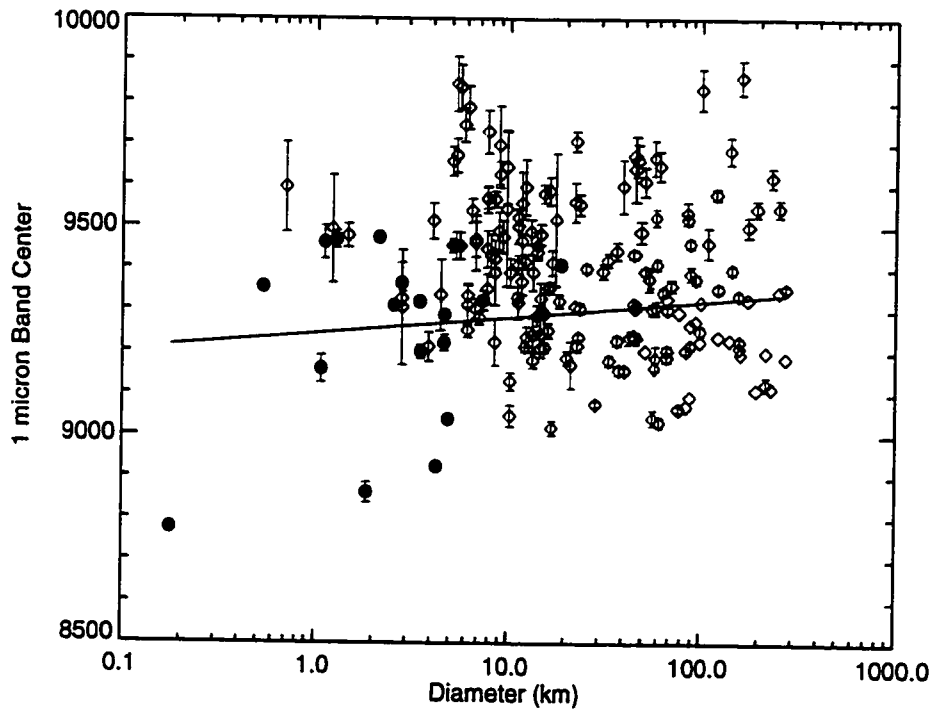


Figure 5.3: Plot of $1\text{-}\mu\text{m}$ band center vs. size. NEOs observed in this survey are plotted as solid circles, and S-type asteroids from Xu et al. (1995) (mostly main-belt asteroids, but including five NEOs) are indicated by hollow diamonds. A log-linear fit to these data is shown.

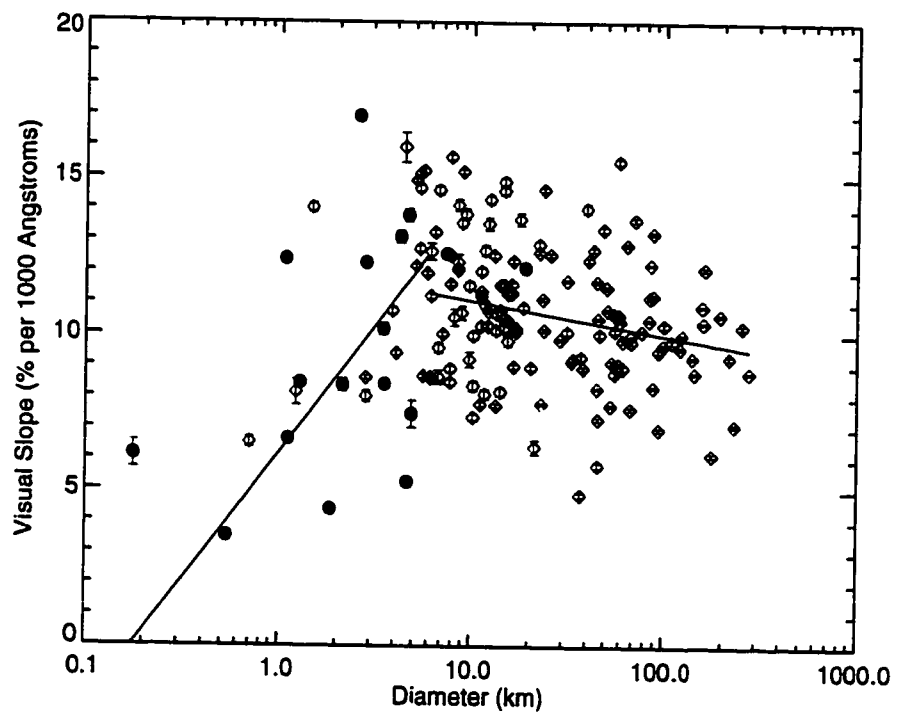


Figure 5.4: Plot of visual slope vs. size. Objects observed in this survey are plotted as solid circles, and S-type asteroids from Xu et al. (1995) are indicated by hollow diamonds. Separate fits to the <6 km and ≥ 6 km regimes are shown.

Chapter 6

Debiasing Asteroid Taxonomic Distributions

Truth is a good thing; but beware of barking too close to the heels of an error, lest you get your brains kicked out.

— Samuel Taylor Coleridge

6.1 Introduction

To some degree, the distribution of taxonomic types among the NEOs should resemble the distribution of types in its source population. In a simple universe, the NEO population would be identical to its progenitor population. There are several factors which complicate this prospect, however.

First, the NEOs may derive from several distinct sources. The two most commonly suggested sources are main-belt asteroids and extinct comets. While main-belt asteroids have been fairly well studied spectroscopically, only a handful of comet nuclei have been similarly observed (Luu & Jewitt 1990). Extinct or dormant comets are even less well characterized, with only one definite example known (4015 Wilson-Harrington, e.g., Fernández et al. 1997). However, it is easier to state what a comet nucleus should *not* look like: comets contain copious amounts of organic material, which should render their surfaces dark and drastically reduce the contrast of any spectral absorption features (Luu 1993). There is no known process which would selectively remove this organic component (Rahe et al. 1994), so objects which have high albedos, or those which have strong spectral absorptions, can almost certainly be excluded as candidates for extinct

comets. We don't know very well what comet nuclei look like, but we do have a good idea of what they *don't* look like.

Second, the average size of NEOs which have been taxonomically classified is much smaller than similarly studied main-belt asteroids. If the taxonomic distributions are size-dependent, then it may be difficult to directly compare NEOs with such potential source populations. A possible taxonomic size dependence is amenable to observational investigation, however, so as long as this problem is acknowledged and taken into account, it may be possible to proceed with a comparison of taxonomic distributions.

Third, the mechanism which delivers progenitor objects into NEO orbits may have some compositional dependence. For example, stronger objects may better survive collisions which propel them into orbital resonances, leading to an over-representation of materially strong objects in the NEO population. The importance of material strength versus self-gravitation in regards to asteroid collisional survivability is a subject of some debate (see Love & Ahrens 1996, and references therein). However, most researchers believe that the transition from strength- to gravity-dominance in controlling asteroid structure occurs somewhere between diameters of 250 m up to a few km. Any possible strength-dependent delivery mechanism should thus be important only at smaller sizes, but since this size range includes the average size of NEOs, one must keep in mind this potential bias to the taxonomic distribution.

Alternatively, surface properties may affect the delivery of objects into resonances via the Yarkovsky effect (Farinella et al. 1998, Vokrouhlický & Farinella 1998). This effect, which is due to the offset between the direction of the absorption of sunlight and the reradiation of infrared radiation by a rotating body, is most significant for objects ranging between 0.1 and 100 m in diameter (Farinella et al. 1998). The strength of the effect is dependent on the insulating properties of the regolith. Additionally, those objects with longer collisional lifetimes will experience greater total orbital excursions due to the Yarkovsky effect than shorter-lived objects. This could cause taxonomic biases among the smallest solar system objects subject to this effect.

A fourth and perhaps most severe complication is that the observed populations of NEOs and main-belt asteroids are subject to strong observational

selection effects. Since most detection and physical observations are performed at visual or near-infrared wavelengths, the most prominent bias is that favoring objects with higher apparent visual brightnesses. The apparent brightness of any given object is dependent on several factors, including the geometric circumstances of its apparition (i.e., the Sun-object and Earth-object distances, and the Sun-object-Earth phase angle), and several intrinsic properties of the object (i.e., the object's diameter, slope parameter G , and geometric albedo in the appropriate wavelength band). The apparition geometry is in turn dependent on the orbital elements of the object, and the time at which the object is observed.

To provide a coherent sample for comparison purposes, the debiasing procedure (which will be described in the following sections) has also been performed on the observed taxonomic distributions of the main-belt asteroids.

6.2 Debiasing Methodology

The number of objects which have been taxonomically classified can be expressed as

$$N_{tax}(a, e, i, H, t) = N_{true}(a, e, i, H, T) P_{tax, total}(H) P_{det, total}(a, e, i, H, T), \quad (6.1)$$

where N_{true} represents the total number of objects, $P_{tax, total}$ the probability that an object which has already been detected has also been taxonomically classified (this may also be regarded, somewhat inaccurately, as the taxonomic completeness), and $P_{det, total}$ the detection completeness (or equivalently, the probability that an object has been detected in the first place). Before an object's taxonomic class is known, its apparent magnitude is typically calculated using the slope parameter appropriate for the S-type asteroids. Therefore, the selection of targets for taxonomical classification observations (which is almost always apparent magnitude-limited) is *not* dependent on taxonomy. Since various spectroscopic surveys have specifically targeted certain asteroid families, regions of the main belt, or orbital classes of objects (including NEOs), P_{tax} is somewhat dependent on the orbital elements of an object. P_{det} is dependent on properties which are themselves dependent on taxonomy, so P_{det} must be derived using models of the object population.

6.3 The Detection Simulation

The simulation I perform in this section follows the technique presented in Rabinowitz (1993), but extended to allow for differences in geometric albedo p , slope parameter G , and color for objects of different taxonomic types. Orbital element space was split up into 3024 cells: 24 bins in semimajor axis, 0.2 AU wide and ranging from 0.7 to 5.2 AU; 9 bins in eccentricity, 0.1 units wide and ranging from 0 to 0.9; and 14 bins in inclination, 5° wide and ranging from 0° to 70° . Test objects were created with orbital elements distributed uniformly within each bin; the remaining orbital elements Ω , ω , and M were chosen randomly from a uniform distribution between 0° and 360° . Object positions were then calculated analytically for a randomly chosen time of observation. If an object was found within 30° of the opposition point, it was scored as a “potential detection” and the circumstances of its apparition were recorded. The 30° limit was chosen as being representative of the observing practices of the major asteroid and NEO detection programs (Rabinowitz 1993, Helin & Dunbar 1990).

This process was continued within each orbital element bin until either 1000 objects were scored as “potential detections,” or 1 million trials took place. In total, 243,918,704 objects were tested, with 2,954,807 scored as potential detections. The simple ratio of number “potentially detected” to number tested is a measure of the probability that an object with elements (a,e,i) is situated so that it is potentially detectable at any given time. This is displayed in Figure 6.1. In general, objects with lower inclinations and larger semimajor axes are more likely to be found close to the opposition point than objects with high inclinations and orbits closer to the Earth.

Another such run was performed, simulating the velocity-dependent detection criteria characteristic of Spacewatch NEO searches (Jedicke 1996). In this case, only those objects exceeding certain velocity thresholds were counted as potential detections. In this run, 1,987,727 “potential detections” were scored out of 1,717,326,208 trials. Figure 6.2 displays the orbital element dependence of the potential detection probability for the Spacewatch-type simulation. Following the procedure outlined in Rabinowitz (1993), each object potentially detected with elements (a,e,i) can be characterized by a magnitude offset $V^* - H$, which is dependent on the circumstances of the apparition. Using the magnitude law

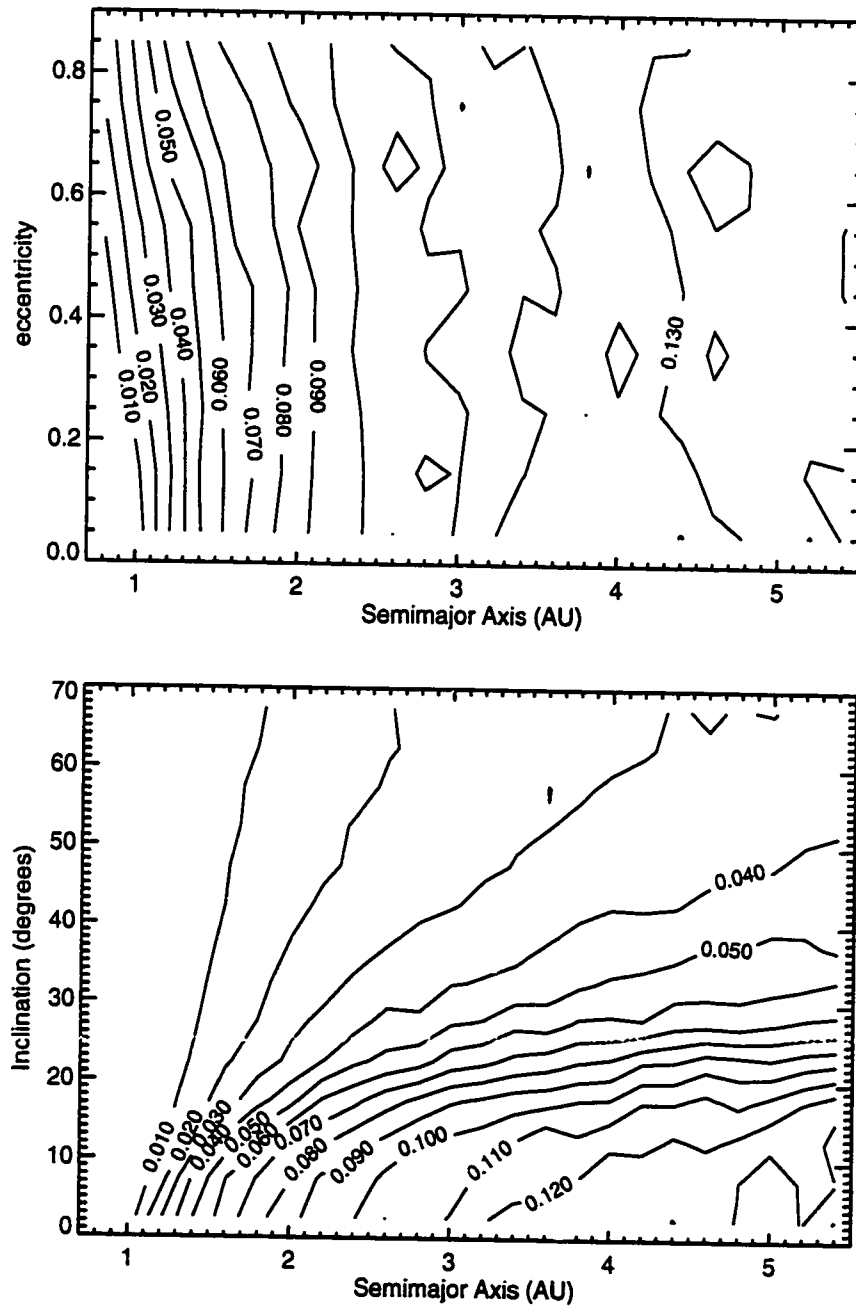


Figure 6.1: Probability that an object will be potentially observed at any given time, dependent on orbital semimajor axis, eccentricity, and inclination. The top e vs. a contour plot is for $i = 0^\circ$, the bottom i vs. a contour plot is for $e = 0$.

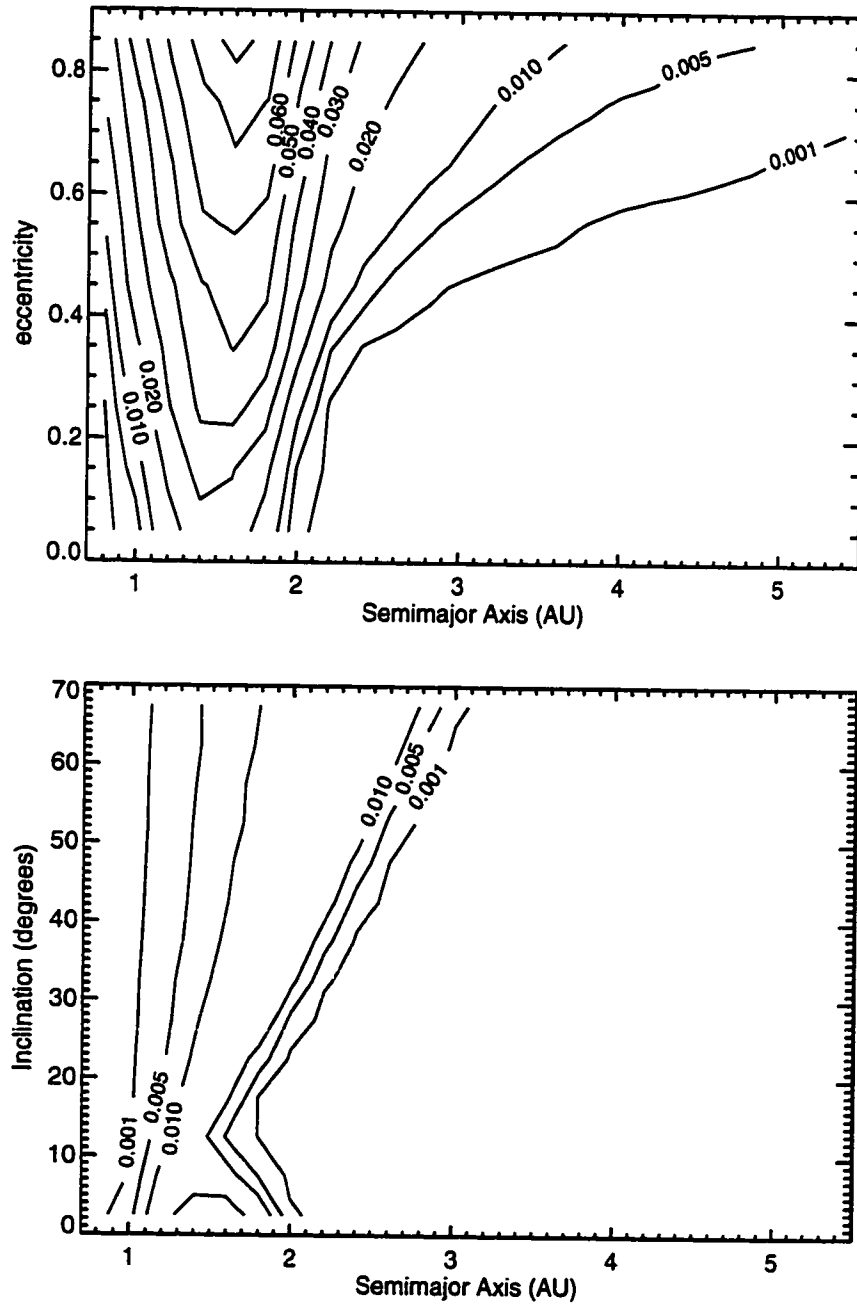


Figure 6.2: Fraction of objects potentially observed at any given time, dependent on orbital semimajor axis, eccentricity, and inclination, for a Spacewatch-type set of velocity-dependent detection criteria. The top e vs. a contour plot is for $i = 0^\circ$, the bottom i vs. a contour plot is for $e = 0$.

Table 6.1: Average geometric albedo p , slope parameter G , and $B - V$ colors for 12 taxonomic classes.

| Taxonomic Class | p | G | $B - V$ (mag) |
|--------------------|-------|-------|------------------|
| A | 0.262 | 0.350 | 1.042 |
| B | 0.071 | 0.100 | 0.672 |
| C | 0.052 | 0.100 | 0.702 |
| D | 0.043 | 0.100 | 0.751 |
| E | 0.422 | 0.350 | 0.706 |
| F | 0.042 | 0.100 | 0.632 |
| G | 0.074 | 0.100 | 0.744 |
| M | 0.150 | 0.190 | 0.703 |
| P | 0.043 | 0.100 | 0.700 |
| Q | 0.212 | 0.250 | 0.834 |
| S | 0.175 | 0.250 | 0.859 |
| V | 0.197 | 0.350 | 0.800 |

in Bowell et al. (1989), $V^* - H$ is calculated through

$$V^* - H = 5 \log(r\Delta) + \delta_{\text{trail}} - 2.5 \log[(1 - G(T))\Phi_1(\alpha) + G(T)\Phi_2(\alpha)], \quad (6.2)$$

where V^* is the apparent, trailed magnitude of the object, H is the absolute magnitude of the object, r and Δ the heliocentric and geocentric distances respectively, δ_{trail} is the trailing loss due to object motion during an exposure, G is the slope parameter, α the Sun-object-Earth phase angle, and Φ_1 and Φ_2 given by equation (A5) in Bowell et al. (1989). Since G is dependent on object surface characteristics (and taxonomic class T), so is the magnitude offset $V^* - H$. Table 6.1 lists average parameters for different taxonomic classes. It must be noted here that the X class represents those objects with E, M, or P-type spectra for which no albedo information is available, and since without albedo information it is impossible to derive sizes, X class objects are not explicitly handled as a unique group through the rest of these debiasing steps. Geometric albedo P and slope parameter G were derived from diameters and absolute magnitudes in Bowell (1998). $B - V$ colors were derived through synthetic photometry using

average spectra in Xu et al. (1995).

The trailing loss δ_{trail} is a function of exposure time, object apparent velocity, and atmospheric seeing, and becomes important when an object moves more than a seeing disk during an exposure. Trailing loss is calculated by the following fit to data presented in Figure 2 of Jedicke & Herron (1997):

$$\delta_{trail} = 1.25[\sqrt{(\xi - 0.035)^2 + 0.04262} + (\xi - 0.035)], \quad (6.3)$$

and

$$\xi = \log(t_{exp}\omega / FWHM), \quad (6.4)$$

where t_{exp} is the exposure time, ω the apparent velocity, and $FWHM$ the full-width-half-maximum of the seeing disk, in the appropriate units. This expression has the advantage over the one presented in Jedicke & Herron (1997) in that this function is continuous rather than discrete.

The detection probability for an object of apparent magnitude V^* at a *single* apparition and in a single observation is

$$P_{det}(a, e, i, V^*, T) = V^*(a, e, i, T) \epsilon_{detect}(V^*) P_{pot}(a, e, i) (A_{det}/A_{survey}), \quad (6.5)$$

where ϵ_{det} is the threshold function for detection, $P_{pot}(a, e, i)$ is the probability that an object is positioned so as to be “potentially detectable,” and A_{det}/A_{survey} is the ratio of the active detector area to the total survey area.

The threshold function was modeled in the form

$$\epsilon_{detect}(V^*) = 0.5(1 - \text{erf}[(V^* - V_{50})/\sigma]), \quad (6.6)$$

where erf is the standard error function, V_{50} is the magnitude at 50% detection efficiency, and σ is a measure of the steepness of the dropoff in detection efficiency. For simulations of Spacewatch-type programs utilizing CCD's, V_{50} was set to 20.77, and σ to 0.230 to match the threshold function described in Jedicke & Herron (1997). For simulations of photographic search programs, V_{50} was set to 16.5, and σ to 0.7.

The individual detection probability for any object with elements (a, e, i) and absolute magnitude H is calculated as

$$P_{det}(a, e, i, H, T) = 1 - \prod_n (1 - P_{det}(a, e, i, V_n^*, T)). \quad (6.7)$$

It is now possible to estimate $P_{det,total}$ by calculating the probability that any object would be observed given the effective numbers of search exposures which have been made by the various asteroid and NEO search programs to date. At this point, it is necessary to derive the observed detection completeness as a function of absolute magnitude. This is the only part of the entire debiasing process which relies on model distributions of size, orbital elements, and taxonomic types. The (estimated) true size and orbital distributions for the main-belt asteroids were taken from Jedicke (1996). The main-belt was further broken down into three zones to allow the ratio between “bright” (i.e., S-type) asteroids and “dark” (C-type) asteroids to vary with heliocentric distance. The definitions of these zones, and the bright/dark ratios for the main belt were taken from Jedicke & Metcalfe (1998). The (estimated) true size and orbital distributions for the NEOs were taken from Rabinowitz (1993), with the numbers of “bright” and “dark” objects being set equal. I note here that it would be possible to rederive the estimated true distributions of the main-belt and NEO populations given the detection simulations which have been performed, but those results are extremely sensitive to the assumptions made about detector performance and other search criteria, and it was felt that such an undertaking was beyond the immediate scope of this work. The derivation of a taxonomic bias is less sensitive to such underlying assumptions, because it is the *ratio* of completenesses between different taxonomic classes that is important, and not the *absolute* level of completeness of any one of them.

The total detection probability may be expressed as

$$P_{det,total}(a, e, i, H, T) = 1 - \prod (1 - P_{det}(a, e, i, V^*, T))^{n_{exp}}, \quad (6.8)$$

where n_{exp} is the effective number of exposures, which was estimated to be $\sim 1,000$ CCD and $\sim 3,500$ photographic exposures for main asteroid belt searches, and $\sim 7,000$ CCD and $\sim 15,000$ photographic exposures for the NEOs.

The taxonomic classification probability $P_{tax,total}$ is derived by calculating the fraction of known objects at a given magnitude which have been taxonomically classified. Since there may be some dependence of P_{tax} on orbital elements, it is necessary to split up the population of NEOs and main-belt asteroids into regions which have been similarly targeted. Table 6.2 lists 22 zones in which the selection effects are judged as most nearly identical. The boundaries of these zones are

Table 6.2: Orbital Element Zones

| Zone | Description | Criteria |
|------|----------------|---|
| ATE | Atens | $a \leq 1.0$ |
| APO | Apollos | $q \leq 1.0$ |
| AMO | Amors | $q \leq 1.3$ |
| HU | Hungaria Group | $1.78 \leq a \leq 2.00, e \leq 0.18, 16^\circ \leq i \leq 34^\circ$ |
| MC | Mars Crossers | $q \leq 1.666$ |
| FL | Flora Family | $2.10 \leq a \leq 2.30, i \leq 11^\circ$ |
| PH | Phocaea Group | $2.25 \leq a \leq 2.50, e \geq 0.10, 18^\circ \leq i \leq 32^\circ$ |
| NY | Nysa Family | $2.41 \leq a \leq 2.50, 0.12 \leq e \leq 0.21, 1.5^\circ \leq i \leq 4.3^\circ$ |
| VES | Vesta Family | $2.28 \leq q \leq 2.50, 0.04 \leq e \leq 0.16, 5^\circ \leq i \leq 8^\circ$ |
| I | Main Belt | $2.30 < a \leq 2.50, i < 18^\circ$ |
| PAL | Pallas Zone | $2.50 < a < 2.82, 33^\circ \leq i \leq 38^\circ$ |
| IIa | Main Belt | $2.50 < a \leq 2.706, i < 33^\circ$ |
| IIb | Main Belt | $2.706 < a \leq 2.82, i < 33^\circ$ |
| KOR | Koronis Zone | $2.83 < a \leq 2.91, e \leq 0.11, i \leq 3.5^\circ$ |
| EOS | Eos Zone | $2.99 \leq a \leq 3.03, 0.01 \leq e \leq 0.13, 8^\circ \leq i \leq 12^\circ$ |
| IIIa | Main Belt | $2.82 < a \leq 3.03, e \leq 0.35, i \leq 30^\circ$ |
| THE | Themis Zone | $3.08 \leq a \leq 3.24, 0.09 \leq e \leq 0.22, i \leq 3^\circ$ |
| GR | Griqua Group | $3.10 \leq a \leq 3.27, e \geq 0.35$ |
| IIIb | Main Belt | $3.03 < a \leq 3.27, e < 0.35, i \leq 30^\circ$ |
| CYB | Cybele Group | $3.27 < a \leq 3.70, e \leq 0.30, i \leq 25^\circ$ |
| HIL | Hilda Group | $3.70 < a \leq 4.20, e \leq 0.30, i \leq 20^\circ$ |
| T | Trojan Group | $5.05 \leq a \leq 5.40$ |

drawn from Zellner (1979) as augmented and altered by Gradie et al. (1989), and with the addition of a zone for the Vesta family of asteroids, which were targeted heavily by Xu et al. (1995), and the separation of the Amor-Aten-Apollo zone into its three component regions.

Figures 6.3 – 6.10 display the taxonomic probabilities for each of the 22 regions listed in Table 6.2. Taxonomic classifications for 1295 objects have been collected from the literature and produced for those objects observed in this

survey. The catalog of taxonomic classifications and selected other parameters are available from the author.

After the derivation of $P_{det,total}$ and $P_{tax,total}$, *correction factors* may be derived for every object such that any one taxonomically classified object corresponds to the true number of objects which exist in that taxonomic class, at that absolute magnitude, and in that orbital element zone. These correction factors are simply the reciprocals of $P_{det,total}$ and $P_{tax,total}$. A list of these corrections factors for 1295 taxonomically classified objects is available from the author by request. Systematic errors were estimated by varying the numbers of search exposures by factors of two, and recomputing the correction factors accordingly.

Once the true distribution of objects versus magnitude is known, it is then possible to derive the true size distribution. The absolute magnitude H of an object is dependent on its geometric albedo p and its diameter D through the following relation (Muinonen et al. 1995):

$$H(D, p) = 15.648 - 5 \log D - 2.5 \log p. \quad (6.9)$$

The results of these debiasing efforts are presented in Chapter 7.

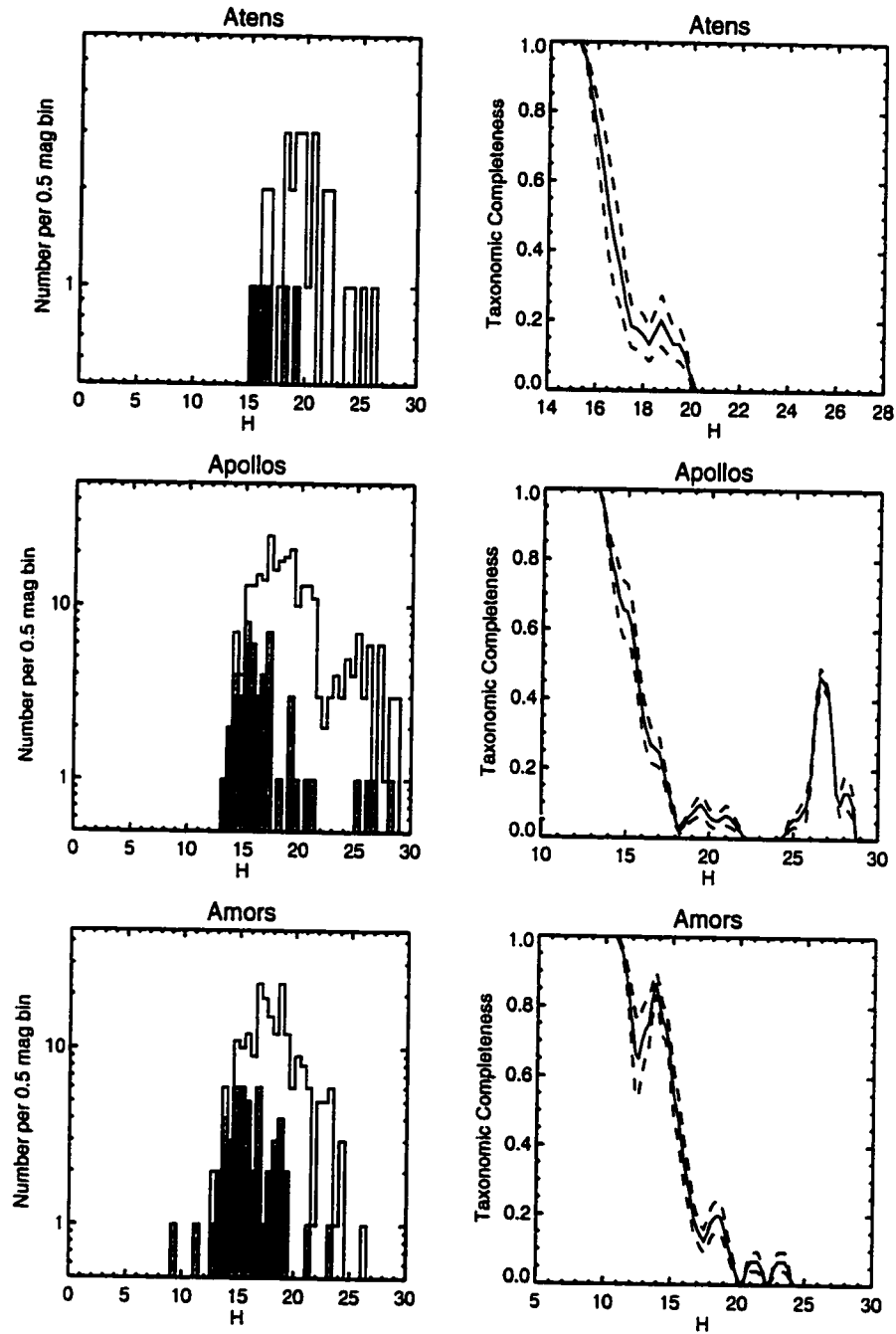


Figure 6.3: Taxonomic completenesses for the Atens, Apollos, and Amors. Figures on the left display histograms of the numbers of detected objects versus absolute magnitude H ; the shaded areas represent those objects which have been taxonomically classified. Figures on the right present the derived taxonomic completeness functions versus absolute magnitude. Dashed lines represent 1σ uncertainties.

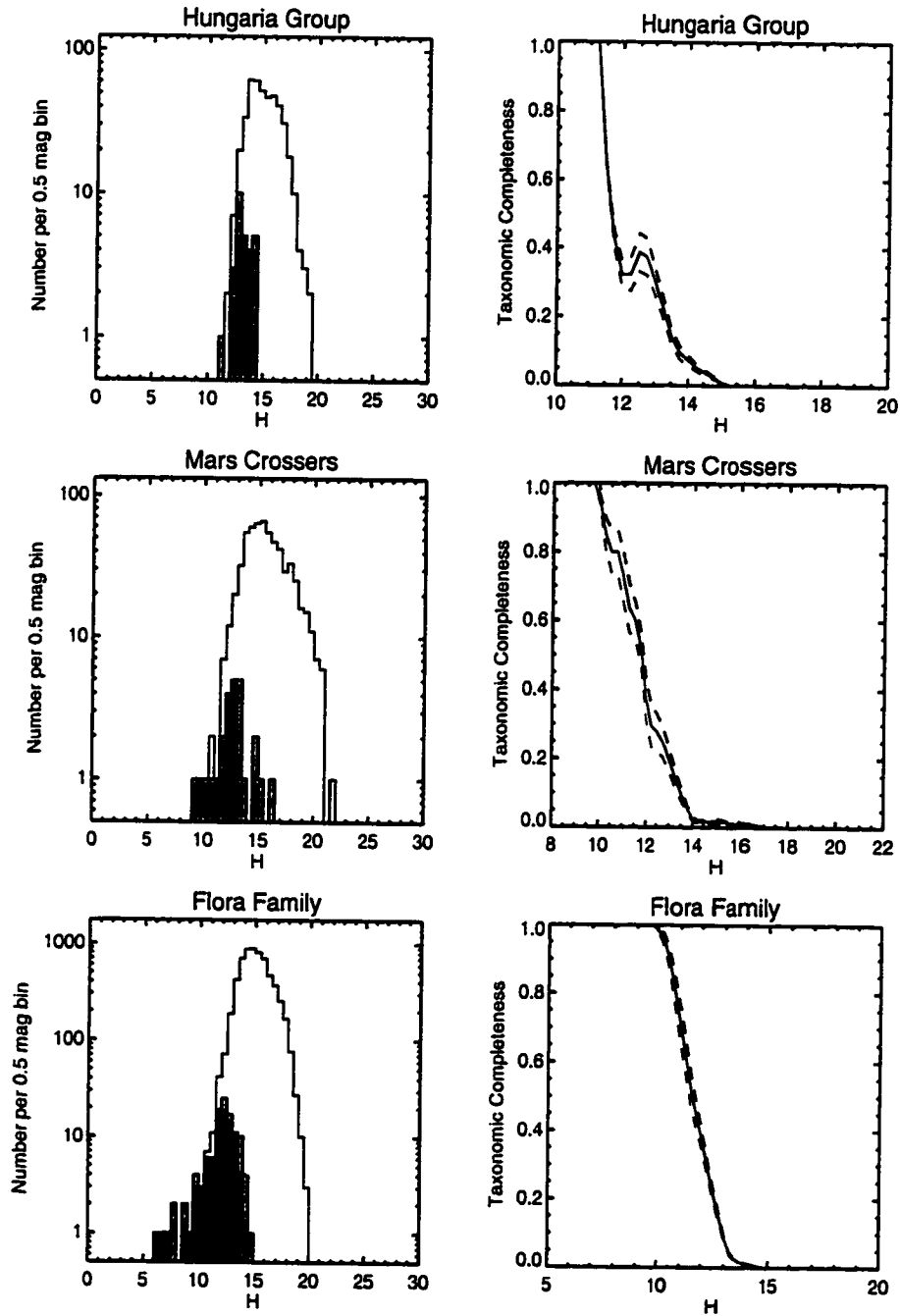


Figure 6.4: Taxonomic completenesses for the Hungaria Group, Mars Crossers, and Flora Family. Figures on the left display histograms of the numbers of detected objects versus absolute magnitude H ; the shaded areas represent those objects which have been taxonomically classified. Figures on the right present the derived taxonomic completeness functions versus absolute magnitude. Dashed lines represent 1σ uncertainties.

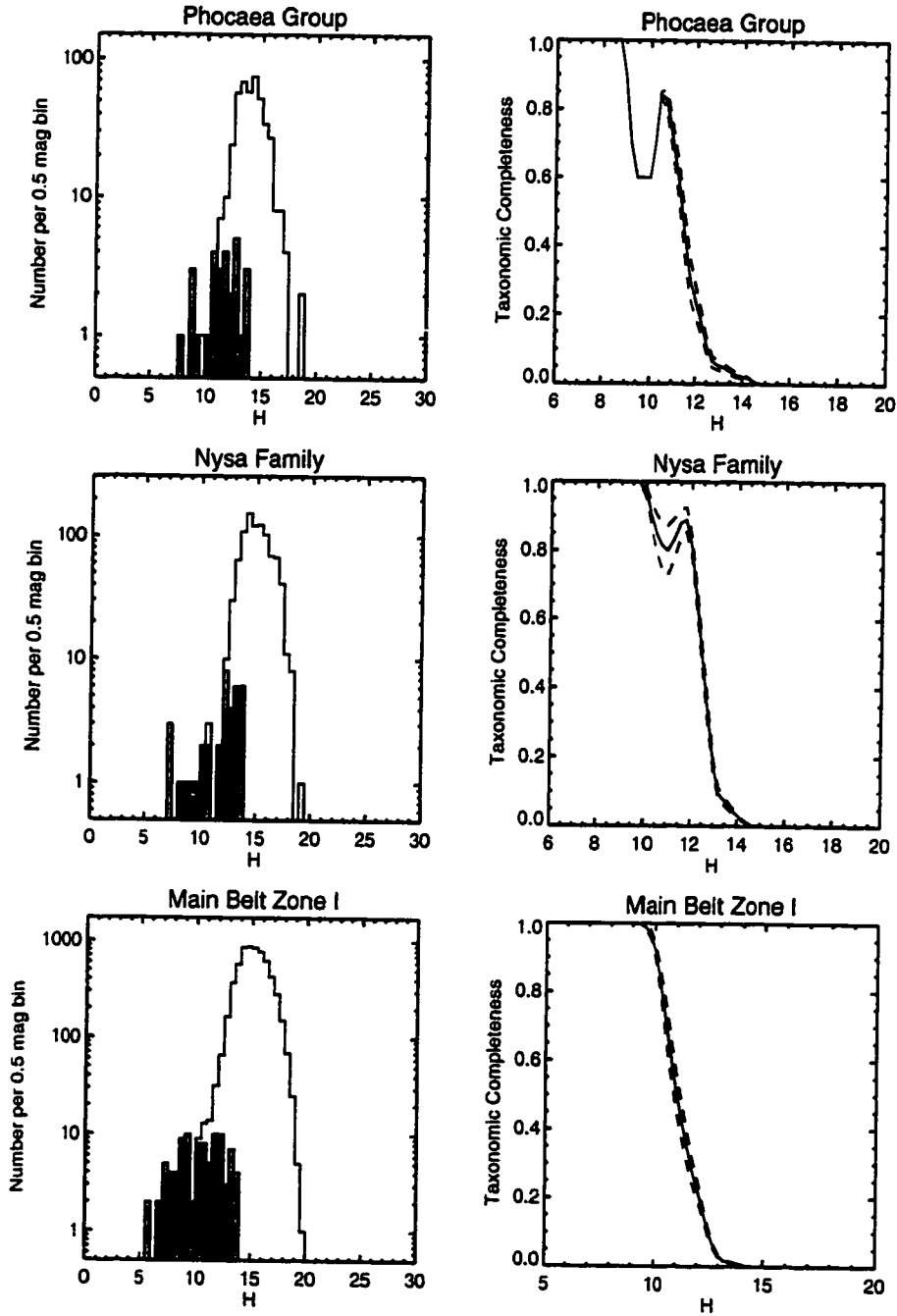


Figure 6.5: Taxonomic completenesses for the Phocaea Group, Nysa Family, and Main Belt I. Figures on the left display histograms of the numbers of detected objects versus absolute magnitude H ; the shaded areas represent those objects which have been taxonomically classified. Figures on the right present the derived taxonomic completeness functions versus absolute magnitude. Dashed lines represent 1σ uncertainties.

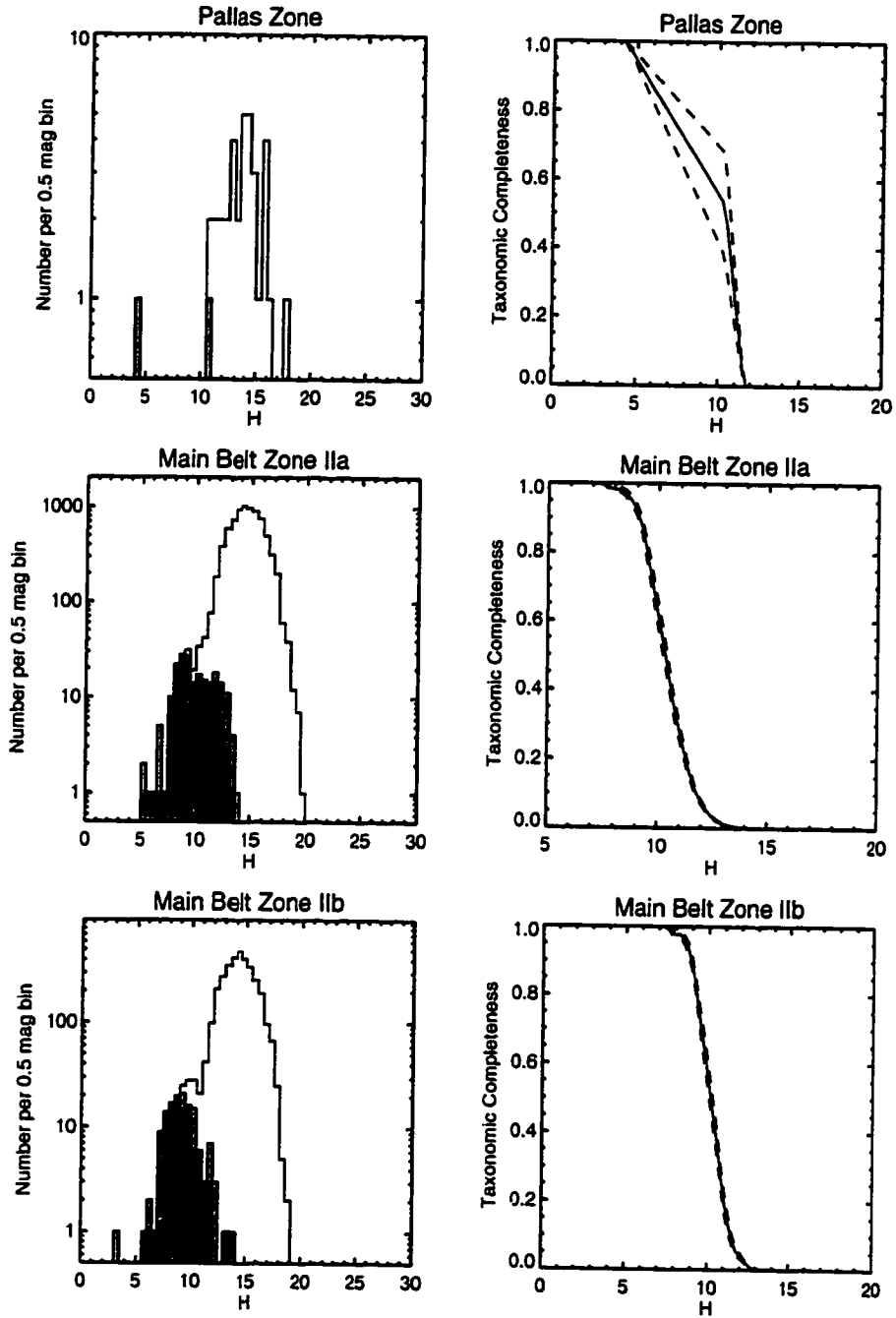


Figure 6.6: Taxonomic completenesses for the Pallas Zone, Main Belt IIa, and Main Belt IIb. Figures on the left display histograms of the numbers of detected objects versus absolute magnitude H ; the shaded areas represent those objects which have been taxonomically classified. Figures on the right present the derived taxonomic completeness functions versus absolute magnitude. Dashed lines represent 1σ uncertainties.

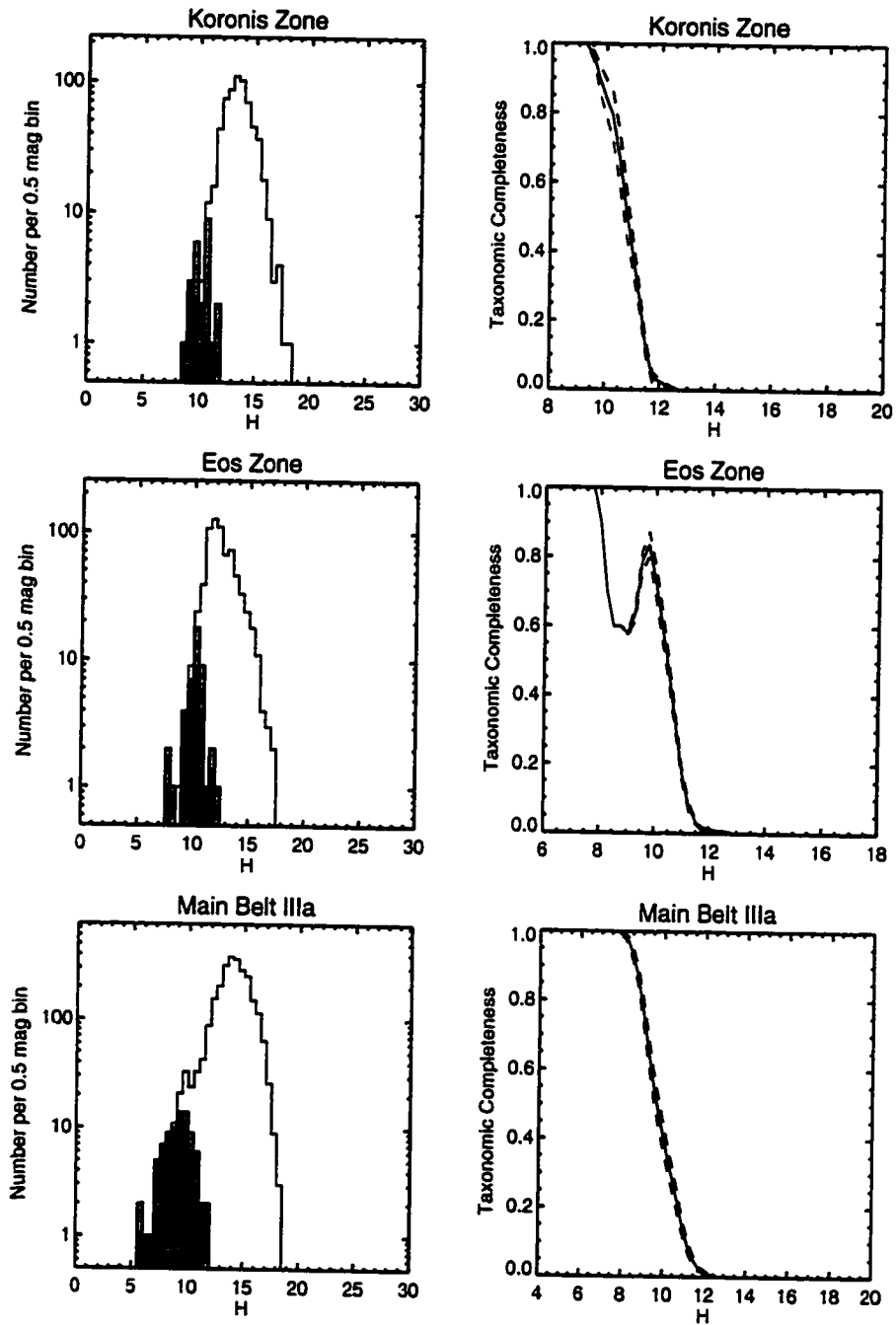


Figure 6.7: Taxonomic completenesses for the Koronis Zone, Eos Zone, and Main Belt IIIa. Figures on the left display histograms of the numbers of detected objects versus absolute magnitude H ; the shaded areas represent those objects which have been taxonomically classified. Figures on the right present the derived taxonomic completeness functions versus absolute magnitude. Dashed lines represent 1σ uncertainties.

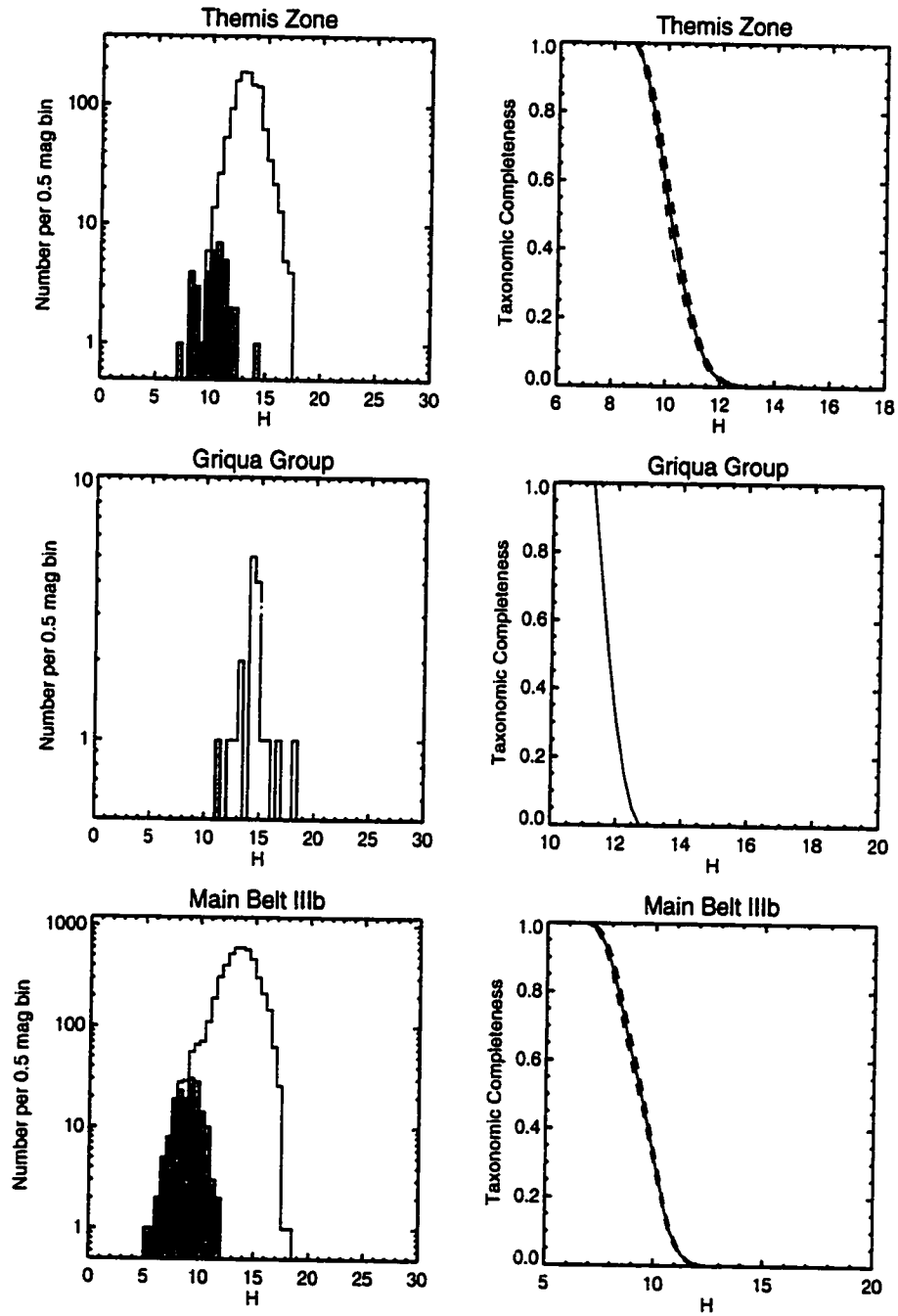


Figure 6.8: Taxonomic completenesses for the Themis Zone, Griqua Group, and Main Belt IIIb. Figures on the left display histograms of the numbers of detected objects versus absolute magnitude H ; the shaded areas represent those objects which have been taxonomically classified. Figures on the right present the derived taxonomic completeness functions versus absolute magnitude. Dashed lines represent 1σ uncertainties.

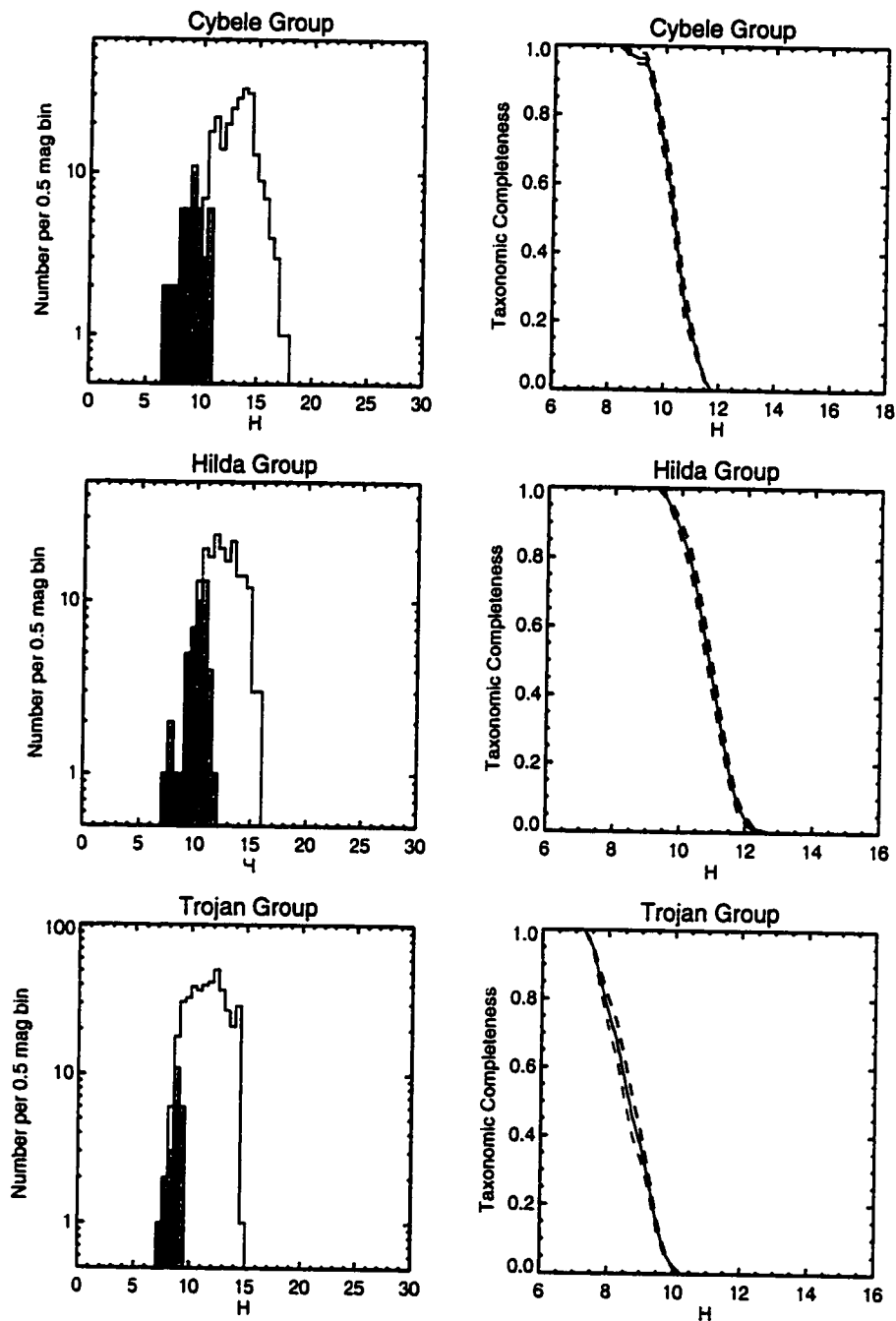


Figure 6.9: Taxonomic completenesses for the Cybele Group, Hilda Group, and Trojan Group. Figures on the left display histograms of the numbers of detected objects versus absolute magnitude H ; the shaded areas represent those objects which have been taxonomically classified. Figures on the right present the derived taxonomic completeness functions versus absolute magnitude. Dashed lines represent 1σ uncertainties.

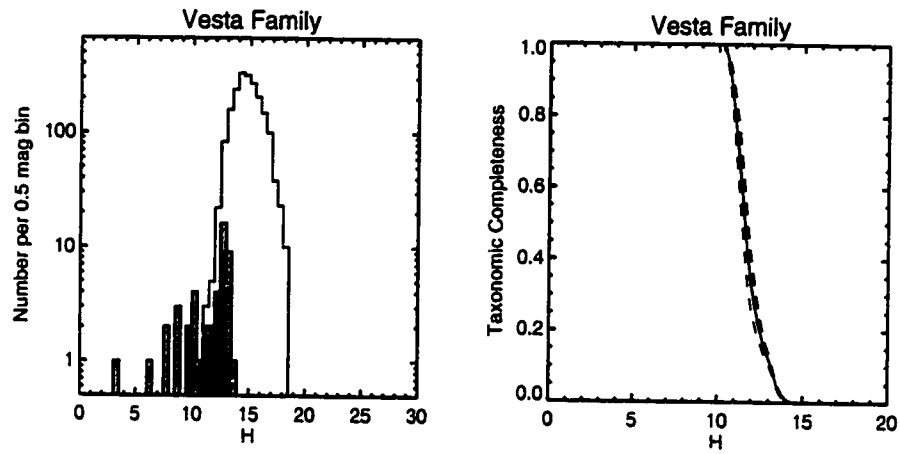


Figure 6.10: Taxonomic completenesses for the Vesta Family. The figure on the left displays a histogram of the numbers of detected objects versus absolute magnitude H ; the shaded areas represent those objects which have been taxonomically classified. The figure on the right presents the derived taxonomic completeness function versus absolute magnitude. Dashed lines represent 1σ uncertainties.

Chapter 7

Discussion of Debiasing Results

*I wish I were a little rock,
A-sitting on a hill,
A-doing nothing all day long,
But just a sitting still;
I wouldn't eat, I wouldn't sleep,
I wouldn't even wash -
I'd sit and sit a thousand years,
And rest myself, b'Gosh!*

— Frederick Palmer Latimer

Figures 7.1 – 7.22 present the bias-corrected cumulative size distributions of objects in each of 22 orbital element zones. Slopes for three different size exponents are overplotted; this is the exponent b in the traditional expression

$$N(> D) = AD^{-b+1}. \quad (7.1)$$

An exponent $b = 3.5$ corresponds to the expected value for a collisionally evolved system (Dohnanyi 1971).

Figure 7.23 displays the bias-corrected cumulative size distributions for the combined NEO population (i.e., the Amors, Atens, and Apollos).

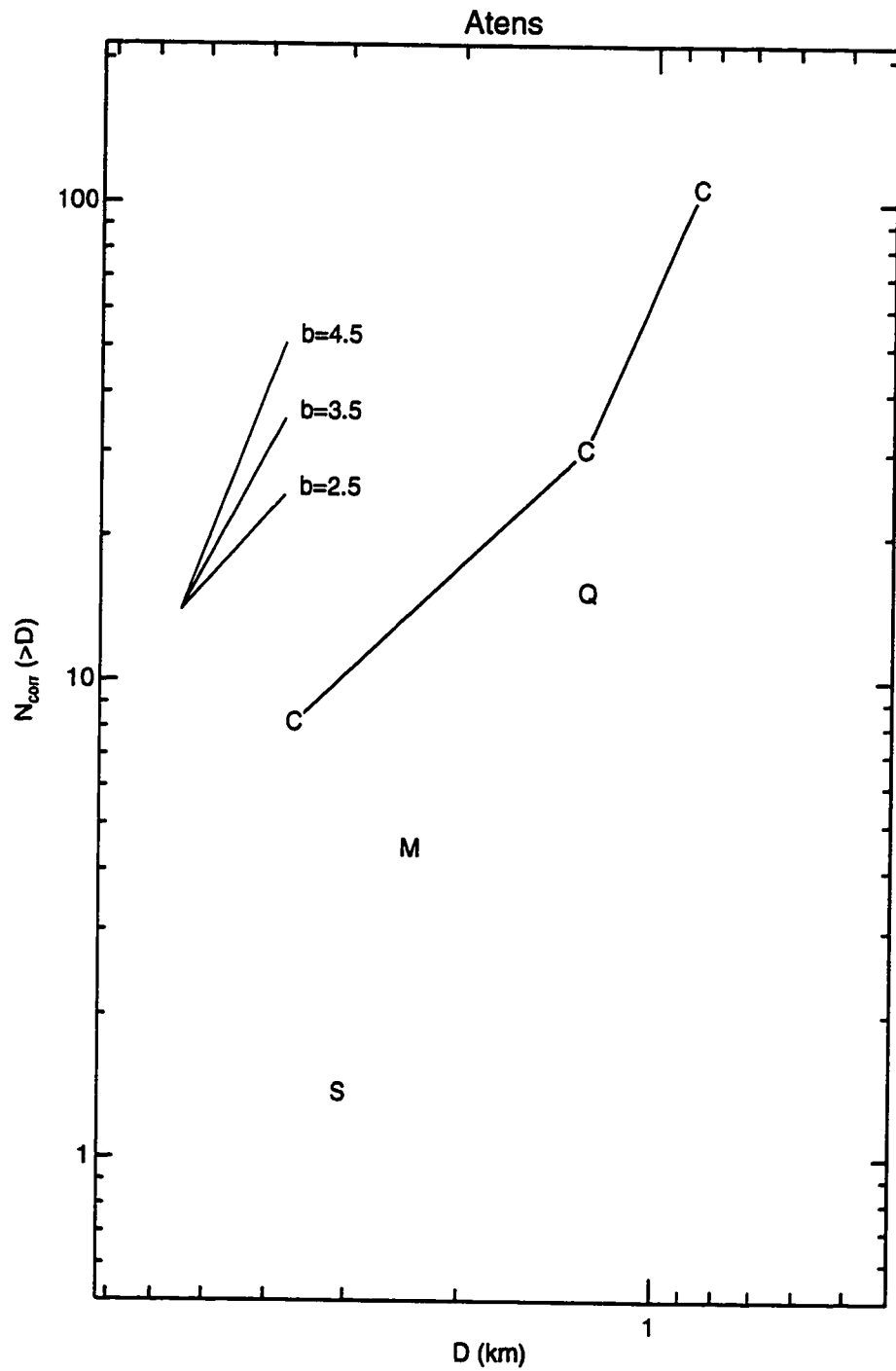


Figure 7.1: Cumulative Size-Frequency Diagram for the Atens.

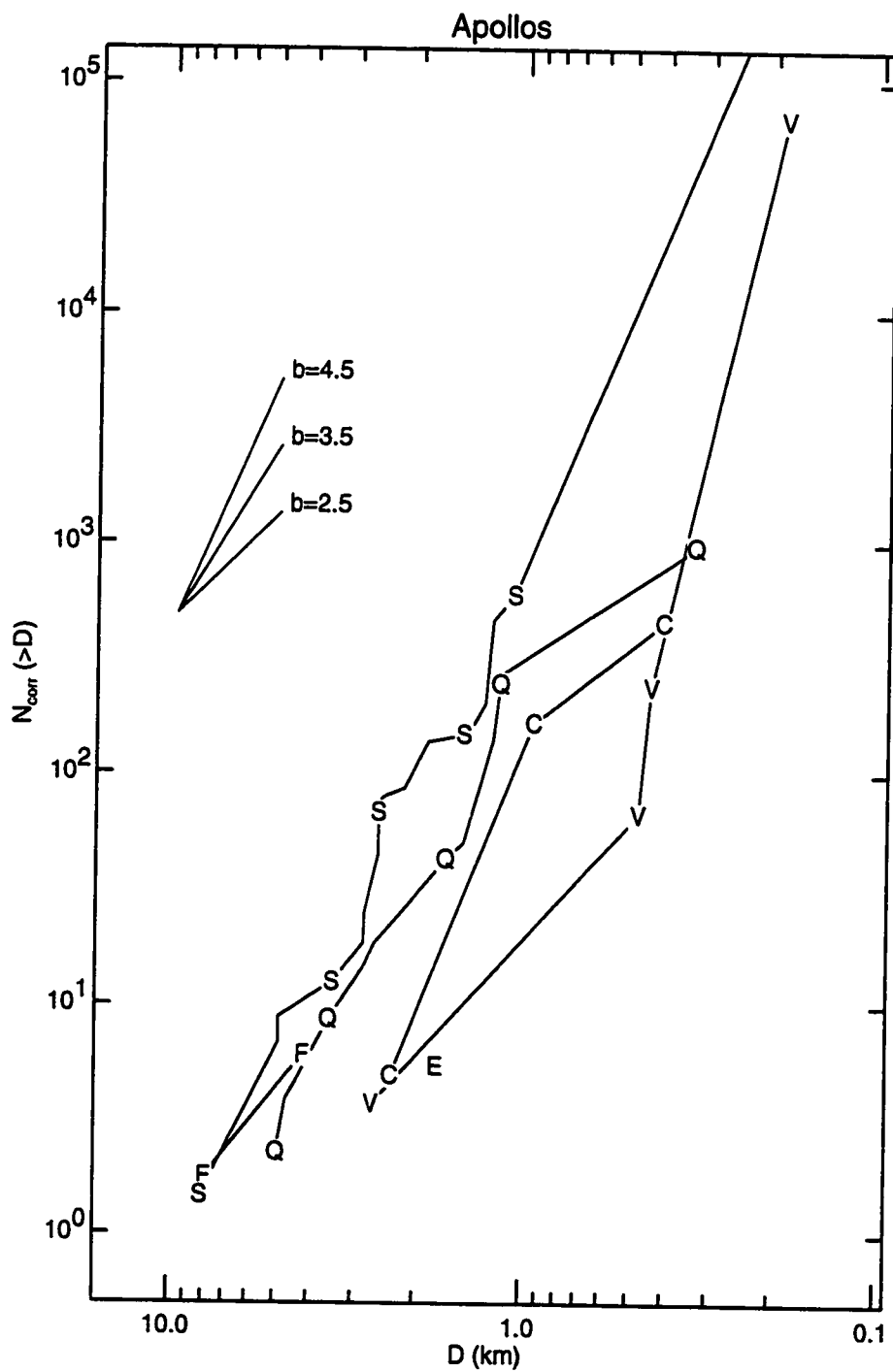


Figure 7.2: Cumulative Size-Frequency Diagram for the Apollos.

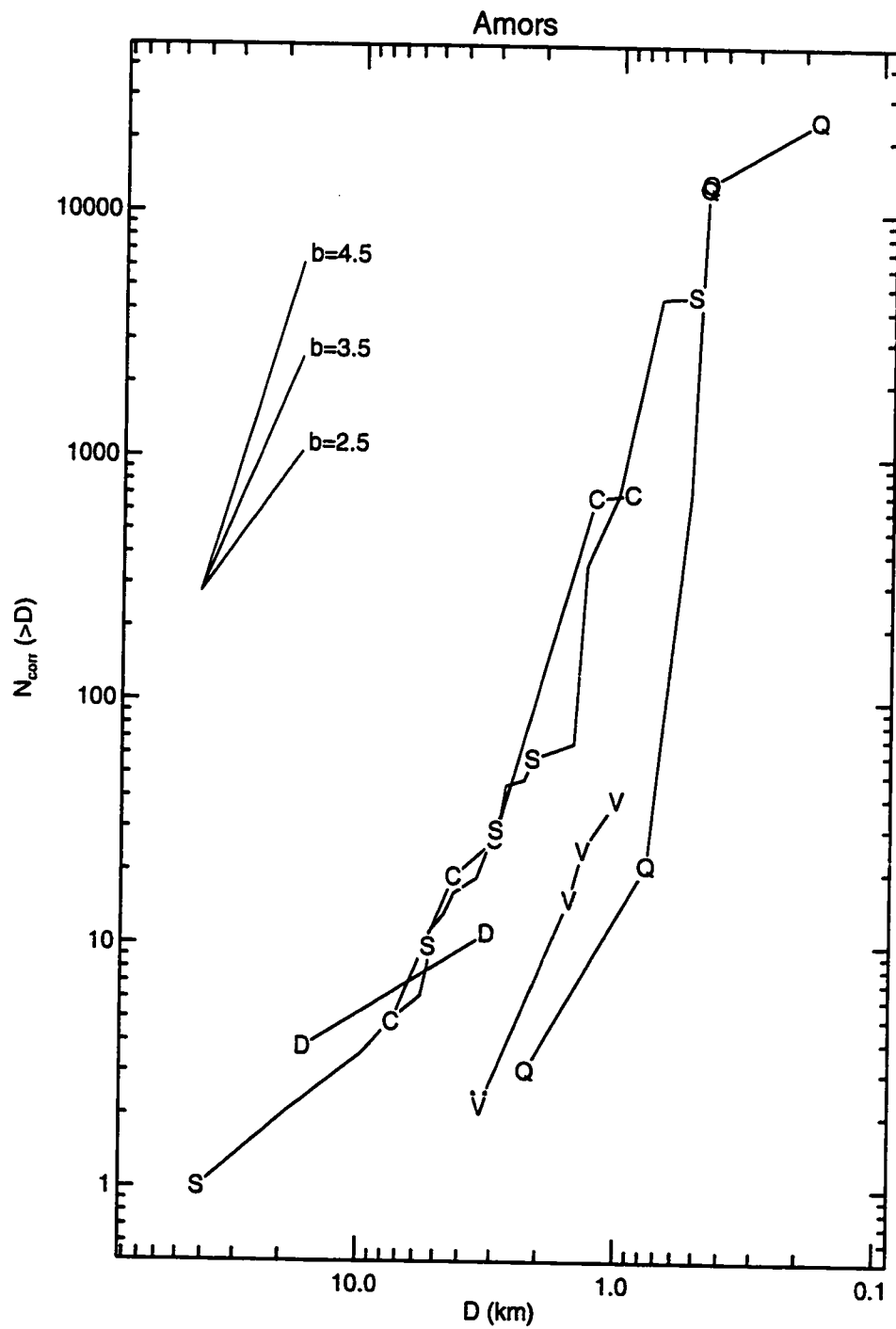


Figure 7.3: Cumulative Size-Frequency Diagram for the Amors.

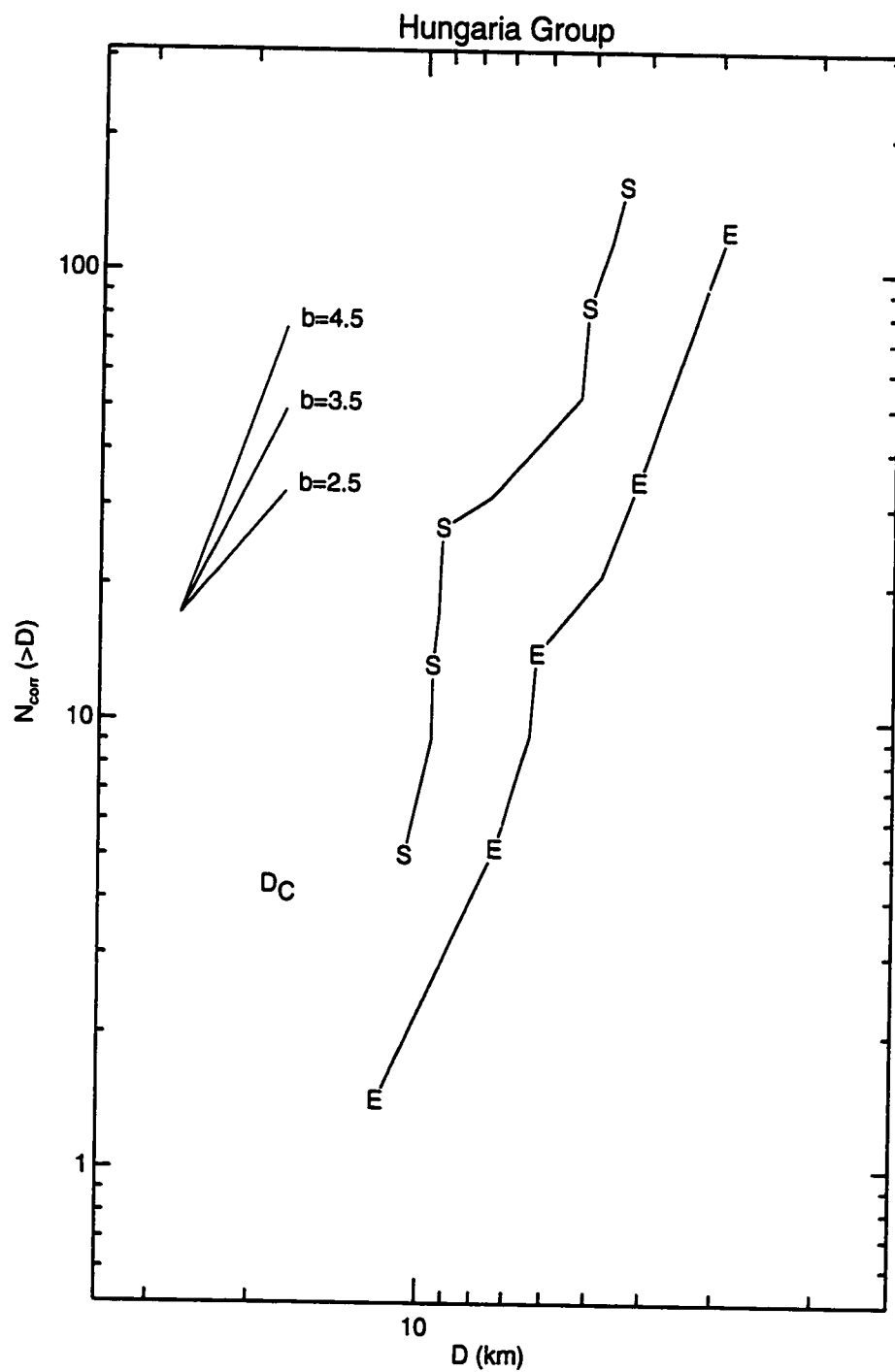


Figure 7.4: Cumulative Size-Frequency Diagram for the Hungaria Group.

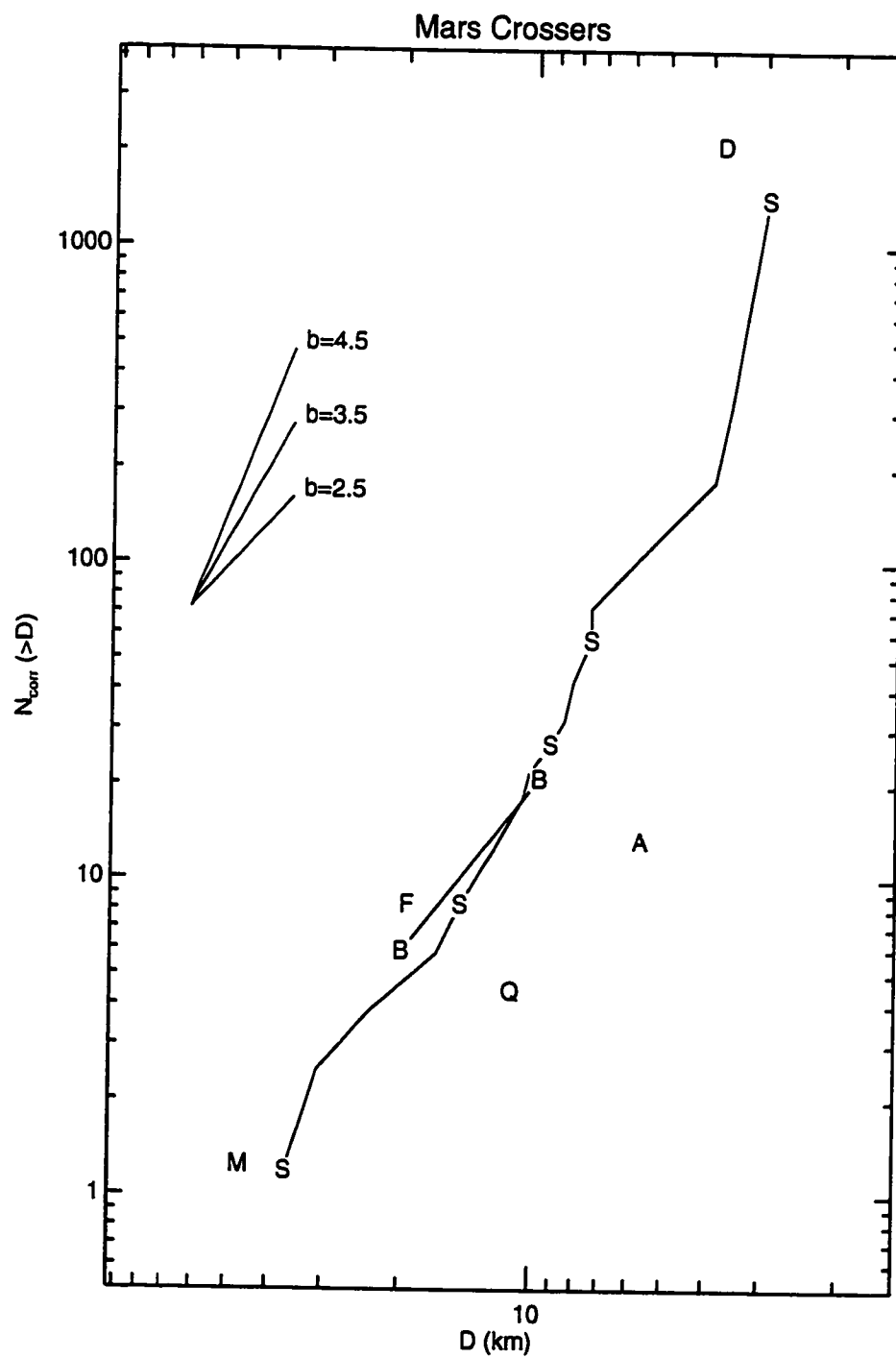


Figure 7.5: Cumulative Size-Frequency Diagram for the Mars Crossers.

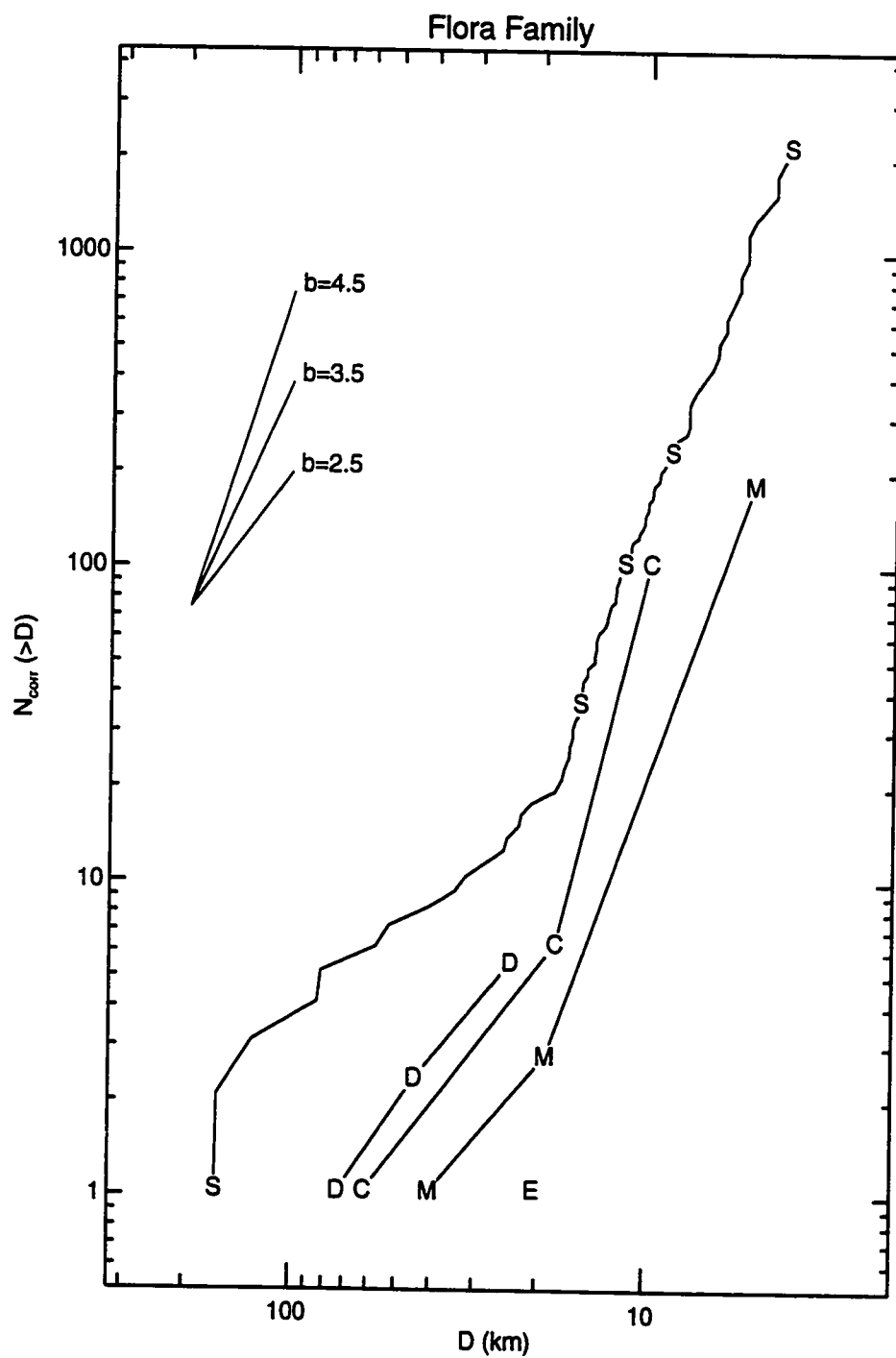


Figure 7.6: Cumulative Size-Frequency Diagram for the Flora Family.

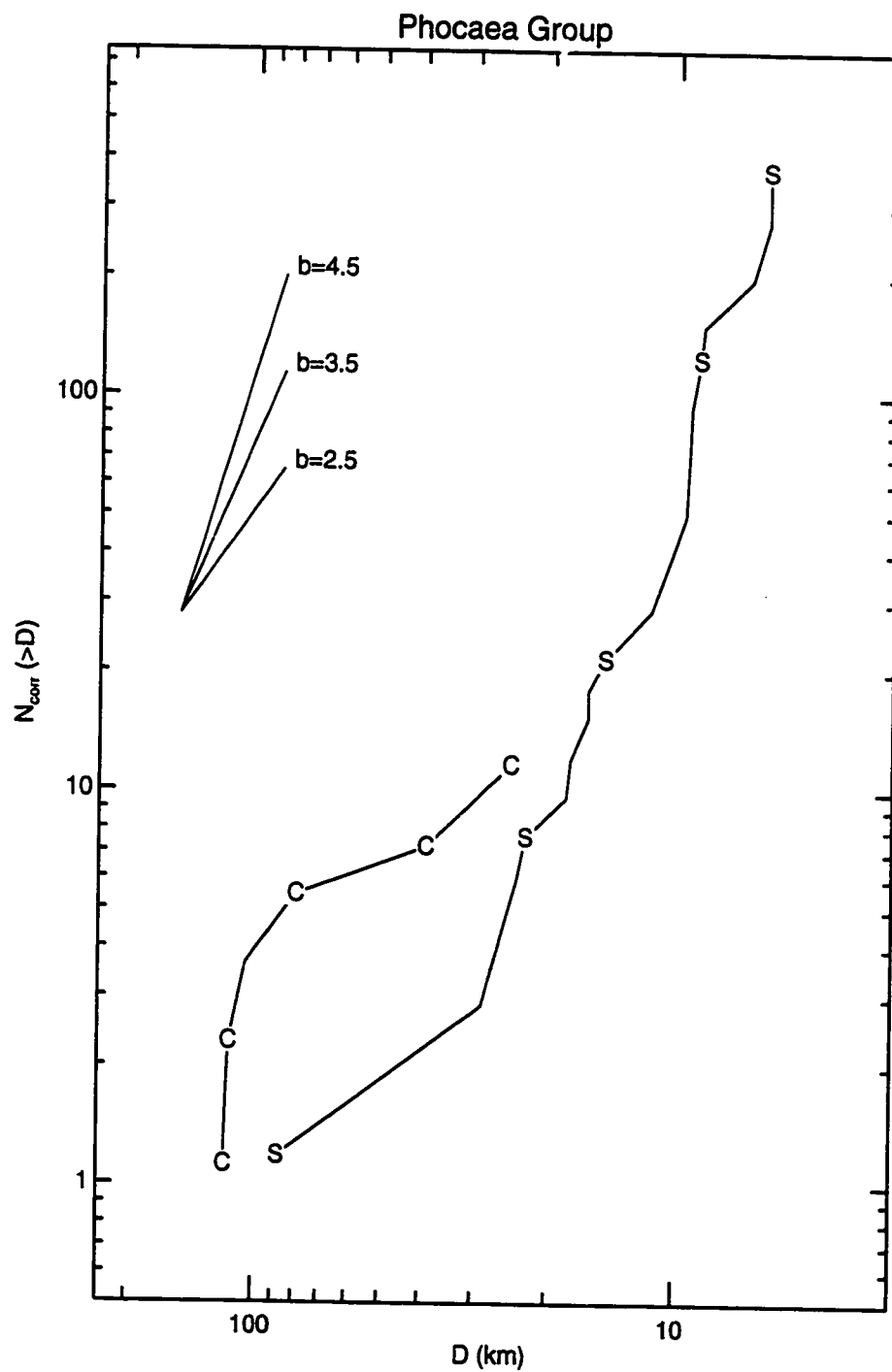


Figure 7.7: Cumulative Size-Frequency Diagram for the Phocaea Group.

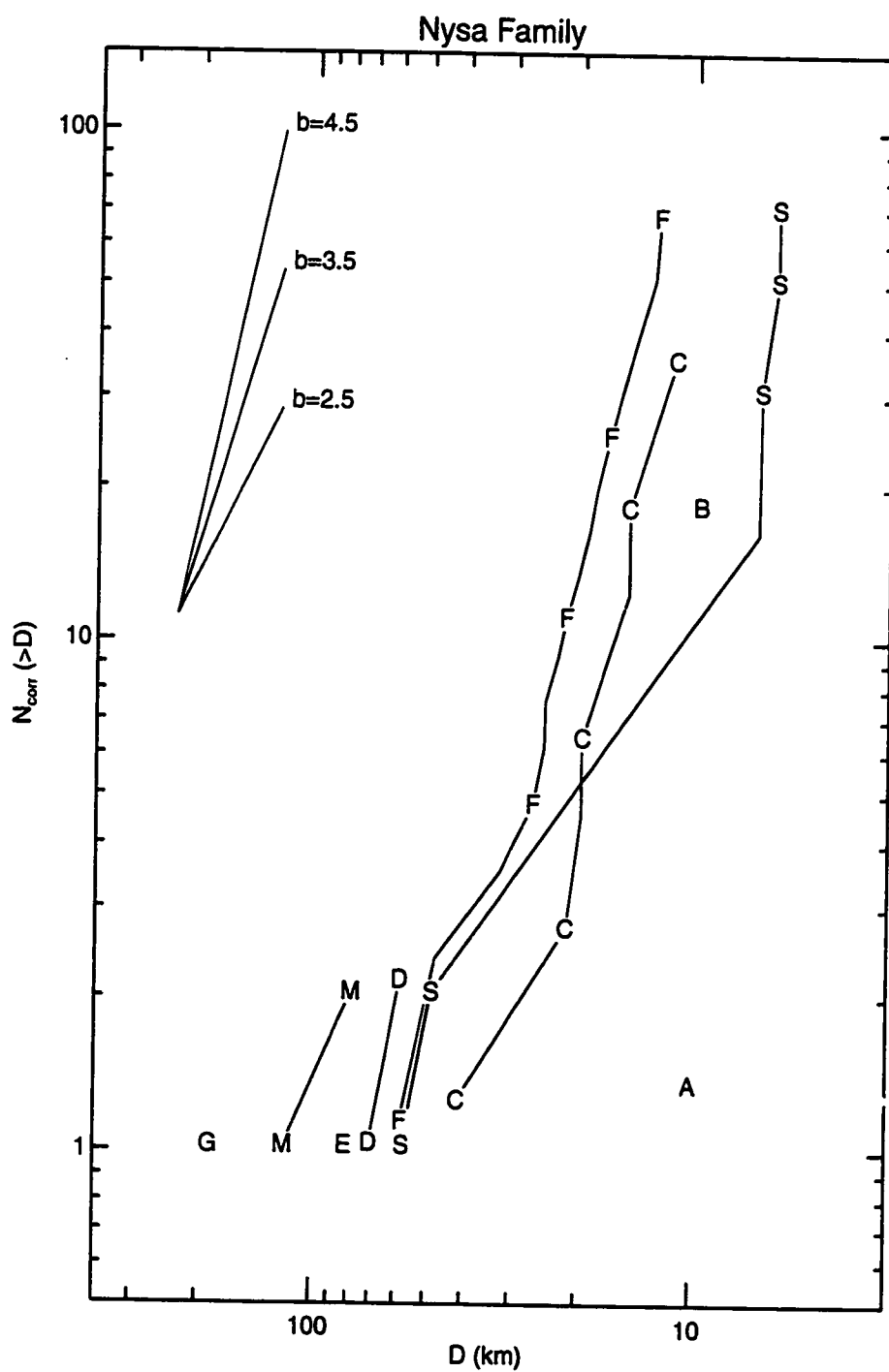


Figure 7.8: Cumulative Size-Frequency Diagram for the Nysa Family.

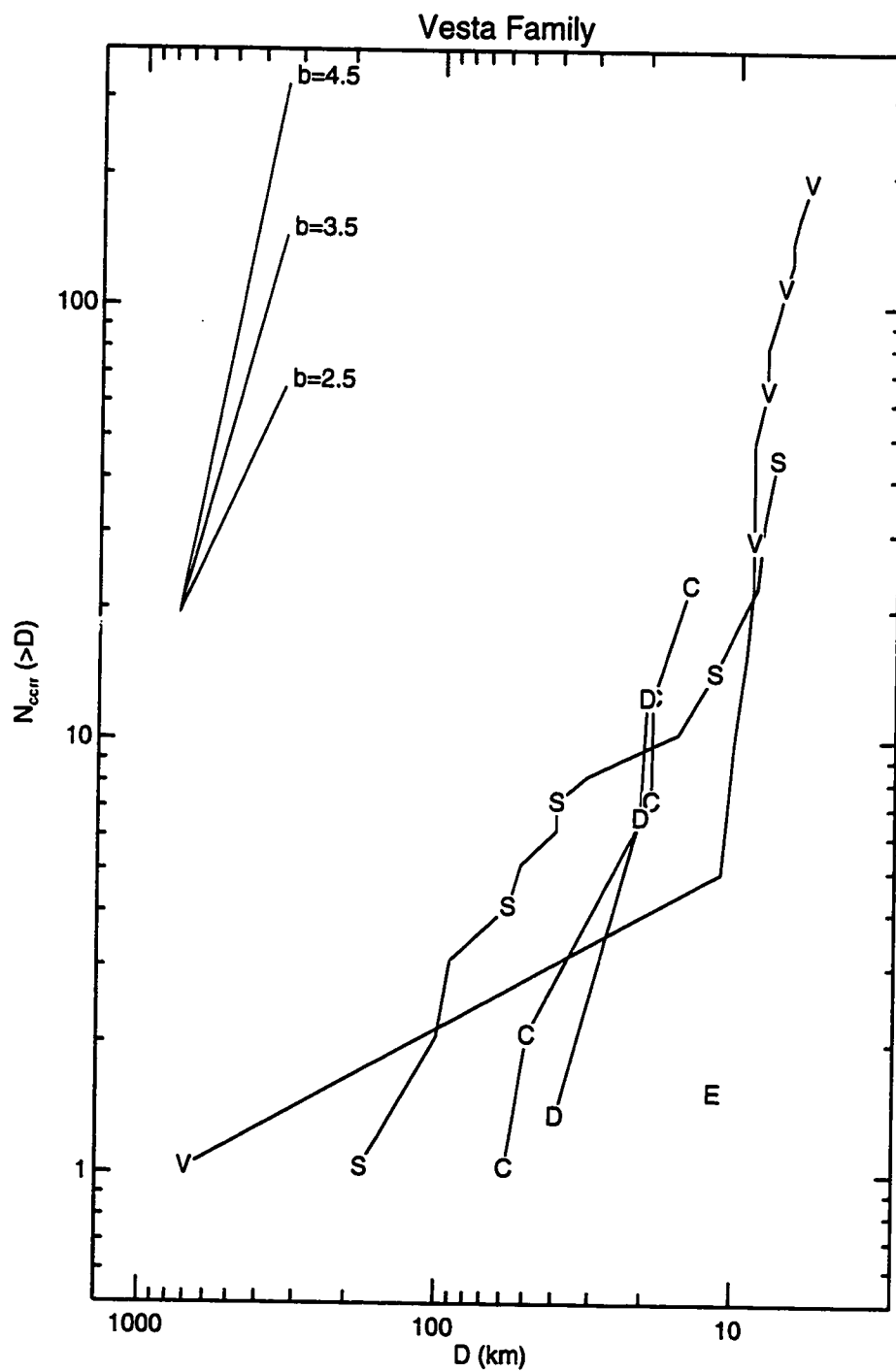


Figure 7.9: Cumulative Size-Frequency Diagram for the Vesta Family.

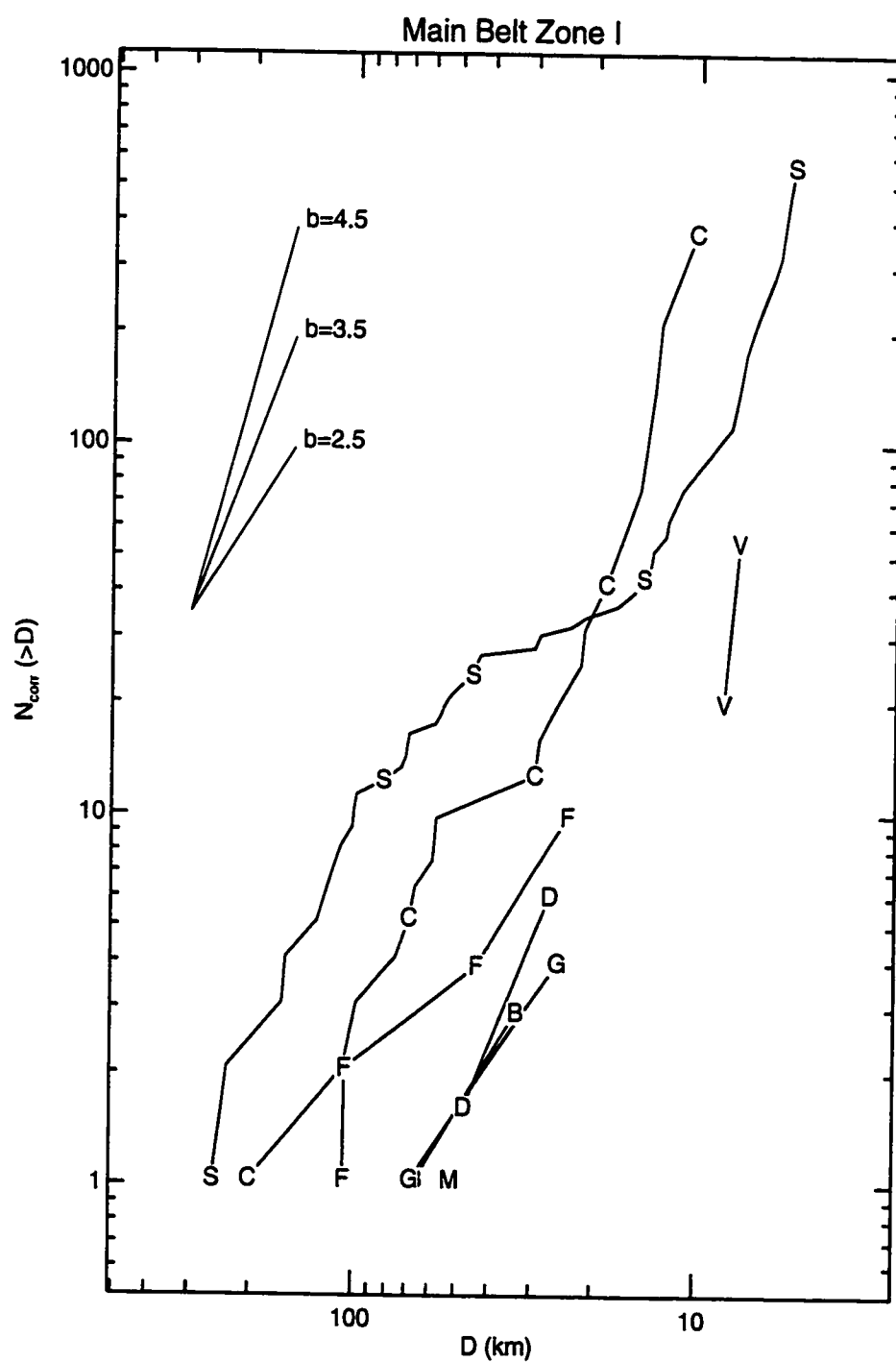


Figure 7.10: Cumulative Size-Frequency Diagram for Main Belt Zone I.

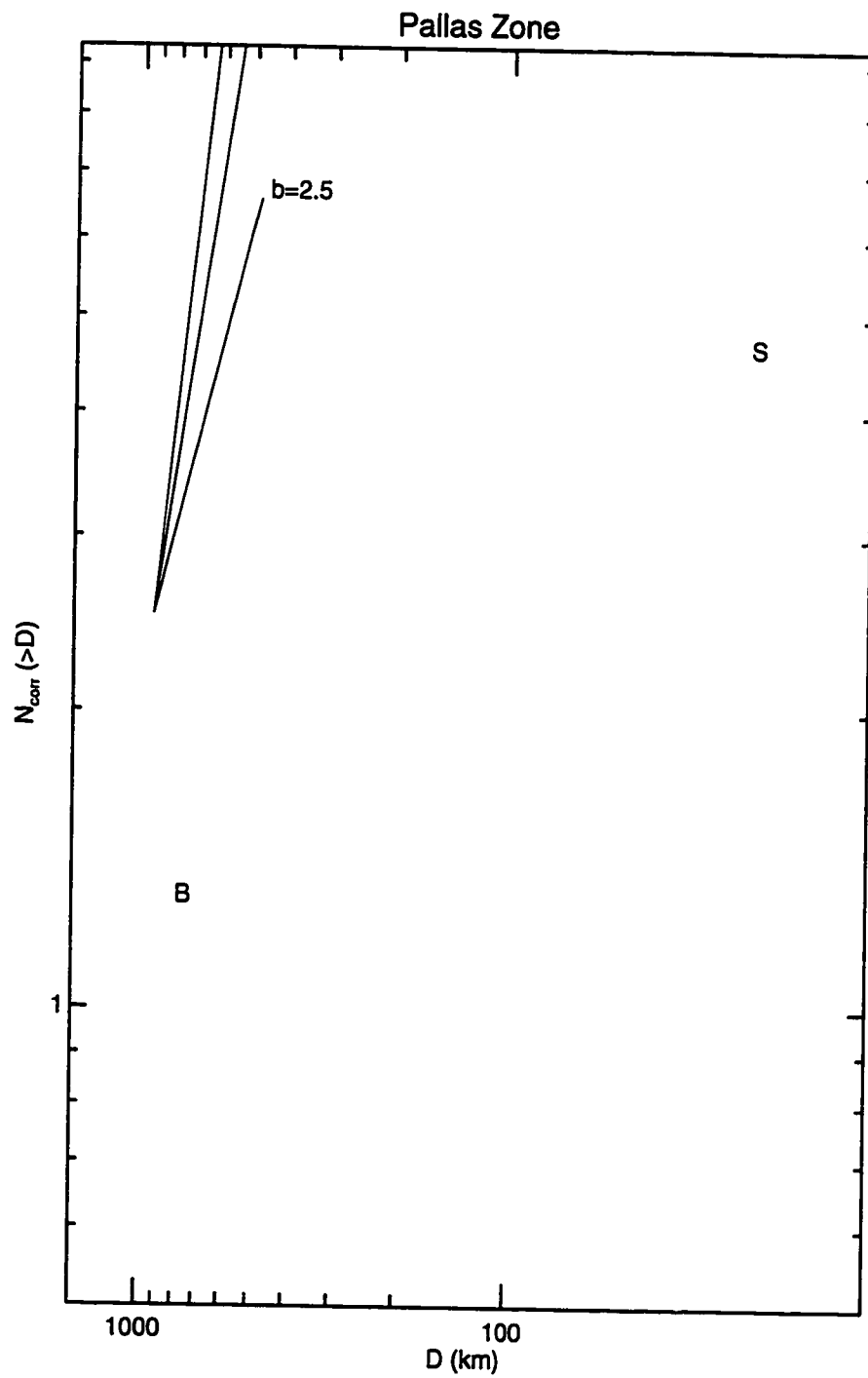


Figure 7.11: Cumulative Size-Frequency Diagram for the Pallas Zone.

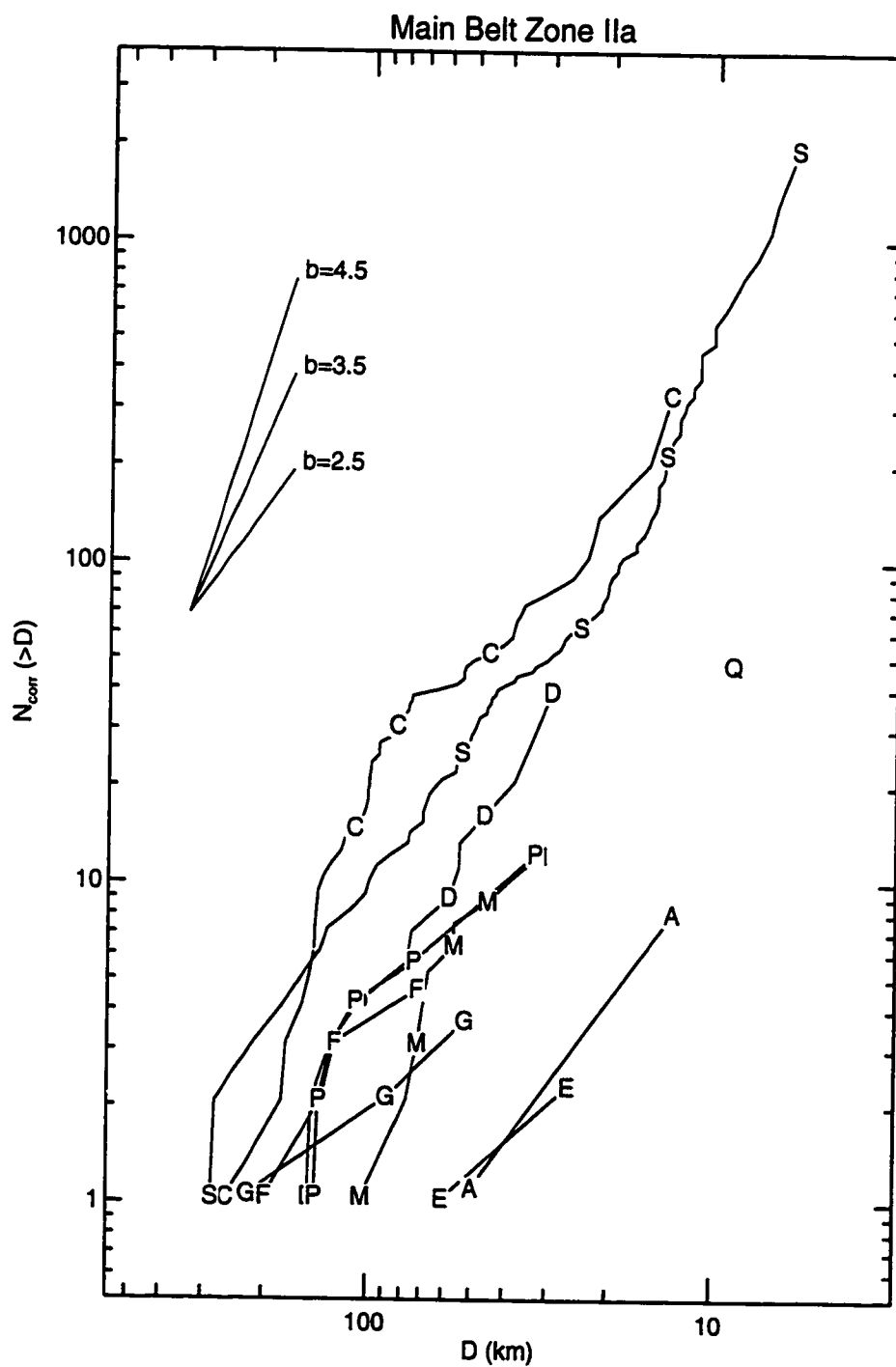


Figure 7.12: Cumulative Size-Frequency Diagram for Main Belt Zone IIa.

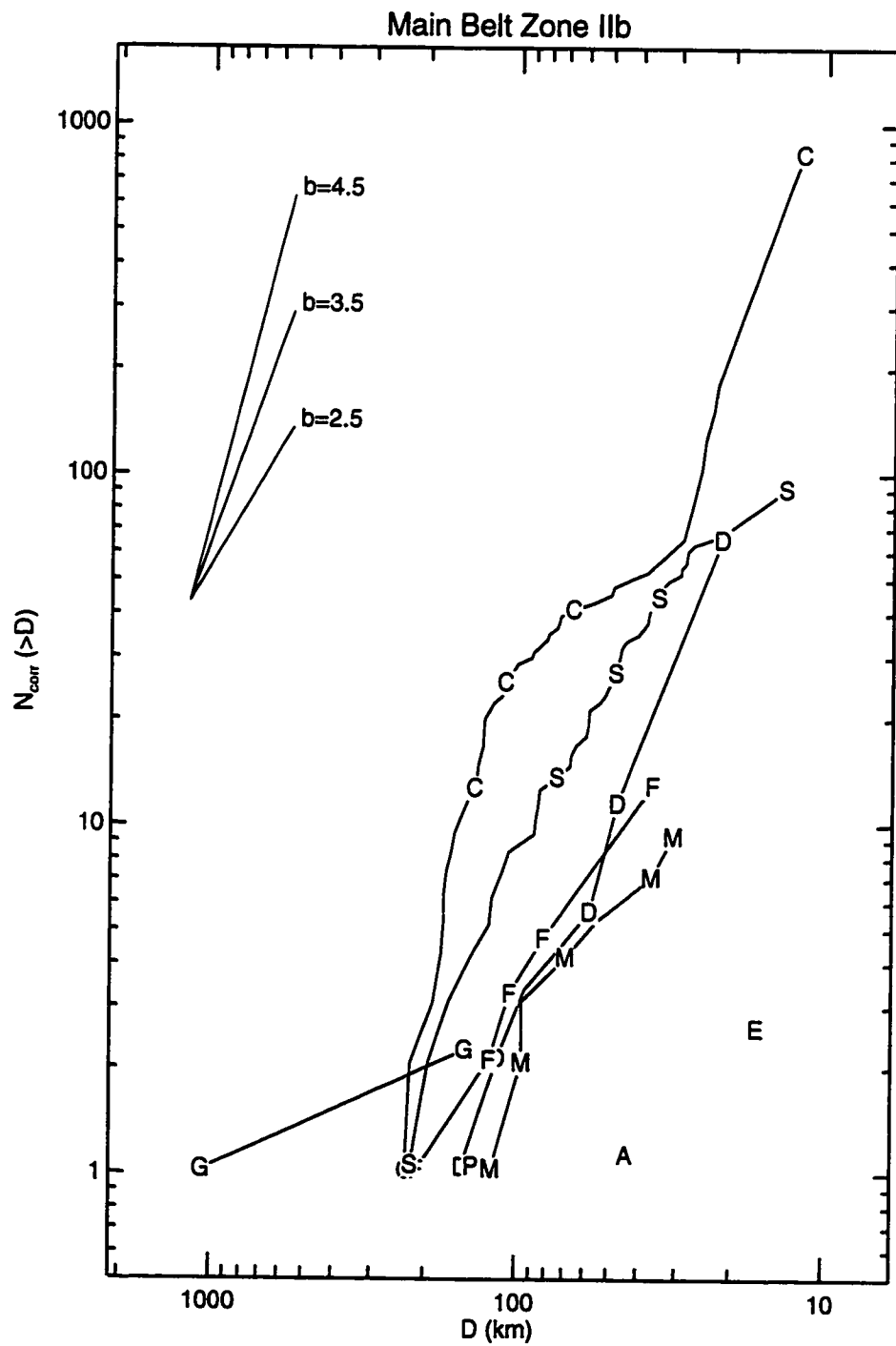


Figure 7.13: Cumulative Size-Frequency Diagram for Main Belt Zone IIb.

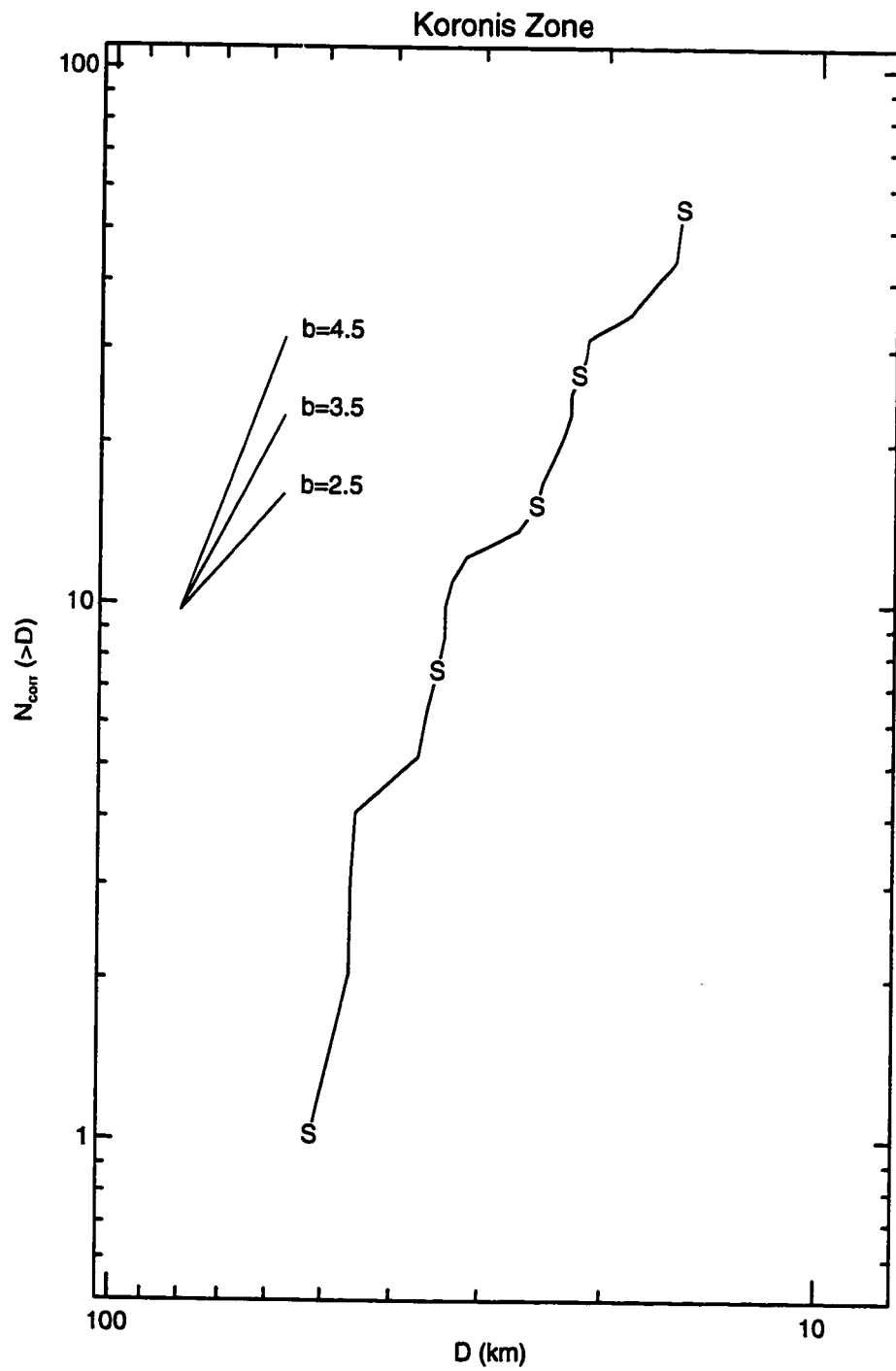


Figure 7.14: Cumulative Size-Frequency Diagram for the Koronis Zone.

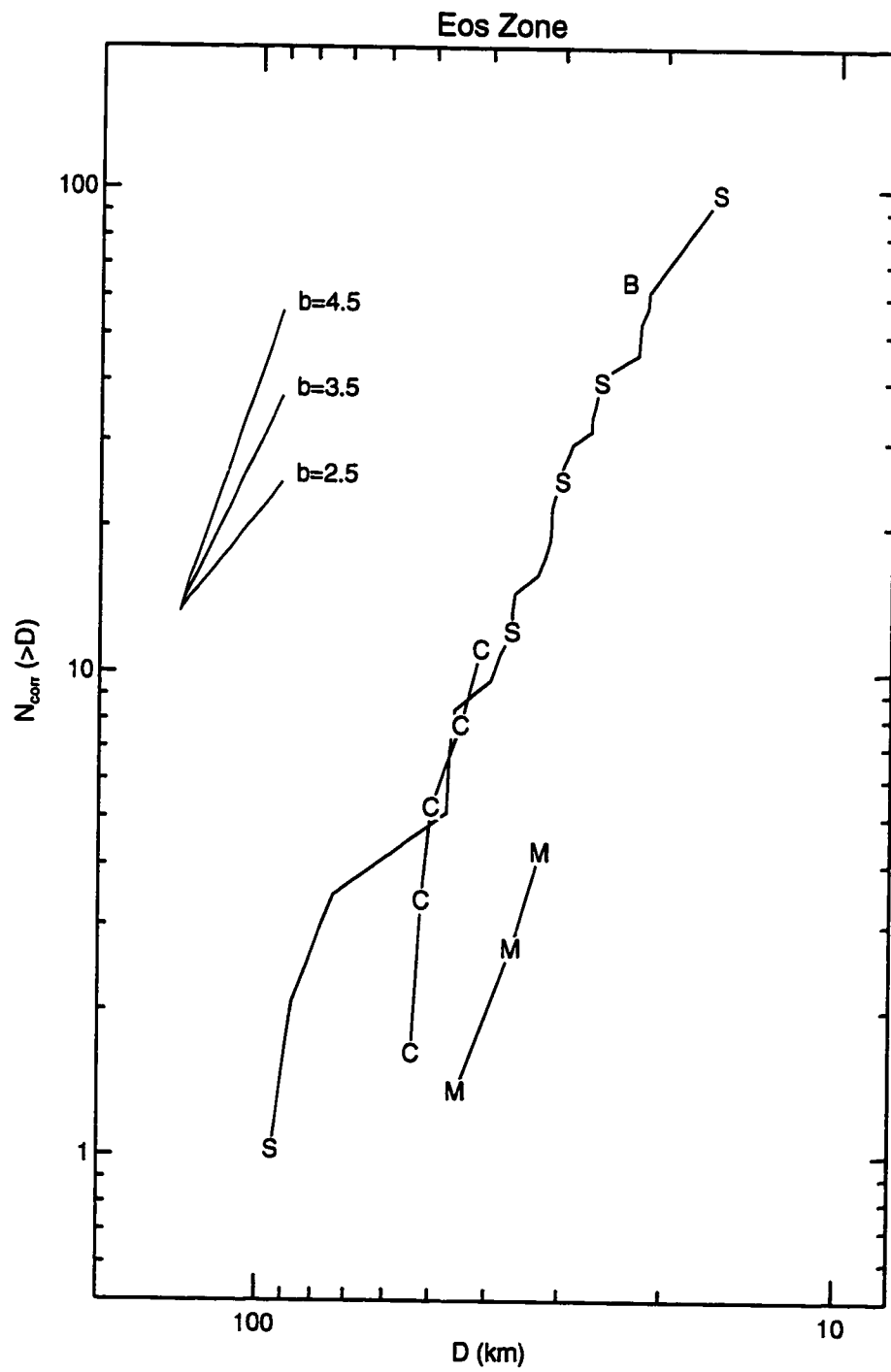


Figure 7.15: Cumulative Size-Frequency Diagram for the Eos Zone.

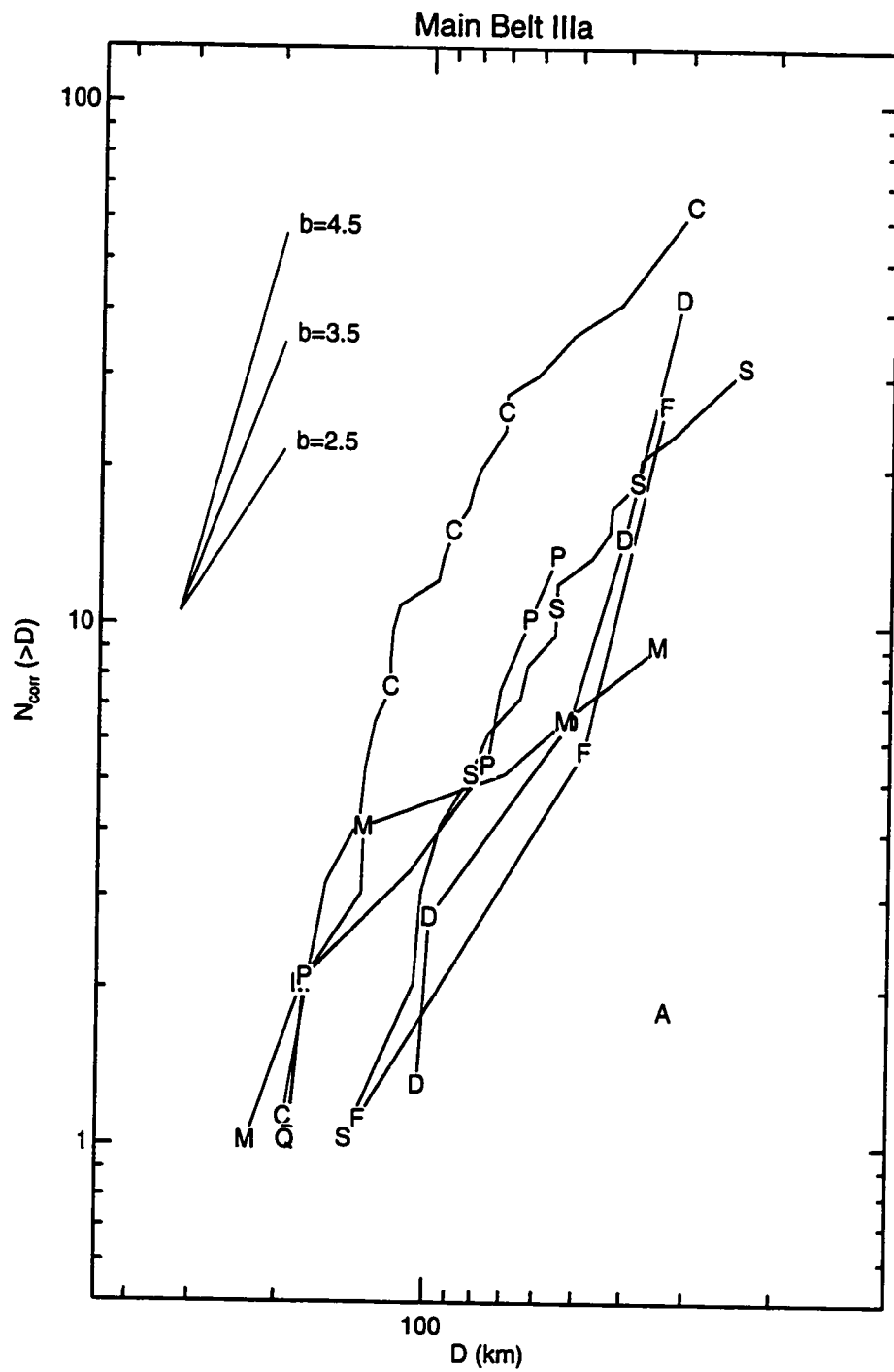


Figure 7.16: Cumulative Size-Frequency Diagram for Main Belt Zone IIIa.

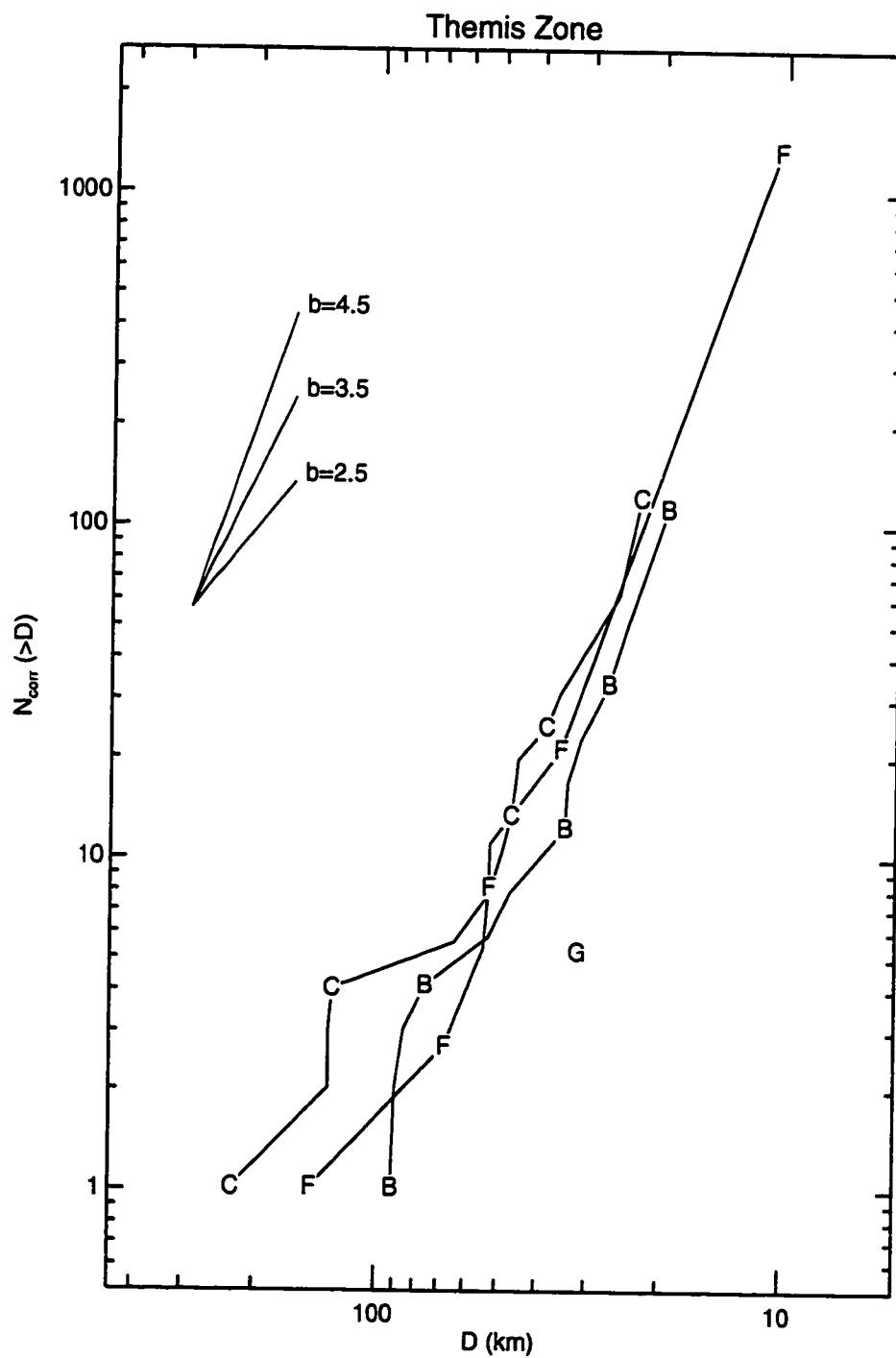


Figure 7.17: Cumulative Size-Frequency Diagram for the Themis Zone.

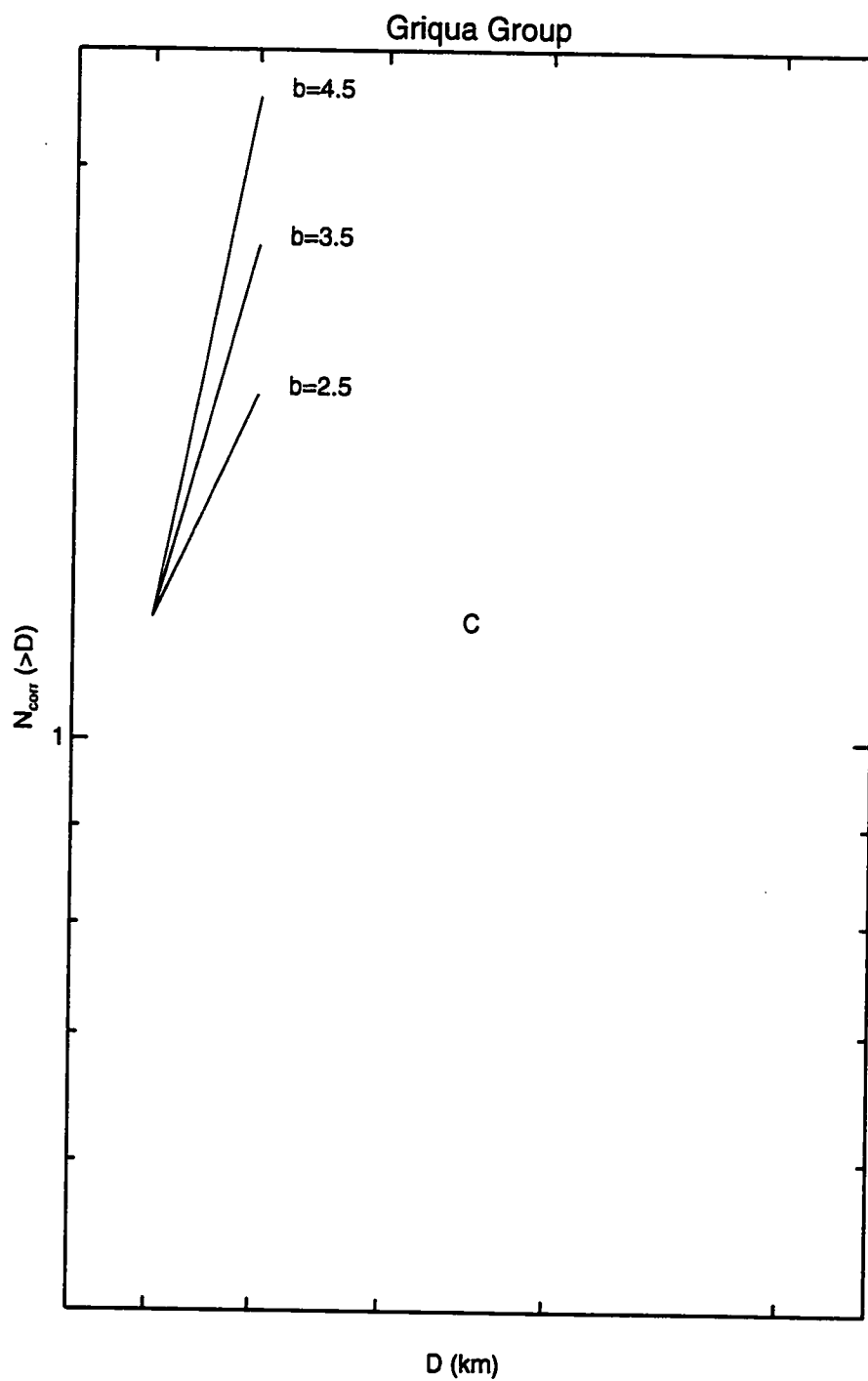


Figure 7.18: Cumulative Size-Frequency Diagram for the Griqua Group.

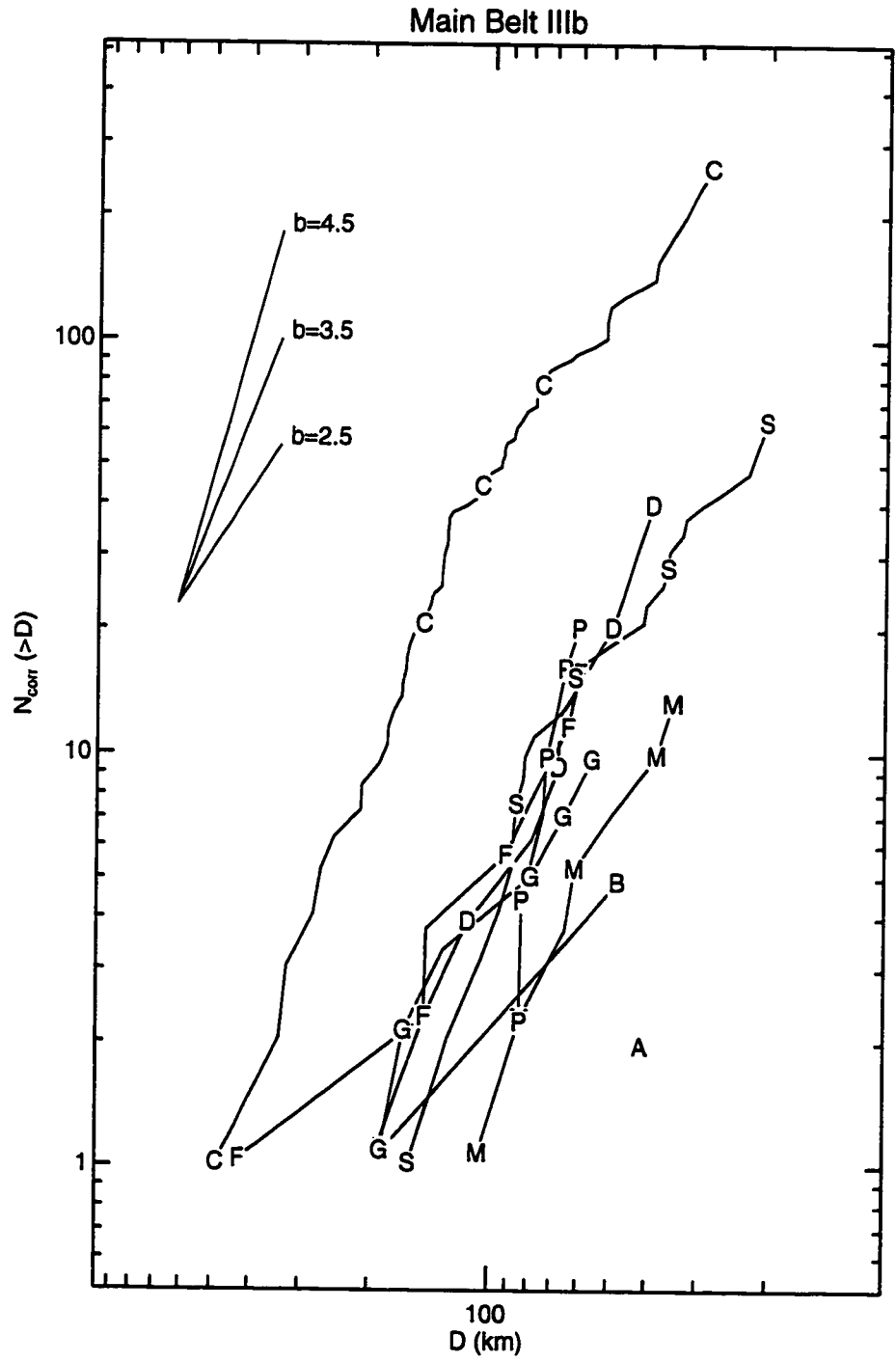


Figure 7.19: Cumulative Size-Frequency Diagram for Main Belt Zone IIIb.

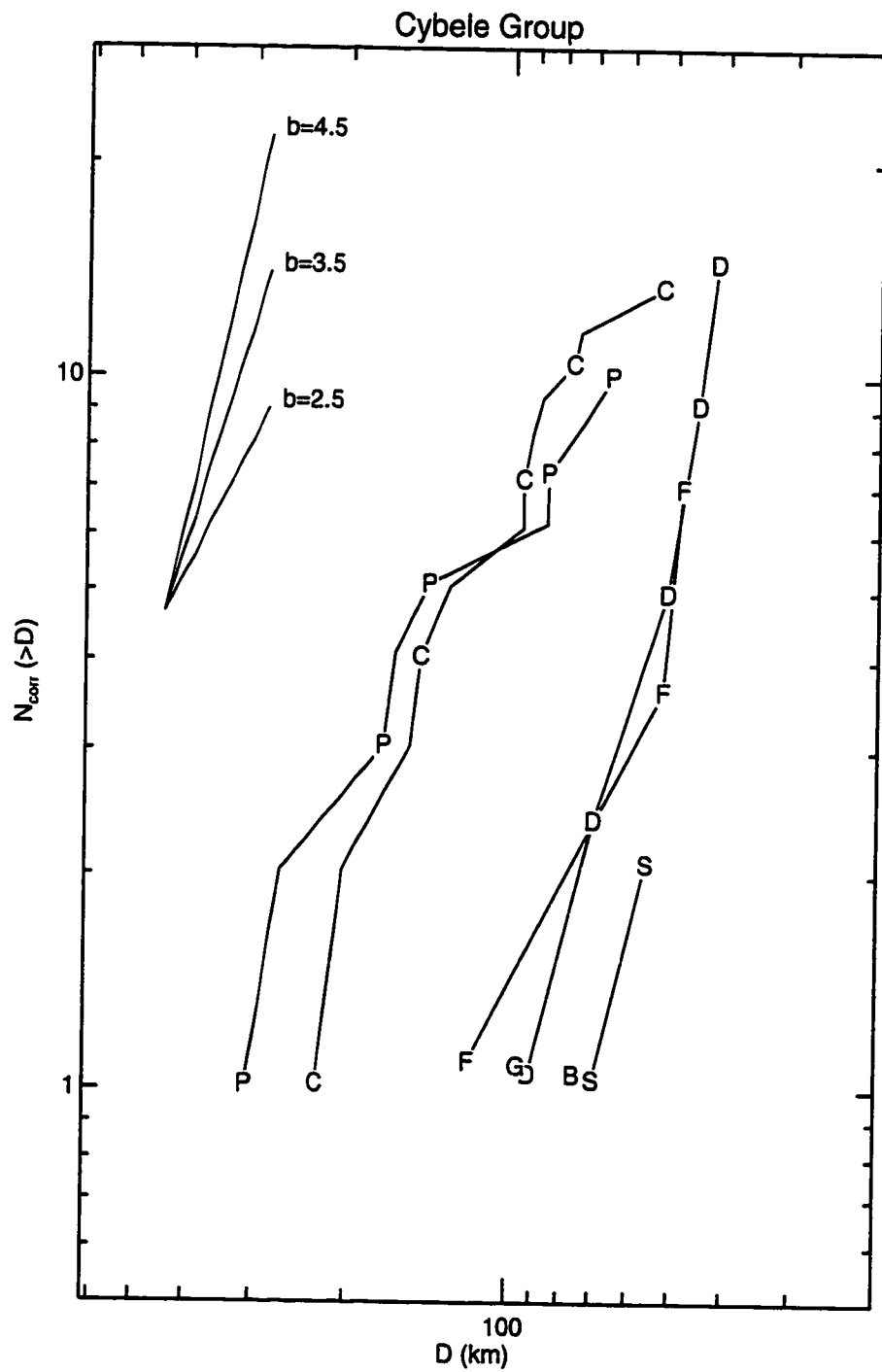


Figure 7.20: Cumulative Size-Frequency Diagram for the Cybele Group.

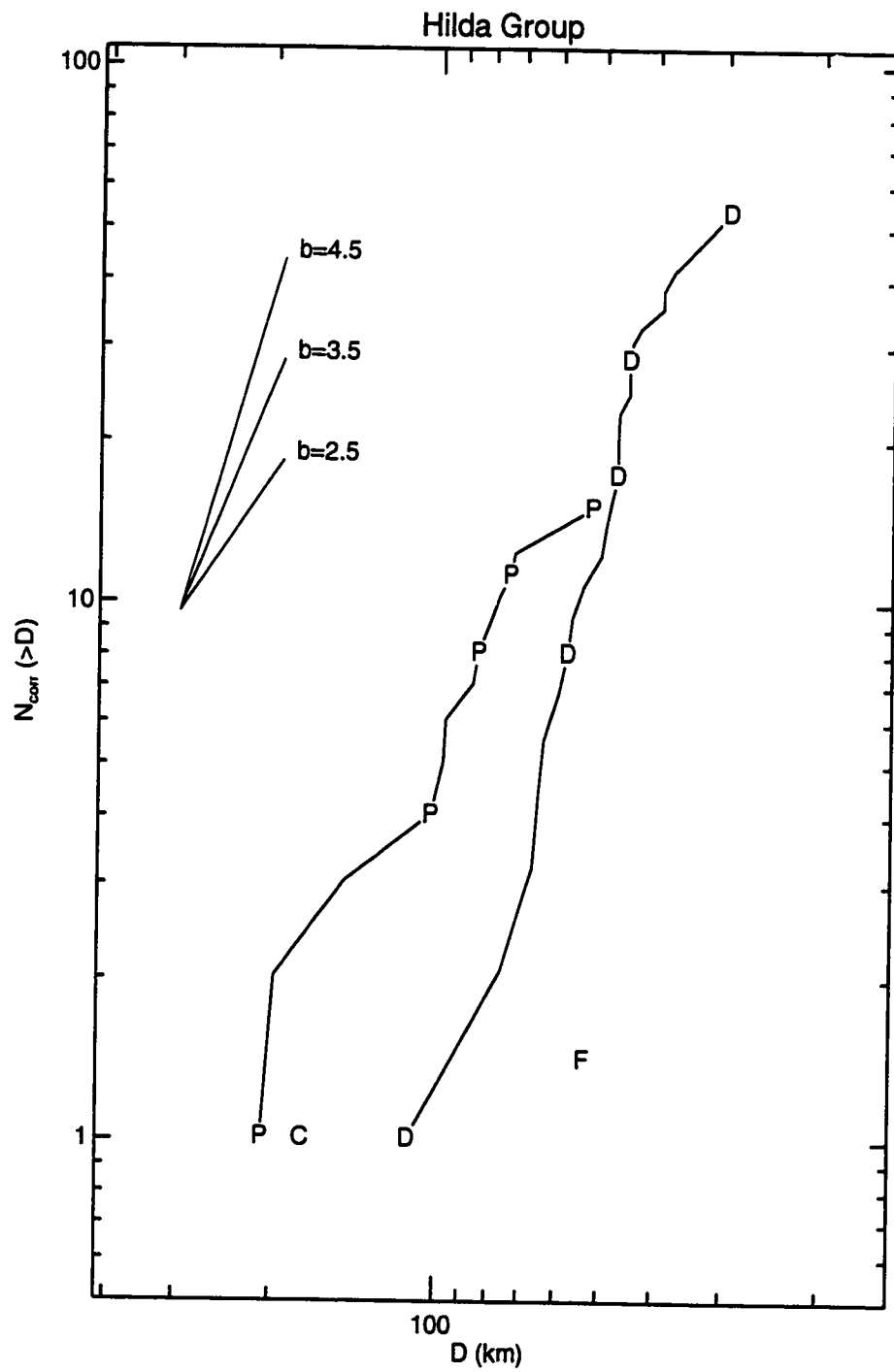


Figure 7.21: Cumulative Size-Frequency Diagram for the Hilda Group.

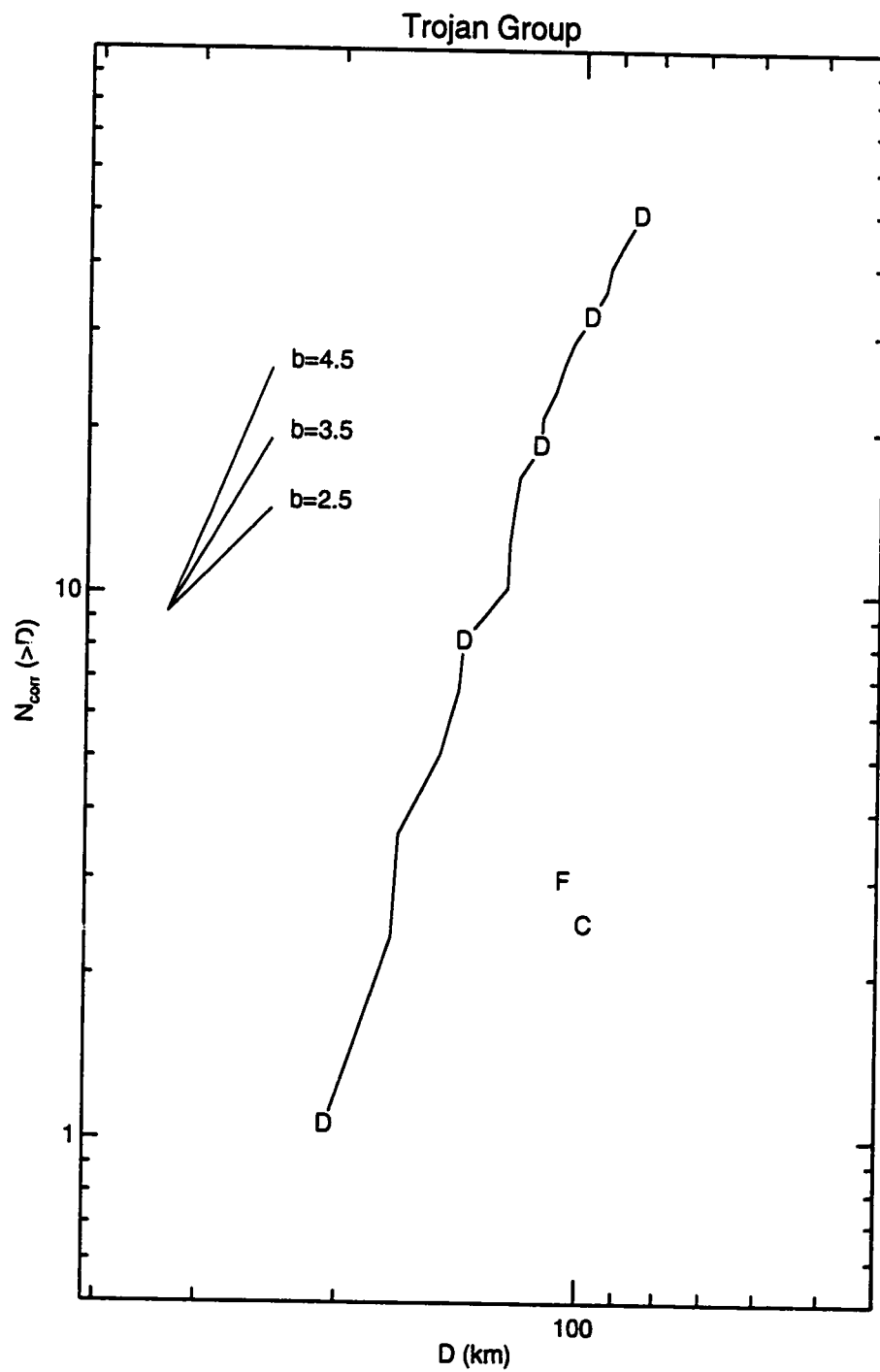


Figure 7.22: Cumulative Size-Frequency Diagram for the Trojan Group.

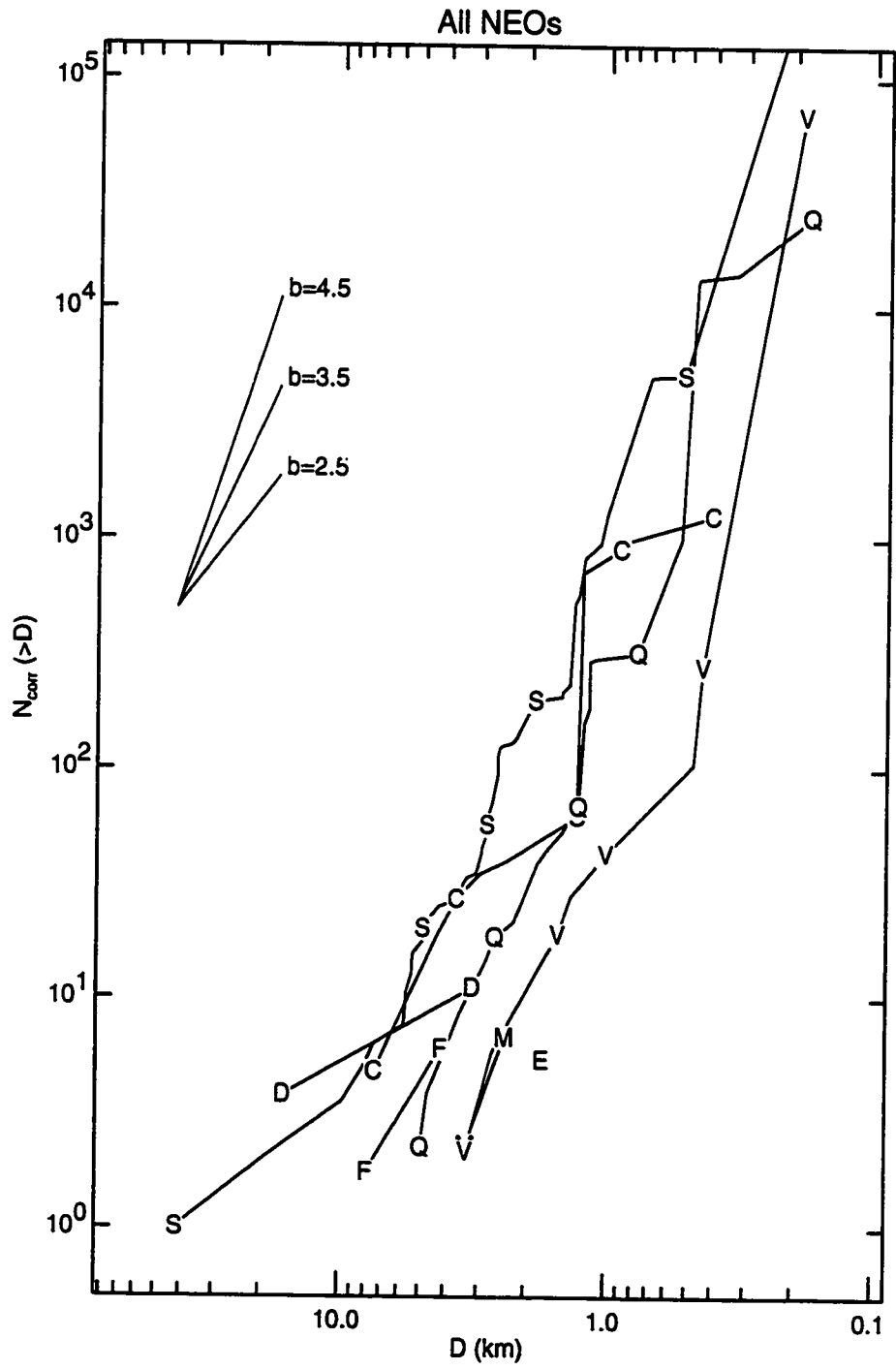


Figure 7.23: Cumulative Size-Frequency Diagram for the NEOs.

The overall slope of the size distribution in any given zone is sensitive to but not necessarily identical to the input model size distribution; caution must be exercised in drawing conclusions based on the overall slope. Changes in slope are less likely to derive from errors in the input model, and changes in relative numbers between different taxonomic classes still less so. For example, the sharp increase in the numbers of V-type objects in the Vesta Family is almost certainly real, and likewise the predominance of the F-types in the Nysa Family.

These diagrams point out the fact that no single ratio between taxonomic types can adequately describe the fraction of taxonomic types among either the asteroids or the NEOs. There are strong variations with size; this is perhaps most noticeable in the Vesta Family, where the V-types rise quickly in number at sizes smaller than 20 km.

Table 7.1 lists the taxonomic fractions in the 22 orbital element zones. These results are in good agreement with debiased distributions for main-belt asteroids reported by Luu & Jewitt (1990). Table 7.2 lists similar values, but for the combined NEO population. In this case, however, the new bias-corrected data showing an *excess* of S-types among the NEOs disagree with the results of Luu & Jewitt (1990), who found an S:C ratio of $0.2 \pm 0.1:1$. Their results rely on spectra of NEOs obtained over the limited wavelength range 4200 - 7200 Å, which end far blueward of the $1\mu\text{m}$ absorption feature which characterizes the S-type. Furthermore, their results hinge on the application of a strictly linear correction for phase reddening, for phase angles exceeding 60° . The taxonomic bias corrections of Luu & Jewitt (1989) can not be directly compared to the correction factors derived in this work, as their corrections do not take sample completeness into account, and so refer only to a bias against the discovery of new objects and not that in the existing, observed population.

These new results also indicate that the NEO population is even more rich in S-types than the 3:1 resonance main-belt asteroids. If the NEOs do derive in part from 3:1 resonance asteroids, then it may be necessary to include a secondary source which contains a higher fraction of S-type asteroids. The inner main belt may provide such a source, especially along the border of the ν_6 secular resonance. It is also worth noting that the S:C ratio among the NEOs is roughly comparable to that of the Mars Crossers (though the C-types among the Mars Crossers seem

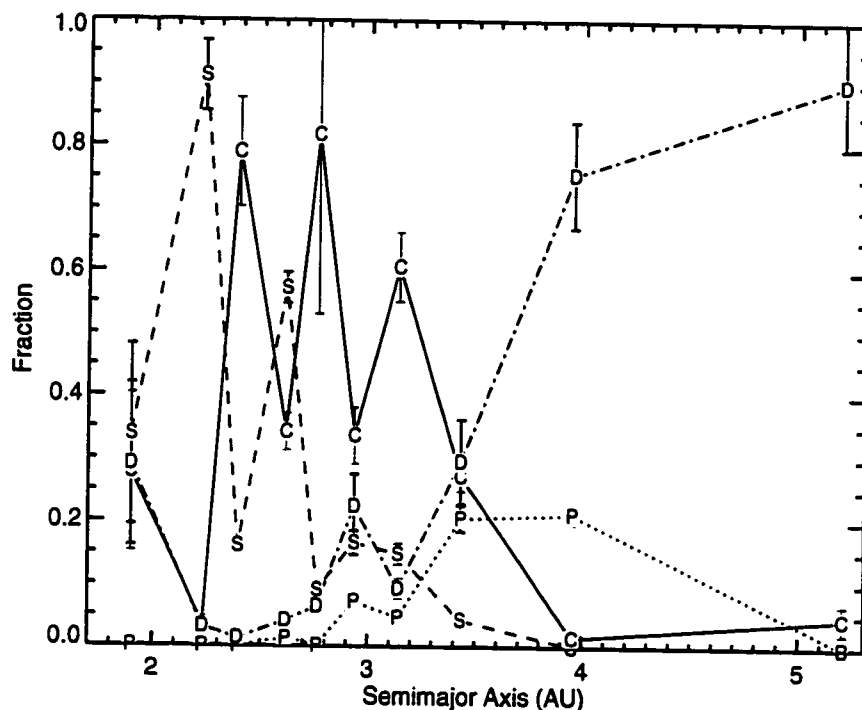


Figure 7.24: Taxonomic Gradient Across the Main Belt

to be of the B-subtype). These results hold true even if all the X-types among the NEOs are of the primitive P-type (Table 7.3).

Figure 7.23 presents the cumulative size-frequency diagram for the combined NEO population. It is immediately apparent that S-types dominate the numbers at nearly every magnitude. The anomalous D-type at a diameter of ~ 13 km is 3552 Don Quixote, an Amor object with a Jupiter-crossing orbit, and thus a very good candidate for an extinct comet. It is also clear that the fraction of C-type or other “primitive” types do *not* increase relative at smaller sizes; if anything, there is a deficit of C-types near diameters of ~ 2 km. This argues against there being a large population of extinct comets hidden among the ~ 1 km diameter NEOs.

The well-known heliocentric variation in taxonomic types (cf. Gradie et al. 1989) is displayed using this new data in Figure 7.24.

Table 7.1: Bias-corrected Taxonomic Fractions

| Atens | | | | |
|-------------|-----------------|-----------------|-----------------|-----------------|
| Diam. | S | Q | V | A |
| 1-10 km | 0.03 ± 0.01 | 0.30 ± 0.12 | 0.00 ± 0.00 | 0.00 ± 0.00 |
| 10-100 km | ... | ... | ... | ... |
| 100-1000 km | ... | ... | ... | ... |
| | | | | |
| Diam. | E | M | C | F |
| 1-10 km | 0.00 ± 0.00 | 0.09 ± 0.04 | 0.59 ± 0.19 | 0.00 ± 0.00 |
| 10-100 km | ... | ... | ... | ... |
| 100-1000 km | ... | ... | ... | ... |
| | | | | |
| Diam. | B | G | P | D |
| 1-10 km | 0.00 ± 0.00 | 0.00 ± 0.00 | 0.00 ± 0.00 | 0.00 ± 0.00 |
| 10-100 km | ... | ... | ... | ... |
| 100-1000 km | ... | ... | ... | ... |
| | | | | |
| Apollos | | | | |
| Diam. | S | Q | V | A |
| 1-10 km | 0.66 ± 0.12 | 0.31 ± 0.05 | 0.00 ± 0.00 | 0.00 ± 0.00 |
| 10-100 km | ... | ... | ... | ... |
| 100-1000 km | ... | ... | ... | ... |
| | | | | |
| Diam. | E | M | C | F |
| 1-10 km | 0.01 ± 0.00 | 0.00 ± 0.00 | 0.01 ± 0.00 | 0.01 ± 0.00 |
| 10-100 km | ... | ... | ... | ... |
| 100-1000 km | ... | ... | ... | ... |
| | | | | |
| Diam. | B | G | P | D |
| 1-10 km | 0.00 ± 0.00 | 0.00 ± 0.00 | 0.00 ± 0.00 | 0.00 ± 0.00 |
| 10-100 km | ... | ... | ... | ... |
| 100-1000 km | ... | ... | ... | ... |

Table 7.1 - *Continued*

| Amors | | | | |
|----------------|-----------------|-----------------|-----------------|-----------------|
| Diam. | S | Q | V | A |
| 1-10 km | 0.49 ± 0.15 | 0.00 ± 0.00 | 0.03 ± 0.01 | 0.00 ± 0.00 |
| 10-100 km | 0.35 ± 0.04 | 0.00 ± 0.00 | 0.00 ± 0.00 | 0.00 ± 0.00 |
| 100-1000 km | ... | ... | ... | ... |
| Diam. | E | M | C | F |
| 1-10 km | 0.00 ± 0.00 | 0.00 ± 0.00 | 0.48 ± 0.11 | 0.00 ± 0.00 |
| 10-100 km | 0.00 ± 0.00 | 0.00 ± 0.00 | 0.00 ± 0.00 | 0.00 ± 0.00 |
| 100-1000 km | ... | ... | ... | ... |
| Diam. | B | G | P | D |
| 1-10 km | 0.00 ± 0.00 | 0.00 ± 0.00 | 0.00 ± 0.00 | 0.01 ± 0.00 |
| 10-100 km | 0.00 ± 0.00 | 0.00 ± 0.00 | 0.00 ± 0.00 | 0.65 ± 0.30 |
| 100-1000 km | ... | ... | ... | ... |
| Hungaria Group | | | | |
| Diam. | S | Q | V | A |
| 1-10 km | 0.55 ± 0.06 | 0.00 ± 0.00 | 0.00 ± 0.00 | 0.00 ± 0.00 |
| 10-100 km | 0.34 ± 0.14 | 0.00 ± 0.00 | 0.00 ± 0.00 | 0.00 ± 0.00 |
| 100-1000 km | ... | ... | ... | ... |
| Diam. | E | M | C | F |
| 1-10 km | 0.45 ± 0.08 | 0.00 ± 0.00 | 0.00 ± 0.00 | 0.00 ± 0.00 |
| 10-100 km | 0.10 ± 0.04 | 0.00 ± 0.00 | 0.28 ± 0.13 | 0.00 ± 0.00 |
| 100-1000 km | ... | ... | ... | ... |
| Diam. | B | G | P | D |
| 1-10 km | 0.00 ± 0.00 | 0.00 ± 0.00 | 0.00 ± 0.00 | 0.00 ± 0.00 |
| 10-100 km | 0.00 ± 0.00 | 0.00 ± 0.00 | 0.00 ± 0.00 | 0.29 ± 0.13 |
| 100-1000 km | ... | ... | ... | ... |

Table 7.1 - *Continued*

| Mars Crossers | | | | |
|---------------|-----------------|-----------------|-----------------|-----------------|
| Diam. | S | Q | V | A |
| 1-10 km | 0.40 ± 0.11 | 0.00 ± 0.00 | 0.00 ± 0.00 | 0.00 ± 0.00 |
| 10-100 km | 0.52 ± 0.10 | 0.11 ± 0.05 | 0.00 ± 0.00 | 0.00 ± 0.00 |
| 100-1000 km | ... | ... | ... | ... |
| Diam. | E | M | C | F |
| 1-10 km | 0.00 ± 0.00 | 0.00 ± 0.00 | 0.00 ± 0.00 | 0.00 ± 0.00 |
| 10-100 km | 0.00 ± 0.00 | 0.03 ± 0.01 | 0.00 ± 0.00 | 0.20 ± 0.07 |
| 100-1000 km | ... | ... | ... | ... |
| Diam. | B | G | P | D |
| 1-10 km | 0.00 ± 0.00 | 0.00 ± 0.00 | 0.00 ± 0.00 | 0.60 ± 0.26 |
| 10-100 km | 0.14 ± 0.06 | 0.00 ± 0.00 | 0.00 ± 0.00 | 0.00 ± 0.00 |
| 100-1000 km | ... | ... | ... | ... |
| Flora Family | | | | |
| Diam. | S | Q | V | A |
| 1-10 km | 0.88 ± 0.06 | 0.00 ± 0.00 | 0.00 ± 0.00 | 0.00 ± 0.00 |
| 10-100 km | 0.91 ± 0.06 | 0.00 ± 0.00 | 0.00 ± 0.00 | 0.00 ± 0.00 |
| 100-1000 km | 1.00 ± 0.11 | 0.00 ± 0.00 | 0.00 ± 0.00 | 0.00 ± 0.00 |
| Diam. | E | M | C | F |
| 1-10 km | 0.00 ± 0.00 | 0.08 ± 0.01 | 0.04 ± 0.01 | 0.00 ± 0.00 |
| 10-100 km | 0.01 ± 0.00 | 0.02 ± 0.01 | 0.04 ± 0.01 | 0.00 ± 0.00 |
| 100-1000 km | 0.00 ± 0.00 | 0.00 ± 0.00 | 0.00 ± 0.00 | 0.00 ± 0.00 |
| Diam. | B | G | P | D |
| 1-10 km | 0.00 ± 0.00 | 0.00 ± 0.00 | 0.00 ± 0.00 | 0.00 ± 0.00 |
| 10-100 km | 0.00 ± 0.00 | 0.00 ± 0.00 | 0.00 ± 0.00 | 0.03 ± 0.01 |
| 100-1000 km | 0.00 ± 0.00 | 0.00 ± 0.00 | 0.00 ± 0.00 | 0.00 ± 0.00 |

Table 7.1 - *Continued*

| Phocaea Group | | | | |
|---------------|-------------------|-------------------|-------------------|-------------------|
| Diam. | S | Q | V | A |
| 1-10 km | (1.00 ± 0.12) | (0.00 ± 0.00) | (0.00 ± 0.00) | (0.00 ± 0.00) |
| 10-100 km | 0.78 ± 0.12 | 0.00 ± 0.00 | 0.00 ± 0.00 | 0.00 ± 0.00 |
| 100-1000 km | 0.00 ± 0.00 | 0.00 ± 0.00 | 0.00 ± 0.00 | 0.00 ± 0.00 |
| Diam. | E | M | C | F |
| 1-10 km | (0.00 ± 0.00) | (0.00 ± 0.00) | (0.00 ± 0.00) | (0.00 ± 0.00) |
| 10-100 km | 0.00 ± 0.00 | 0.00 ± 0.00 | 0.22 ± 0.07 | 0.00 ± 0.00 |
| 100-1000 km | 0.00 ± 0.00 | 0.00 ± 0.00 | 1.00 ± 0.22 | 0.00 ± 0.00 |
| Diam. | B | G | P | D |
| 1-10 km | (0.00 ± 0.00) | (0.00 ± 0.00) | (0.00 ± 0.00) | (0.00 ± 0.00) |
| 10-100 km | 0.00 ± 0.00 | 0.00 ± 0.00 | 0.00 ± 0.00 | 0.00 ± 0.00 |
| 100-1000 km | 0.00 ± 0.00 | 0.00 ± 0.00 | 0.00 ± 0.00 | 0.00 ± 0.00 |
| Nysa Family | | | | |
| Diam. | S | Q | V | A |
| 1-10 km | 0.79 ± 0.12 | 0.00 ± 0.00 | 0.00 ± 0.00 | 0.00 ± 0.00 |
| 10-100 km | 0.02 ± 0.00 | 0.00 ± 0.00 | 0.00 ± 0.00 | 0.01 ± 0.01 |
| 100-1000 km | 0.00 ± 0.00 | 0.00 ± 0.00 | 0.00 ± 0.00 | 0.00 ± 0.00 |
| Diam. | E | M | C | F |
| 1-10 km | 0.00 ± 0.00 | 0.00 ± 0.00 | 0.00 ± 0.00 | 0.00 ± 0.00 |
| 10-100 km | 0.01 ± 0.00 | 0.01 ± 0.00 | 0.32 ± 0.06 | 0.61 ± 0.08 |
| 100-1000 km | 0.00 ± 0.00 | 0.50 ± 0.08 | 0.00 ± 0.00 | 0.00 ± 0.00 |
| Diam. | B | G | P | D |
| 1-10 km | 0.21 ± 0.06 | 0.00 ± 0.00 | 0.00 ± 0.00 | 0.00 ± 0.00 |
| 10-100 km | 0.00 ± 0.00 | 0.00 ± 0.00 | 0.00 ± 0.00 | 0.02 ± 0.00 |
| 100-1000 km | 0.00 ± 0.00 | 0.50 ± 0.08 | 0.00 ± 0.00 | 0.00 ± 0.00 |

Table 7.1 - *Continued*

| Main Belt Zone I | | | | |
|------------------|-----------------|-----------------|-----------------|-----------------|
| Diam. | S | Q | V | A |
| 1-10 km | 0.90 ± 0.11 | 0.00 ± 0.00 | 0.10 ± 0.02 | 0.00 ± 0.00 |
| 10-100 km | 0.14 ± 0.01 | 0.00 ± 0.00 | 0.00 ± 0.00 | 0.00 ± 0.00 |
| 100-1000 km | 0.71 ± 0.04 | 0.00 ± 0.00 | 0.00 ± 0.00 | 0.00 ± 0.00 |
| Diam. | E | M | C | F |
| 1-10 km | 0.00 ± 0.00 | 0.00 ± 0.00 | 0.00 ± 0.00 | 0.00 ± 0.00 |
| 10-100 km | 0.00 ± 0.00 | 0.00 ± 0.00 | 0.81 ± 0.09 | 0.02 ± 0.01 |
| 100-1000 km | 0.00 ± 0.00 | 0.00 ± 0.00 | 0.14 ± 0.02 | 0.14 ± 0.02 |
| Diam. | B | G | P | D |
| 1-10 km | 0.00 ± 0.00 | 0.00 ± 0.00 | 0.00 ± 0.00 | 0.00 ± 0.00 |
| 10-100 km | 0.01 ± 0.00 | 0.01 ± 0.00 | 0.00 ± 0.00 | 0.01 ± 0.00 |
| 100-1000 km | 0.00 ± 0.00 | 0.00 ± 0.00 | 0.00 ± 0.00 | 0.00 ± 0.00 |
| Pallas Zone | | | | |
| Diam. | S | Q | V | A |
| 1-10 km | ... | ... | ... | ... |
| 10-100 km | 1.00 ± 0.51 | 0.00 ± 0.00 | 0.00 ± 0.00 | 0.00 ± 0.00 |
| 100-1000 km | 0.00 ± 0.00 | 0.00 ± 0.00 | 0.00 ± 0.00 | 0.00 ± 0.00 |
| Diam. | E | M | C | F |
| 1-10 km | ... | ... | ... | ... |
| 10-100 km | 0.00 ± 0.00 | 0.00 ± 0.00 | 0.00 ± 0.00 | 0.00 ± 0.00 |
| 100-1000 km | 0.00 ± 0.00 | 0.00 ± 0.00 | 0.00 ± 0.00 | 0.00 ± 0.00 |
| Diam. | B | G | P | D |
| 1-10 km | ... | ... | ... | ... |
| 10-100 km | 0.00 ± 0.00 | 0.00 ± 0.00 | 0.00 ± 0.00 | 0.00 ± 0.00 |
| 100-1000 km | 1.00 ± 0.42 | 0.00 ± 0.00 | 0.00 ± 0.00 | 0.00 ± 0.00 |

Table 7.1 - *Continued*

| Main Belt Zone IIa | | | | |
|--------------------|-------------------|-------------------|-------------------|-------------------|
| Diam. | S | Q | V | A |
| 1-10 km | (0.97 ± 0.12) | (0.03 ± 0.01) | (0.00 ± 0.00) | (0.00 ± 0.00) |
| 10-100 km | 0.59 ± 0.03 | 0.00 ± 0.00 | 0.00 ± 0.00 | 0.01 ± 0.00 |
| 100-1000 km | 0.22 ± 0.01 | 0.00 ± 0.00 | 0.00 ± 0.00 | 0.00 ± 0.00 |
| Diam. | E | M | C | F |
| 1-10 km | (0.00 ± 0.00) | (0.00 ± 0.00) | (0.00 ± 0.00) | (0.00 ± 0.00) |
| 10-100 km | 0.00 ± 0.00 | 0.01 ± 0.00 | 0.34 ± 0.03 | 0.00 ± 0.00 |
| 100-1000 km | 0.00 ± 0.00 | 0.02 ± 0.00 | 0.45 ± 0.03 | 0.07 ± 0.01 |
| Diam. | B | G | P | D |
| 1-10 km | (0.00 ± 0.00) | (0.00 ± 0.00) | (0.00 ± 0.00) | (0.00 ± 0.00) |
| 10-100 km | 0.00 ± 0.00 | 0.00 ± 0.00 | 0.01 ± 0.00 | 0.04 ± 0.01 |
| 100-1000 km | 0.00 ± 0.00 | 0.03 ± 0.01 | 0.10 ± 0.01 | 0.10 ± 0.01 |
| Main Belt Zone IIb | | | | |
| Diam. | S | Q | V | A |
| 1-10 km | ... | ... | ... | ... |
| 10-100 km | 0.09 ± 0.01 | 0.00 ± 0.00 | 0.00 ± 0.00 | 0.00 ± 0.00 |
| 100-1000 km | 0.19 ± 0.01 | 0.00 ± 0.00 | 0.00 ± 0.00 | 0.00 ± 0.00 |
| Diam. | E | M | C | F |
| 1-10 km | ... | ... | ... | ... |
| 10-100 km | 0.00 ± 0.00 | 0.01 ± 0.00 | 0.83 ± 0.30 | 0.01 ± 0.00 |
| 100-1000 km | 0.00 ± 0.00 | 0.02 ± 0.00 | 0.62 ± 0.03 | 0.07 ± 0.01 |
| Diam. | B | G | P | D |
| 1-10 km | ... | ... | ... | ... |
| 10-100 km | 0.00 ± 0.00 | 0.00 ± 0.00 | 0.00 ± 0.00 | 0.07 ± 0.01 |
| 100-1000 km | 0.00 ± 0.00 | 0.03 ± 0.01 | 0.02 ± 0.00 | 0.05 ± 0.01 |

Table 7.1 - *Continued*

| Koronis Zone | | | | |
|--------------|-----------------|-----------------|-----------------|-----------------|
| Diam. | S | Q | V | A |
| 1-10 km | ... | ... | ... | ... |
| 10-100 km | 1.00 ± 0.11 | 0.00 ± 0.00 | 0.00 ± 0.00 | 0.00 ± 0.00 |
| 100-1000 km | ... | ... | ... | ... |
| Diam. | E | M | C | F |
| 1-10 km | ... | ... | ... | ... |
| 10-100 km | 0.00 ± 0.00 | 0.00 ± 0.00 | 0.00 ± 0.00 | 0.00 ± 0.00 |
| 100-1000 km | ... | ... | ... | ... |
| Diam. | B | G | P | D |
| 1-10 km | ... | ... | ... | ... |
| 10-100 km | 0.00 ± 0.00 | 0.00 ± 0.00 | 0.00 ± 0.00 | 0.00 ± 0.00 |
| 100-1000 km | ... | ... | ... | ... |
| Eos Zone | | | | |
| Diam. | S | Q | V | A |
| 1-10 km | ... | ... | ... | ... |
| 10-100 km | 0.55 ± 0.06 | 0.00 ± 0.00 | 0.00 ± 0.00 | 0.00 ± 0.00 |
| 100-1000 km | ... | ... | ... | ... |
| Diam. | E | M | C | F |
| 1-10 km | ... | ... | ... | ... |
| 10-100 km | 0.00 ± 0.00 | 0.02 ± 0.01 | 0.06 ± 0.01 | 0.00 ± 0.00 |
| 100-1000 km | ... | ... | ... | .. |
| Diam. | B | G | P | D |
| 1-10 km | ... | ... | ... | ... |
| 10-100 km | 0.36 ± 0.12 | 0.00 ± 0.00 | 0.00 ± 0.00 | 0.00 ± 0.00 |
| 100-1000 km | ... | ... | ... | ... |

Table 7.1 - *Continued*

| Main Belt IIIa | | | | |
|----------------|-----------------|-----------------|-----------------|-----------------|
| Diam. | S | Q | V | A |
| 1-10 km | ... | ... | ... | ... |
| 10-100 km | 0.17 ± 0.02 | 0.00 ± 0.00 | 0.00 ± 0.00 | 0.01 ± 0.01 |
| 100-1000 km | 0.12 ± 0.01 | 0.04 ± 0.01 | 0.00 ± 0.00 | 0.00 ± 0.00 |
| Diam. | E | M | C | F |
| 1-10 km | ... | ... | ... | ... |
| 10-100 km | 0.00 ± 0.00 | 0.03 ± 0.01 | 0.32 ± 0.05 | 0.15 ± 0.04 |
| 100-1000 km | 0.00 ± 0.00 | 0.16 ± 0.01 | 0.44 ± 0.04 | 0.05 ± 0.01 |
| Diam. | B | G | P | D |
| 1-10 km | ... | ... | ... | ... |
| 10-100 km | 0.00 ± 0.00 | 0.00 ± 0.00 | 0.06 ± 0.02 | 0.25 ± 0.06 |
| 100-1000 km | 0.00 ± 0.00 | 0.00 ± 0.00 | 0.14 ± 0.02 | 0.05 ± 0.02 |
| Themis Zone | | | | |
| Diam. | S | Q | V | A |
| 1-10 km | ... | ... | ... | ... |
| 10-100 km | 0.00 ± 0.00 | 0.00 ± 0.00 | 0.00 ± 0.00 | 0.00 ± 0.00 |
| 100-1000 km | 0.00 ± 0.00 | 0.00 ± 0.00 | 0.00 ± 0.00 | 0.00 ± 0.00 |
| Diam. | E | M | C | F |
| 1-10 km | ... | ... | ... | ... |
| 10-100 km | 0.00 ± 0.00 | 0.00 ± 0.00 | 0.07 ± 0.01 | 0.85 ± 0.37 |
| 100-1000 km | 0.00 ± 0.00 | 0.00 ± 0.00 | 0.80 ± 0.05 | 0.20 ± 0.03 |
| Diam. | B | G | P | D |
| 1-10 km | ... | ... | ... | ... |
| 10-100 km | 0.07 ± 0.01 | 0.00 ± 0.00 | 0.00 ± 0.00 | 0.00 ± 0.00 |
| 100-1000 km | 0.00 ± 0.00 | 0.00 ± 0.00 | 0.00 ± 0.00 | 0.00 ± 0.00 |

Table 7.1 - *Continued*

| Griqua Group | | | | |
|----------------|-----------------|-----------------|-----------------|-----------------|
| Diam. | S | Q | V | A |
| 1-10 km | ... | ... | ... | ... |
| 10-100 km | 0.00 ± 0.00 | 0.00 ± 0.00 | 0.00 ± 0.00 | 0.00 ± 0.00 |
| 100-1000 km | ... | ... | ... | ... |
| Diam. | E | M | C | F |
| 1-10 km | ... | ... | ... | ... |
| 10-100 km | 0.00 ± 0.00 | 0.00 ± 0.00 | 1.00 ± 0.34 | 0.00 ± 0.00 |
| 100-1000 km | ... | ... | ... | ... |
| Diam. | B | G | P | D |
| 1-10 km | ... | ... | ... | ... |
| 10-100 km | 0.00 ± 0.00 | 0.00 ± 0.00 | 0.00 ± 0.00 | 0.00 ± 0.00 |
| 100-1000 km | ... | ... | ... | ... |
| Main Belt IIIb | | | | |
| Diam. | S | Q | V | A |
| 1-10 km | ... | ... | ... | ... |
| 10-100 km | 0.17 ± 0.02 | 0.00 ± 0.00 | 0.00 ± 0.00 | 0.01 ± 0.00 |
| 100-1000 km | 0.05 ± 0.01 | 0.00 ± 0.00 | 0.00 ± 0.00 | 0.00 ± 0.00 |
| Diam. | E | M | C | F |
| 1-10 km | ... | ... | ... | ... |
| 10-100 km | 0.00 ± 0.00 | 0.03 ± 0.01 | 0.58 ± 0.06 | 0.03 ± 0.01 |
| 100-1000 km | 0.00 ± 0.00 | 0.02 ± 0.00 | 0.75 ± 0.05 | 0.06 ± 0.01 |
| Diam. | B | G | P | D |
| 1-10 km | ... | ... | ... | ... |
| 10-100 km | 0.01 ± 0.00 | 0.02 ± 0.01 | 0.05 ± 0.01 | 0.10 ± 0.02 |
| 100-1000 km | 0.02 ± 0.00 | 0.05 ± 0.01 | 0.00 ± 0.00 | 0.06 ± 0.02 |

Table 7.1 - *Continued*

| Cybele Group | | | | |
|--------------|-----------------|-----------------|-----------------|-----------------|
| Diam. | S | Q | V | A |
| 1-10 km | ... | ... | ... | ... |
| 10-100 km | 0.05 ± 0.01 | 0.00 ± 0.00 | 0.00 ± 0.00 | 0.00 ± 0.00 |
| 100-1000 km | 0.00 ± 0.00 | 0.00 ± 0.00 | 0.00 ± 0.00 | 0.00 ± 0.00 |
| | | | | |
| Diam. | E | M | C | F |
| 1-10 km | ... | ... | ... | ... |
| 10-100 km | 0.00 ± 0.00 | 0.00 ± 0.00 | 0.22 ± 0.03 | 0.16 ± 0.05 |
| 100-1000 km | 0.00 ± 0.00 | 0.00 ± 0.00 | 0.45 ± 0.03 | 0.10 ± 0.03 |
| | | | | |
| Diam. | B | G | P | D |
| 1-10 km | ... | ... | ... | ... |
| 10-100 km | 0.03 ± 0.01 | 0.03 ± 0.01 | 0.13 ± 0.03 | 0.38 ± 0.09 |
| 100-1000 km | 0.00 ± 0.00 | 0.00 ± 0.00 | 0.45 ± 0.03 | 0.00 ± 0.00 |
| | | | | |
| Hilda Group | | | | |
| Diam. | S | Q | V | A |
| 1-10 km | ... | ... | ... | ... |
| 10-100 km | 0.00 ± 0.00 | 0.00 ± 0.00 | 0.00 ± 0.00 | 0.00 ± 0.00 |
| 100-1000 km | 0.00 ± 0.00 | 0.00 ± 0.00 | 0.00 ± 0.00 | 0.00 ± 0.00 |
| | | | | |
| Diam. | E | M | C | F |
| 1-10 km | ... | ... | ... | ... |
| 10-100 km | 0.00 ± 0.00 | 0.00 ± 0.00 | 0.00 ± 0.00 | 0.02 ± 0.01 |
| 100-1000 km | 0.00 ± 0.00 | 0.00 ± 0.00 | 0.17 ± 0.02 | 0.00 ± 0.00 |
| | | | | |
| Diam. | B | G | P | D |
| 1-10 km | ... | ... | ... | ... |
| 10-100 km | 0.00 ± 0.00 | 0.00 ± 0.00 | 0.17 ± 0.02 | 0.81 ± 0.09 |
| 100-1000 km | 0.00 ± 0.00 | 0.00 ± 0.00 | 0.67 ± 0.04 | 0.17 ± 0.02 |

Table 7.1 - *Continued*

| Trojan Group | | | | |
|--------------|-----------------|-----------------|-----------------|-----------------|
| Diam. | S | Q | V | A |
| 1-10 km | ... | ... | ... | ... |
| 10-100 km | 0.00 ± 0.00 | 0.00 ± 0.00 | 0.00 ± 0.00 | 0.00 ± 0.00 |
| 100-1000 km | 0.00 ± 0.00 | 0.00 ± 0.00 | 0.00 ± 0.00 | 0.00 ± 0.00 |
| Diam. | E | M | C | F |
| 1-10 km | ... | ... | ... | ... |
| 10-100 km | 0.00 ± 0.00 | 0.00 ± 0.00 | 0.11 ± 0.05 | 0.00 ± 0.00 |
| 100-1000 km | 0.00 ± 0.00 | 0.00 ± 0.00 | 0.00 ± 0.00 | 0.09 ± 0.05 |
| Diam. | B | G | P | D |
| 1-10 km | ... | ... | ... | ... |
| 10-100 km | 0.00 ± 0.00 | 0.00 ± 0.00 | 0.00 ± 0.00 | 0.89 ± 0.18 |
| 100-1000 km | 0.00 ± 0.00 | 0.00 ± 0.00 | 0.00 ± 0.00 | 0.91 ± 0.12 |
| Vesta Family | | | | |
| Diam. | S | Q | V | A |
| 1-10 km | 0.14 ± 0.03 | 0.00 ± 0.00 | 0.86 ± 0.07 | 0.00 ± 0.00 |
| 10-100 km | 0.23 ± 0.04 | 0.00 ± 0.00 | 0.15 ± 0.05 | 0.00 ± 0.00 |
| 100-1000 km | 0.50 ± 0.09 | 0.00 ± 0.00 | 0.50 ± 0.09 | 0.00 ± 0.00 |
| Diam. | E | M | C | F |
| 1-10 km | 0.00 ± 0.00 | 0.00 ± 0.00 | 0.00 ± 0.00 | 0.00 ± 0.00 |
| 10-100 km | 0.03 ± 0.01 | 0.00 ± 0.00 | 0.39 ± 0.08 | 0.00 ± 0.00 |
| 100-1000 km | 0.00 ± 0.00 | 0.00 ± 0.00 | 0.00 ± 0.00 | 0.00 ± 0.00 |
| Diam. | B | G | P | D |
| 1-10 km | 0.00 ± 0.00 | 0.00 ± 0.00 | 0.00 ± 0.00 | 0.00 ± 0.00 |
| 10-100 km | 0.00 ± 0.00 | 0.00 ± 0.00 | 0.00 ± 0.00 | 0.21 ± 0.06 |
| 100-1000 km | 0.00 ± 0.00 | 0.00 ± 0.00 | 0.00 ± 0.00 | 0.00 ± 0.00 |

Table 7.2: Bias-corrected Taxonomic Fractions for the NEOs (excluding X-types)

| Diam. | S | Q | V | A |
|-----------|-------------------|-------------------|-------------------|-------------------|
| 0.1–1 km | (0.04 ± 0.01) | (0.25 ± 0.06) | (0.70 ± 0.30) | (0.00 ± 0.00) |
| 1–10 km | 0.54 ± 0.13 | 0.13 ± 0.02 | 0.02 ± 0.00 | 0.00 ± 0.00 |
| 10–100 km | 0.35 ± 0.04 | 0.00 ± 0.00 | 0.00 ± 0.00 | 0.00 ± 0.00 |

| Diam. | E | M | C | F |
|-----------|-------------------|-------------------|-------------------|-------------------|
| 0.1–1 km | (0.00 ± 0.00) | (0.00 ± 0.00) | (0.01 ± 0.00) | (0.00 ± 0.00) |
| 1–10 km | 0.00 ± 0.00 | 0.00 ± 0.00 | 0.30 ± 0.07 | 0.00 ± 0.00 |
| 10–100 km | 0.00 ± 0.00 | 0.00 ± 0.00 | 0.00 ± 0.00 | 0.00 ± 0.00 |

| Diam. | B | G | P | D |
|-----------|-------------------|-------------------|-------------------|-------------------|
| 0.1–1 km | (0.00 ± 0.00) | (0.00 ± 0.00) | (0.00 ± 0.00) | (0.00 ± 0.00) |
| 1–10 km | 0.00 ± 0.00 | 0.00 ± 0.00 | 0.00 ± 0.00 | 0.00 ± 0.00 |
| 10–100 km | 0.00 ± 0.00 | 0.00 ± 0.00 | 0.00 ± 0.00 | 0.65 ± 0.30 |

The cumulative size-frequency distribution for S-type NEOs shows a wave-like oscillation in number. This is displayed in Figure 7.25, where a power-law distribution with an exponent of $b = 3.7$ has been divided out to better show the variation in numbers with size. The error bars in diameter are derived from the estimated 1σ uncertainties in magnitude for each object. The error bars in cumulative number are 1σ random errors in corrected number only. These waves are qualitatively similar to those predicted by Campo Bagatin et al. (1994) for collisional systems with a small-size cutoff. In this theory, the wave pattern occurs because particles just larger than the cutoff are not destroyed by impacts with smaller particles, and are created by the disruption of even larger bodies faster than they are depleted. This pattern extends upwards in size to diameters of tens of kilometers.

While there are qualitative similarities to the apparent oscillations seen in this work, the waves observed here have a much shorter wavelength than the ones

Table 7.3: Bias-corrected Taxonomic Fractions for the NEOs (if all X-types are P-type)

| Diam. | S | Q | V | A |
|-----------|-------------------|-------------------|-------------------|-------------------|
| 0.1-1 km | (0.03 ± 0.01) | (0.21 ± 0.05) | (0.58 ± 0.25) | (0.00 ± 0.00) |
| 1-10 km | 0.52 ± 0.13 | 0.12 ± 0.02 | 0.02 ± 0.00 | 0.00 ± 0.00 |
| 10-100 km | 0.35 ± 0.04 | 0.00 ± 0.00 | 0.00 ± 0.00 | 0.00 ± 0.00 |

| Diam. | E | M | C | F |
|-----------|-------------------|-------------------|-------------------|-------------------|
| 0.1-1 km | (0.00 ± 0.00) | (0.00 ± 0.00) | (0.00 ± 0.00) | (0.00 ± 0.00) |
| 1-10 km | 0.00 ± 0.00 | 0.00 ± 0.00 | 0.29 ± 0.07 | 0.00 ± 0.00 |
| 10-100 km | 0.00 ± 0.00 | 0.00 ± 0.00 | 0.00 ± 0.00 | 0.00 ± 0.00 |

| Diam. | B | G | P | D |
|-----------|-------------------|-------------------|-------------------|-------------------|
| 0.1-1 km | (0.00 ± 0.00) | (0.00 ± 0.00) | (0.17 ± 0.07) | (0.00 ± 0.00) |
| 1-10 km | 0.00 ± 0.00 | 0.00 ± 0.00 | 0.04 ± 0.01 | 0.00 ± 0.00 |
| 10-100 km | 0.00 ± 0.00 | 0.00 ± 0.00 | 0.00 ± 0.00 | 0.65 ± 0.30 |

in Campo Bagatin et al. (1994), where the peak-to-peak wavelength covers nearly two orders of magnitude in size (compared to a mere factor of ~ 2.5 seen in this work). If indeed the oscillations are real, then it is possible they are due to some other mechanism, such as an influx into the NEOs of fragments of a preferred size range ($D \sim 2.5$ km), perhaps due to stochastic cratering and fragmentation events in the main belt (Durda & Dermott 1997).

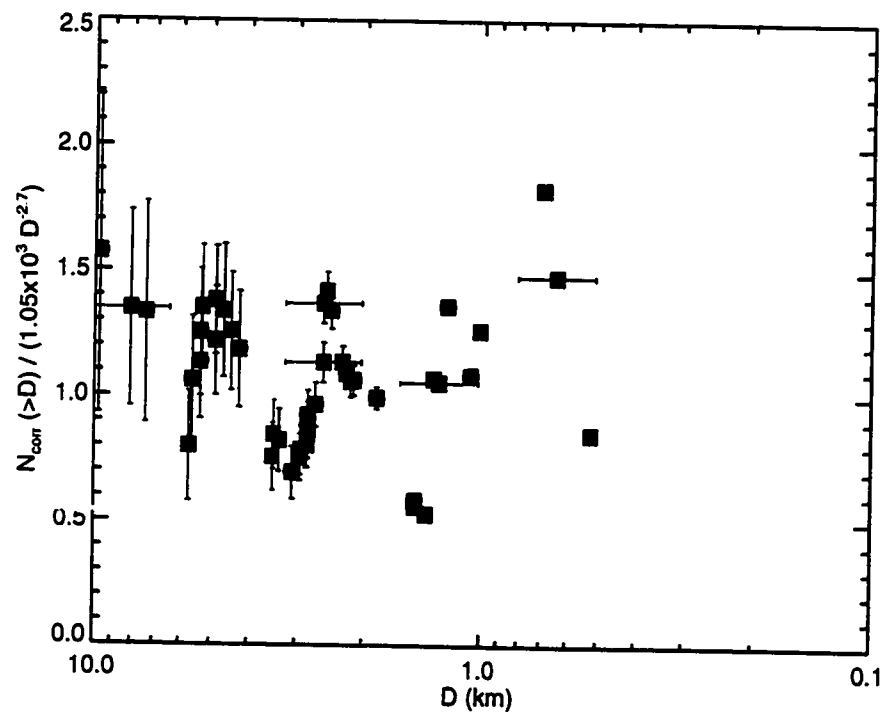


Figure 7.25: Wave-like Oscillation in the Size-Frequency Distribution of S-type NEOs.

Chapter 8

Conclusions

God keep me from ever completing anything. This whole book is but a draft - nay, but the draft of a draft. Oh Time, Strength, Cash, and Patience!

— Herman Melville

The observation and analysis of the reflectance spectra of a significant number of NEO and other objects, and their comparison with previously published NEO and main-belt asteroid spectra has allowed me to make several conclusions regarding individual objects and the general NEO population:

- The distribution of taxonomic types among the NEOs is similar to that of inner main-belt asteroids, and perhaps even richer in S-types than the 3:1 resonance asteroids. No evidence is found for any significant presence of extinct comets among the NEOs down to sizes of ~ 1 km.
- Several of the NEOs displaying $1\text{-}\mu\text{m}$ absorption bands have spectra similar if not identical to ordinary chondrite meteorites.
- Two of the traditionally strongest candidates for extinct comets (2201 Oljato and 2212 Hephaistos) are seen to have strong $1\text{-}\mu\text{m}$ absorption bands, consistent with the presence of mafic silicates on their surfaces, and inconsistent with current ideas of cometary surfaces.
- Four objects in cometary-type orbits (2906 Caltech, 2938 Hopi, 1994 EQ3, and 1996 PW) are seen to have relatively featureless red-sloped spectra consistent with observed comet nuclei.

- 3103 Eger, classed as an E-type object and suggested by Gaffey et al (1992) as the parent body of the enstatite achondrite meteorites, is seen to have an unusual spectrum with a very strong $1\text{-}\mu\text{m}$ absorption band, completely inconsistent with an enstatite composition.
- The trend of increasing $1\text{-}\mu\text{m}$ absorption band depth with decreasing size is confirmed in this study. The positive correlation of visual slope with increasing size is also confirmed by this study for objects larger than 10 km; however, the opposite effect is seen for smaller objects. This may help reconcile the differences between the S-type asteroids and the ordinary chondrite meteorites.

References

- Adams, J. B. 1975, in *Infrared and Raman spectroscopy of lunar and terrestrial minerals*, ed. C. Karr, Jr. (New York: Academic Press), 91
- Adams, J. B. 1974, *J. Geophys. Res.*, 79, 4829
- Adams, J. B. & Filice, A. L. 1967, *J. Geophys. Res.*, 72, 5705
- Barucci, M. A., Capria, M. T., Coradini, A., & Fulchignoni, M. 1987, *Icarus*, 72, 304
- Belton, M. J. S., Veverka, J., Thomas, P., Helfenstein, D., Simonelli, D., Chapman, C., Davies, M. E., Greeley, R., Greenberg, R., Head, J., Murchie, S., Klaasen, K., Johnson, T. V., McEwen, A., Morrison, D., Neukum, G., Fanale, F., Anger, C., Carr, M., & Pilcher, C. 1992, *Science*, 257, 1647
- Binzel, R. P., Bus, S. J., & Burbine, T. H. 1998, *Lunar and Planetary Science Conference*, 29, 1222
- Binzel, R. P. 1996, Private communication
- Binzel, R. P., Bus, S. J., Burbine, T. H., & Sunshine, J. M. 1996, *Science*, 273, 946
- Bowell, E. L. G. 1998, web page <ftp://ftp.lowell.edu/pub/elgb/astorb.html>
- Burns, R. G. 1993, *Mineralogical Applications of Crystal Field Theory* (New York: Cambridge Univ. Press)
- Campo Bagatin, A., Cellino, A., Davis, D. R., Farinella, P., & Paolicchi, P. 1994, *Planet. Space Sci.*, 42, 1079
- Charette, M. P., McCord, T. B., & Pieters, C. M. 1974, *J. Geophys. Res.*, 79, 11
- Chyba, C. F. 1990, *Nature*, 343, 129
- Davenport, S. A., Wdowiak, T. J., Jones, D. D., & Wdowiak, P. 1990, in *Global Catastrophes in Earth History: An Interdisciplinary Conference on Impacts, Volcanism, and Mass Mortality*, eds. V. L. Sharpton & P. D. Ward, Geological Soc. of America Special Paper 247 (Boulder: Geological Soc. of America)

- Dohnanyi, J. S. 1971, in *Physical Studies of Minor Planets*, ed. T. Gehrels (Washington, D. C.: N. A. S. A.), 263
- Durda, D. D. & Dermott, S. F. 1997, *Icarus*, 130, 140
- Farinella, P., Vokrouhlicky, D., & Hartmann, W. K. 1998, *Icarus*, 132, 378
- Fernández, Y. R., McFadden, L. A., Lisse, C. M., Helin, E. F., & Chamberlin, A. B. 1997, *Icarus*, 128, 114
- Filippenko, A. V. 1982, *PASP*, 94, 715
- Gaffey, M. J., Burbine, T. H., & Binzel, R. P. 1993, *Meteoritics*, 28, 161
- Gaffey, M. J., Reed, K. L., & Kelley, M. S. 1992, *Icarus*, 100, 95
- Gradie, J. C., Chapman, C. R., & Tedesco, E. F. 1989, in *Asteroids II*, eds. R. P. Binzel, T. Gehrels, M. S. Matthews. (Tucson: University of Arizona), 316
- Gradie, J. & Veverka, J. 1986, *Icarus*, 66, 455
- Greenberg, R., Head, J., Murchie, S., Klaasen, K., Johnson, T. V., McEwen, A., Morrison, D., Neukum, G., Fanale, F., Anger, C., Carr, M., & Pilcher, C. 1992, *Science*, 257, 1647
- Greenberg, R. & Nolan, M. C. 1989, in *Asteroids II*, eds. R. P. Binzel, T. Gehrels, M. S. Matthews (Tucson: University of Arizona), 778
- Grieve, R. A. F. & Shoemaker, E. M. 1994, in *Hazards Due to Comets and Asteroids*, ed. T. Gehrels (Tucson: University of Arizona), 417.
- Hardorp, J. 1978, *A&A*, 63, 383
- Hammergren, M. 1996, *AAS*, 187, 4203
- Helin, E. F. & Dunbar, R. S. 1990, *Vistas in Astronomy*, 33, 21
- Hicks, M. D., Fink, U., & Grundy, W. M. 1998, *Icarus*, 133, 69
- Hills, J. G. & Goda, M. P. 1993, *AJ*, 105, 1114
- Hörz, F. & Cintala, M. 1997, *Meteoritics and Planetary Science*, 32, 179
- Howell, E. S. 1994, Private communication.
- Howell, E. S., Merenyi, E., & Lebofsky, L. A. 1994, *J. Geophys. Res.*, 99, 110847

- Hunt, G. R. & Salisbury, J. W. 1970, *Modern Geology*, 1, 283
- Hunten, D. M. 1993, *Science*, 259, 915
- Jedicke, R. 1996, *AJ*, 111, 970
- Jedicke, R. & Heron, J. D. 1997, *Icarus*, 127, 494
- Jedicke, R. & Metcalfe, T. S. 1998, *Icarus*, 131, 245
- Kundic, T., Colley, W. N., Gott, J. R. III, Malhotra, S., Ue, Li-Pen, Rhoads, J. E., Stanek, K. Z., Turner, E. L, & Wambsganss, J. 1995, *ApJ*, 455, L5
- Lazzarin, M., Di Martino, M., Barucci, M. A., Doressoundiram, A., & Florczak, M. 1997, *A&A*, 327, 388
- Lipschutz, M. E., Gaffey, M. J., & Pellas, P. 1989, in *Asteroids II*, eds. R. P. Binzel, T. Gehrels, M. S. Matthews. (Tucson: University of Arizona), 740
- Love, S. G. & Ahrens, T. J. 1996, *Icarus*, 124, 141
- Luu, J. X. 1994, *PASP*, 106, 425
- Luu, J. X. 1993, *Icarus*, 104, 138
- Luu, J. X. & Jewitt, D. C. 1990, *AJ*, 100, 933
- Luu, J. X. & Jewitt, D. C. 1989, *AJ*, 98, 1985
- Marcus, J. N. & Olsen, M. A. 1991, in *Comets in the Post-Halley Era*, vol. 1, eds. R. L. Newburn, Jr., M. Neugebauer, & J. Rahe (Dordrecht: Kluwer)
- McCord, T. B., Adams, J. B., & Johnson, T. V. 1970, *Science*, 168, 3938
- McFadden, L. A., Cochran, A. L., Barker, E. S., Cruikshank, D. P., & Hartmann, W. K. 1993, *J. Geophys. Res.*, 98, 3031
- McFadden, L. A., Gaffey, M. J., & McCord, T. B. 1984, *Icarus*, 59, 25
- Melosh, H. J. 1980, *Annual Review of Earth and Planetary Sciences*, 8, 65
- Morrison, D. ed. 1992, *The Spaceguard Survey: Report of the NASA International Near-Earth Object Detection Workshop* (Pasadena: Jet Propulsion Laboratory)
- Muironen, K., Bowell, E., & Lumme, K. 1995, *A&A*, 293, 948
- Pieters, C. M. 1993, *J. Geophys. Res.*, 98, 20817

- Pieters, C. M. & McFadden, L. A. 1994, *Annual Review of Earth and Planetary Sciences*, 22, 457
- Rabinowitz, D. L. 1993, *ApJ*, 407, 412
- Rahe, J., Vanysek, V., & Weissman, P. R. 1994, in *Hazards Due to Comets and Asteroids*, ed. T. Gehrels (Tucson: University of Arizona), 597
- Ryan, E. V. & Melosh, H. J. 1998, *Icarus*, 133, 1
- Shoemaker, E., Canavan, G., Darrah, J., Harris, A., Morrison, D., Mumma, M., & Rabinowitz, D. 1995, *Report of Near-Earth Object Survey Working Group*
- Sunshine, J. M., Pieters, C. M., & Pratt, S. F. 1990, *J. Geophys. Res.*, 95, 6955
- Tedesco, E. F., Matson, D. L., & Veeder, G. J. 1989, in *Asteroids II*, eds. R. P. Binzel, T. Gehrels, M. S. Matthews (Tucson: University of Arizona), 290
- Tholen, D. J. & Barucci, M. A. 1989, in *Asteroids II*, eds. R. P. Binzel, T. Gehrels, M. S. Matthews (Tucson: University of Arizona), 298
- Tyson, J. A. 1989, in *CCDs in Astronomy*, ed. G. H. Jacoby, *ASP Conference Series*, 8, 1
- Veeder, G. J., Tedesco, E. F., & Matson, D. L. 1989, in *Asteroids II*, eds. R. P. Binzel, T. Gehrels, M. S. Matthews (Tucson: University of Arizona), 282
- Veverka, J., et al. 1996, *Icarus*, 120, 66
- Vokrouhlický, D. & Farinella, P. 1998, *A&A*, 335, 351
- Weissman, P. R., A'Hearn, M. F., McFadden, L. A., & Rickman, H. 1989, in *Asteroids II*, eds. R. P. Binzel, T. Gehrels, M. S. Matthews (Tucson: University of Arizona), 880
- Wetherill, G. W. 1974, *Annual Review of Earth and Planetary Sciences*, 2, 303
- Wisniewski, W. Z. 1987, *Icarus*, 70, 566
- Xu, S., Binzel, R. P., Burbine, T. H., & Bus, S. J. 1995, *Icarus*, 115, 1
- Zellner, B. 1979, in *Asteroids*, ed. T. Gehrels (Tucson: University of Arizona), 783
- Zellner, B., Tholen, D. J., & Tedesco, E. F. 1985, *Icarus*, 61, 355

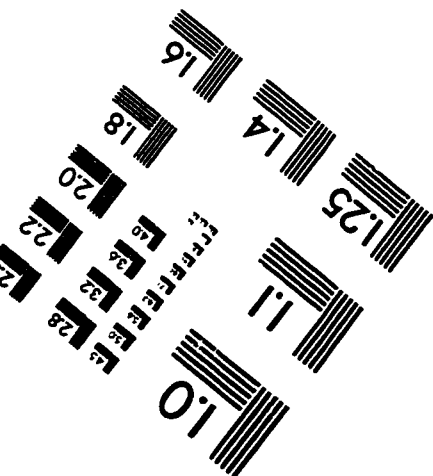
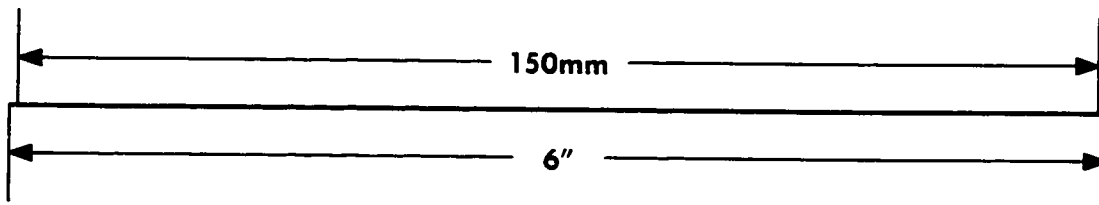
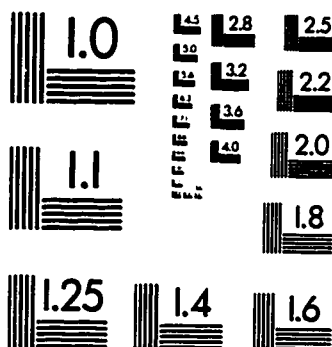
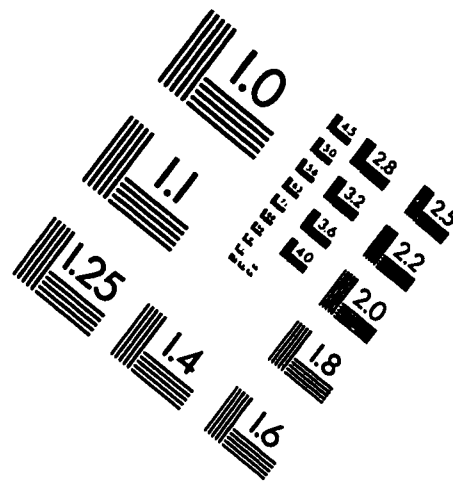
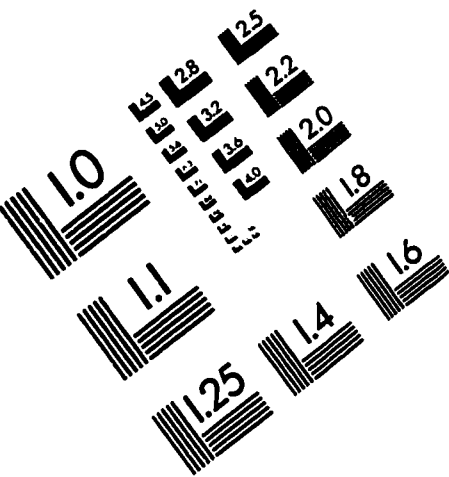
Curriculum Vitae

Mark Hammergren

Mark Hammergren was born in the gritty lakeside town of Waukegan, Illinois, on May 14, 1964. He attended the University of Illinois at Urbana-Champaign, and earned two BS degrees (Physics and Astronomy) in 1986. In 1991, he went to graduate school at the University of Washington Department of Astronomy. On the way to his PhD (to be awarded 1998), he picked up an MS in Astronomy in 1992.

In between, he usually found things to occupy his time, only some of which involved beer.

IMAGE EVALUATION TEST TARGET (QA-3)



APPLIED IMAGE, Inc
1653 East Main Street
Rochester, NY 14609 USA
Phone: 716/482-0300
Fax: 716/288-5989

© 1993, Applied Image, Inc., All Rights Reserved

